

https://dspace.org/

Predicting the effects of explosions placed on the earth's surface

Grobbelaar, Michelle Robyn Garvin

2020

https://hdl.handle.net/10539/30191

Grobbelaar, Michelle Robyn Garvin (2020) Predicting the effects of explosions placed on the earth's surface, University of the Witwatersrand, Johannesburg, <http://hdl.handle.net/10539/30191>

Downloaded from a DSpace repository. https://dspace.org/

PREDICTING THE EFFECTS OF EXPLOSIONS PLACED ON THE EARTH'S SURFACE

Michelle Robyn Garvin Grobbelaar
Student number: 0618727F

A dissertation submitted to the Faculty of Science, University of the Witwatersrand, in fulfilment of the requirements for the degree of Master of Science.

Johannesburg 2020

DECLARATION

I declare that this thesis is my own, unaided work. It is being submitted for the degree of Master of Science in the University of the Witwatersrand, Johannesburg. It has not been submitted before for any degree or examination in any other University.



_____

(Signature of candidate)

_____27_____ day of _____January_____ 2020

Acknowledgements

Special thanks to the Council for Geoscience for their support.

Contents

DECLARATION 1
Table of figures 4
List of tables 6
Glossary of terms 7
Acronyms, Abbreviations and Symbols 8
Abstract 9
1 Introduction 11
1.1 Background 11
1.2 Research objectives 11
2 Literature Review 12
2.1 Blast monitoring 12
2.2 Prediction equations for buried explosions 14
2.3 Prediction equations for explosions in the air or on the ground 19
3 Methodology 26
3.1 Monitoring of seismic signals 26
3.2 Monitoring of atmospheric signals 30
4 Results 35
4.1 Ground monitoring 35
4.1.1 PPV predictive equations 35
4.1.2 Peak displacement measurements 47
4.1.3 First arrival displacement 54
4.2 Atmospheric shock wave monitoring 61
4.2.1 Displacement of atmospheric shock wave 61
4.2.2 Secondary shock delay 68
5 Discussion 74
5.1 Ground monitoring 74
5.2 Surface/air monitoring 76
6 Conclusions 78
7 References 80
APPENDIX A 84
APPENDIX B 89
APPENDIX C 92
APPENDIX D 96
APPENDIX E 102

Table of figures

Figure 1. Graph of PPV limits modified from the United States Code of Federal Regulations (30 CFR part 816.67 of 1998)..... 13
Figure 2. Seismograms modified from Evers et al. (2007) indicating the P-wave arrival and air-coupled Rayleigh waves..... 20
Figure 3. Waveforms recorded by a 3-component accelerometer modified from Gitterman (2013)..... 23
Figure 4. Overpressure records modified from Gitterman (2013). 23
Figure 5. Seismograms of the vertical channel from stations at distances from 0.8 to 4.3 km modified from Bonner et al. (2013). 24
Figure 6. Seismograms of the vertical channel from stations at distances from 2 to 6 km modified from Bonner et al. (2013). 24
Figure 7. Comparison of ANFO and IMI explosives and the effect on the SS delay, modified from Gitterman (2013). 25
Figure 8. Typical installation of stations within the mobile network. 27
Figure 9. Indication of a typical station distribution in and around the demolition ranges at each site. 29
Figure 10. Example of the signal registered on all three components of a station 2.14km from the demolition range..... 32
Figure 11. An example of the signal registered on all three components at a station 4.89km from the demolition range 33
Figure 12. Example of the signal registered on all three components of stations 12.37km (left) and 3.6km (right) from the demolition range 34
Figure 13. The relation between PPV and SD for site 1. 36
Figure 14.The relation between PPV and SD for site 2. 37
Figure 15. The relation between PPV and SD for site 3. 38
Figure 16. The relation between PPV and SD for site 4. 39
Figure 17. The relation between PPV and SD for site 5. 40
Figure 18. The results of the USBM equation for all five sites. The coefficients calculated for each site are listed in Table 3..... 41
Figure 19. The results of the Ambraseys equation for all five sites. The coefficients calculated for each site are listed in Table 3. 41
Figure 20. The results of the Langefors equation for all five sites. The coefficients calculated for each site are listed in Table 3..... 42
Figure 21. The relation between PPV and SW for all 5 sites. 45
Figure 22. The results of the PPV vs SW equation for (a) all five sites and (b) only sites 1, 2, 4 and 5, excluding site 3 because it deviates significantly from the other sites..... 46
Figure 23. The relation between Peak displacement and SD for site 1. 48
Figure 24. The relation between Peak displacement and SD for site 2. 49
Figure 25. The relation between Peak displacement and SD for site 3. 50
Figure 26. The relation between Peak displacement and SD for site 4. 51
Figure 27. The relation between Peak displacement and SD for site 5. 52
Figure 28. The results for the USBM (peak displacement) equation for all five sites. The coefficients calculated for each site are listed in Table 3 53
Figure 29. The results for the Ambraseys (peak displacement) equation for all five sites. The coefficients calculated for each site are listed in Table 3 53
Figure 30. The results for the Langefors (peak displacement) equation for all five sites. The coefficients calculated for each site are listed in Table 3 53
Figure 31. The relation between the first arrival displacement and SD for site.1. 55

Figure 32. The relation between the first arrival displacement and SD for site 2. 56
Figure 33. The relation between the first arrival displacement and SD for site 3. 57
Figure 34. The relation between the first arrival displacement and SD for site 4. 58
Figure 35. The relation between the first arrival displacement and SD for site 5. 59
Figure 36. The results from the USBM (first arrival displacement) for all five sites. . The coefficients calculated for each site are listed in Table 3 60
Figure 37. The results from the Ambraseys (first arrival displacement) for all five sites. The coefficients calculated for each site are listed in Table 3 60
Figure 38. The results from the Langefors (first arrival displacement) for all five sites. The coefficients calculated for each site are listed in Table 3 60
Figure 39. The relation between the displacement caused by the atmospheric shock wave and SD for site 1..... 62
Figure 40. The relation between the displacement caused by the atmospheric shock wave and SD for site 2..... 63
Figure 41. The relation between the displacement caused by the atmospheric shock wave and SD for site 3..... 64
Figure 42. The relation between the displacement caused by the atmospheric shock wave and SD for site 4..... 65
Figure 43. The relation between the displacement caused by the atmospheric shock wave and SD for site 5..... 66
Figure 44. The results for the USBM (atmospheric shock displacement) relation for all five sites. The coefficients calculated for each site are listed in Table 5 67
Figure 45. The results for the Ambraseys (atmospheric shock displacement) relation for all five sites. The coefficients calculated for each site are listed in Table 5..... 67
Figure 46. The Langefors (atmospheric shock displacement) relation for all five sites. The coefficients calculated for each site are listed in Table 5 67
Figure 47. The relation between the scaled SS wave delay (Dt) and ln SD for all the sites. 70
Figure 48. The relation between scaled SS wave delay (Dt) and ln SD for all five sites. The coefficients calculated for each site are listed in Table 6 71
Figure 49. The relation between the log scaled SS wave delay (Dt) and log SD for all the sites..... 72
Figure 50. The relation between log scaled SS (Dt) and log SD for all five sites. . The coefficients calculated for each site are listed in Table 7. 73

List of tables

Table 1. PPV predictive equations used in the studies by Ozer (2008), Ozer et al. (2008), Puri and Prakash (1991). 16
Table 2. The geological description at each of the sites 30
Table 3. Empirical formulae for PPV, the Peak Displacement (Pk) and displacement of the first arrival (Fst) obtained from the five different sites. Table 1 displays the PPV equations and corresponding coefficients utilised. 43
Table 4. The resultant formulae obtained from the PPV vs SW calculations all five sites. 46
Table 5. Empirical formulae for the ground displacement caused by the atmospheric shock wave (Snd) obtained from the five different sites. 68
Table 6. Empirical formulae for the scaled SS wave delay (Dt) obtained from the five different sites. 69
Table 7. Empirical formulae for the relationship between the scaled secondary shock (SS) wave delay (Dt) and scaled distance obtained from the five sites. ... 71
Table 8. Summary of the suitability of each of the equations examined in achieving the objectives of the study. 79
Table 9. Measurements from site 1. A comma separates each measurement listed. 84
Table 10. Measurements from site 2. A comma separates each measurement listed 89
Table 11. Measurements from site 3. A comma separates each measurement listed 92
Table 12. Measurements from site 4. A comma separates each measurement listed 96
Table 13. Measurements from site 5. A comma separates each measurement listed 102

Glossary of terms

(Air) Blast wave	The increase in pressure created by a detonation in the atmosphere which then moves away from the centre of the blast in a spherical wave front.
Displacement of atmospheric shock wave (Snd)	The measured displacement caused by the atmospheric shock wave (nm).
Elastic waves	The waves within a medium where the particles are restored to their original position after being disturbed.
First arrival displacement (Fst)	The peak displacement of the first seismic arrival of the movement of particles at the surface of the Earth (nm).
Infrasound	The sound that has a lower frequency than 20 Hz, i.e. lower than the limit of human hearing.
Overpressure (blast overpressure)	The pressure caused by a shock wave which exceeds the normal atmospheric pressure.
Peak displacement (Pk)	The peak displacemnt of the movement of particles at the surface of the Earth (nm).
Peak particle velocity (PPV)	The peak velocity of the movement of particles at the surface of the Earth (nm/s).
Shock wave	The wave that moves faster than the ambient speed of sound within a medium. It is distinguished by a sudden, almost disjointed, transformation in pressure, density and temperature of the medium through which it is travelling.
Secondary shock wave delay (Dt)	The delay between the main and secondary shock wave. These secondary, and sometimes tertiary, shock waves occur when the air blast wave for an explosion source displays a number of recurrent shocks of smaller magnitudes and at different times, caused by successive implosion of rarefaction waves (the area of low relative pressure following a shock wave) (sec).
Velocity of detonation (VOD)	The velocity at which the shock wave front travels through a detonated explosive.

Acronyms, Abbreviations and Symbols

β	Specific geological constant
Dt	Secondary shock wave delay (sec)
Fst	First arrival displacement (nm)
K	Ground transmission coefficient
MS	Main shock of the atmospheric shock wave
Pk	Peak displacement (nm)
PPV	Peak particle velocity (nm/s)
R	Distance from the explosion to the station (m)
SD	Scaled distance (m)
Snd	Displacement of atmospheric shock wave (nm)
SS	Secondary shock of the atmospheric shock wave
SW	Scaled weight (kg/m)
VOD	Velocity of detonation (m/s)
W_d	Maximum charge per explosion (kg)

Abstract

Many predictive equations within literature are focused on explosions within the ground such as mining blasts and tunnelling. According to the United States Code of Federal Regulations (30 CFR part 816.67 of 1998), the recommended equipment to monitor buried explosions, are geophones. Other equations which examine surface explosions utilise a number of specialised equipment in addition to the seismograph equipment used for monitoring buried explosions, such as microphones and pressure gauges. The aim of this study is to determine whether or not one could use predictive equations for buried explosions to predict the effects from surface explosions by merely using data obtained from a small network of surface installed seismograph stations.

Military demolition sites are areas where old and potentially unstable explosives and obsolete equipment are destroyed and the ordnance is placed on the surface of the ground and detonated. The ordnance is seldom buried and thus modelling and predicting the ground vibrations and shock waves should consider predictive equations for both ground waves and atmospheric shock waves. The modelling can assist in preventing damages to surrounding infrastructure and injury to people in the vicinity. These equations could similarly be utilised for assisting in forensic seismology to determine the details of unexpected explosions, such as gas pipelines, silo explosions and vehicle bombs.

By combining the various equations available, this study has identified a number of predictive equations which have produced acceptable results when examining data obtained from military ordnance demolitions on the surface.

In general, the values for atmospheric shock waves are easier to determine than those from the ground motion because the atmospheric shock waves are more prominent on the seismograms than those of the ground motion, due to the fact that very little of the energy is transmitted into the ground. Therefore, utilising atmospheric shock wave measurements may be more useful because the ground motion waves are not clearly recorded.

The study has shown that the USBM peak particle velocity (PPV) predictive

equation was identified as the most reliable equation out of the three predictive equations developed for buried explosions that were examined. In addition, the study has shown that a less cumbersome yet equally effective relation between PPV and scaled weight (SW) may be more favourable to utilise. However, the predictive equation using the secondary atmospheric shock wave phenomenon produced better results and were easier to measure.

The usefulness of the suggested prediction equations would depend on what requires predicting. For modelling the effects of explosions from a military demolition range on the surrounding infrastructure, one would require PPV prediction and thus the USBM and PPV vs SW relations will provide better solutions. On the other hand, for assisting in forensic seismology to determine the details of an unexpected explosion, the secondary atmospheric shock wave and atmospheric shock wave displacement could be utilised, especially if the ground motion waves are not well recorded.

1 Introduction

1.1 Background

Military demolition sites are areas where old and potentially unstable explosives and obsolete equipment are destroyed. Typically, the ordnance is placed on the surface of the ground and detonated. Ideally the area is located far from any human activity or dwellings, and is cleared prior to use. However, some demolition sites have experienced the encroachment of human settlements. Consequently, modelling and monitoring of the ground vibrations and air blasts have become a priority to ensure that the blasts do not cause irritating disturbances to the local inhabitants or damage to structures that may result in protests and legal challenges. Prediction Equations that could be utilised to predict the effects of the demolition ranges on the surrounding population and structures would be useful in mitigating these risks.

Such prediction equations would not only assist with determining the effects of explosions from a military demolition range on the surrounding infrastructure, but it can also assist with forensic seismology when determining the details of an unexpected explosion, such as gas pipelines, silo explosions and vehicle bombs. However, there appears to be very little literature available that provides suitable prediction equations for on-surface/air explosions. The predictive equations which are readily available have been developed for buried explosions.

1.2 Research objectives

The objectives of this study are:

1) To determine whether it is possible to utilise equations developed for predicting the ground motion produced by buried explosions to predict the effects of explosions on the Earth's surface.
2) To determine whether other predictive equations are available that are more suitable for explosions on the Earth's surface.

2 Literature Review

2.1 Blast monitoring

Blasts or explosions on the Earth's surface, such as at demolition ranges, create seismic waves that travel through the ground and overpressure (air pressure waves) through the atmosphere, which can both shake buildings and disturb people. Together, these phenomena are referred to as seismoacoustics (Ford *et al.*, 2014).

Typically a blast can be characterized by the nature of explosive material utilised, whether there was any reflection (due to geology, topography, atmosphere, etc.) and the extent to which the blast was contained. Overpressure generally occurs when the explosions are on or above the surface of the ground (Williams and Newell, 1991) and in some cases, the overpressure can be recorded up to 2 seconds after the seismic waves when the explosion is approximately 1km from the sensors. The perception of both the ground vibrations and the overpressure is stronger inside buildings than outside. In fact, overpressure may be the cause of complaints which have been erroneously attributed to ground vibration.

The recorded ground motion from blasts is not simple to characterize due to the radiation pattern from the site of the explosion, which is affected by geological factors such as: (1) geometrical spreading, (2) separation of compressional shear and surface waves, (3) reflection, refraction, diffraction and scattering and mode conversion, and (4) frequency-dependent attenuation (New, 1991). In addition, it is influenced by aspects such as the size of the explosion and the distance from the explosion (Puri and Prakash, 1991). It has been noted that geological disparities within the near-surface layer can cause amplification or attenuation of ground motion by as much as four-fold, in comparison to a site established on bedrock (Redmayne and Turbitt, 1991). Similarly, different types of detonations and the prevailing weather conditions, such as temperature gradients, wind direction and cloud cover, can affect the overpressure. These phenomena, along with the features of the structure (such as the foundation, etc.) make accurate predictions of nuisance or damage difficult.

Puri and Prakash (1991) stated that peak particle velocity (PPV) provides an

excellent criterion for assessing the damage due to blast effects, which can sometimes be seen several kilometres away from the blast site and it is therefore widely used for monitoring. They used empirical relations to examine ground motion caused by field blast tests for a proposed limestone quarry and noted that structural damage and PPV show a good correlation over a wide range of frequencies with damage likely to occur when the PPV > 125 mm/s. This PPV corresponds to an earthquake of intensity between VII and VIII on the modified Mercalli intensity scale (MMI), and thus PPV is still the most common single ground motion descriptor for regulating blast designs. The United States Code of Federal Regulations (30 CFR part 816.67 of 1998) sets a limit of 5.08 mm/s at 1 Hz, 19.1 mm/s for frequencies between 4 and 12 Hz, and 50.8 mm/s for frequencies above 30 Hz (Figure 1). Overpressure, on the other hand, may cause buildings to vibrate but structural damage is rare and is usually in the form of broken windows.

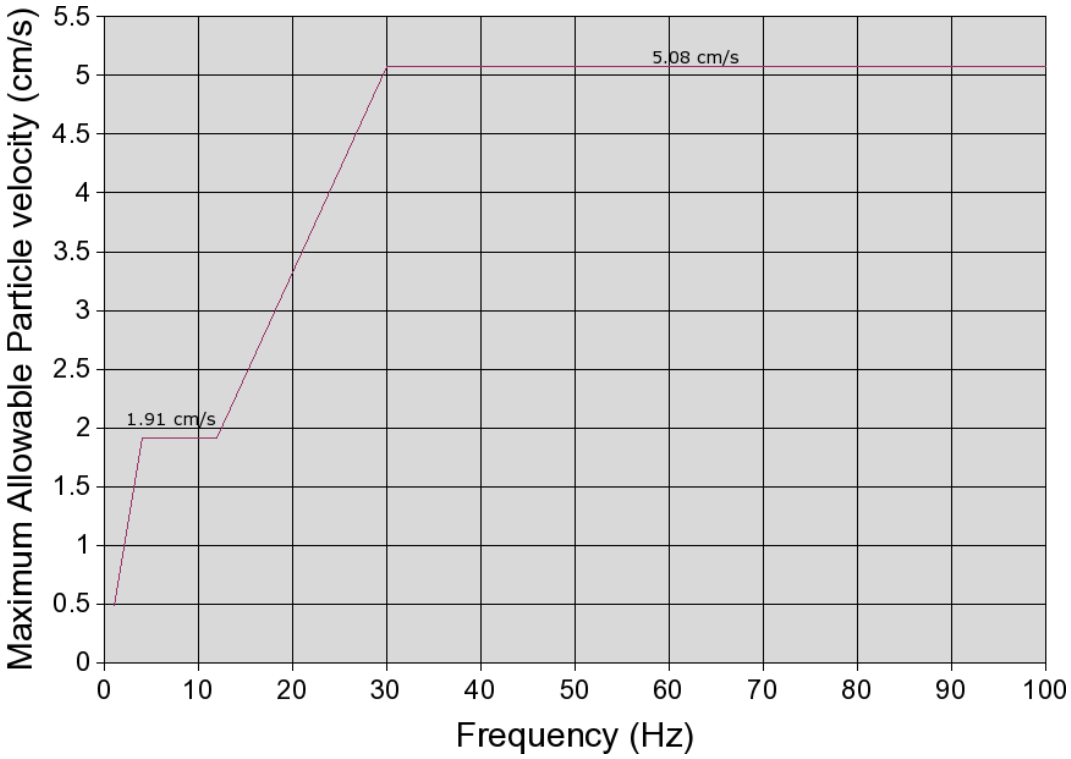


Figure 1. Graph of PPV limits modified from the United States Code of Federal Regulations (30 CFR part 816.67 of 1998).

In order to encompass the complexity of the blasts, charge weight and distance are combined to produce a quality called scaled distance, which generally uses the square root of the maximum weight of the charge for ground vibration and the cube

root for overpressure. Thus, the scaled distance is a combination of the maximum weight of explosive used in generating the vibrations through the ground and air with distance. The 'cube root scaled' distance is the distance from the blast to a defined position divided by the cube root of the maximum weight of explosives. Scaled distance is similarly calculated, however the distance is divided by the square root of the maximum weight of explosives. This weight is determined by the maximum weight in any 8-milisecond period (Joint Committee on Administrative Rules, 1998).

Ford *et al.* (2014) emphasized the importance of quantitative models of signal intensity for predicting explosion effects when the yield and emplacements (height above ground or depth of burial) are known, and inversely when inferring the yield and emplacement based on observed intensities. Kahriman (2002) and Ozer *et al.* (2008) examined a number of predictor equations proposed in the literature, and concluded that due to the large number of complications related to surface blasting, a suitable generic formula has not yet been determined. In addition, Ford *et al.* (2014) found that the literature on seismic motions from surface explosions is smaller than those from buried explosions.

2.2 Prediction equations for buried explosions

Ozer *et al.* (2008) examined ground vibrations caused by bench blasting at a quarry and stated that vibrations caused by blasting are one of the main problems in mining and quarrying, and thus the effects of ground motions caused by blasting on infrastructure and the community should be determined and monitored. Such monitoring involves setting a cautious limit, commonly an established and accepted standard such as the United States Code of Federal Regulations (30 CFR part 816.67 of 1998) which sets a PPV limit of 19.1 mm/s for frequencies below 12 Hz and 50.8 mm/s for frequencies above 30 Hz (Figure 1). In addition, it usually involves instrumental monitoring, such as seismographs, or utilisation of predictive equations involving the scaled distance term.

There is extensive literature describing prediction equations for the vibrations induced by blasting in open pit mines and during tunnelling, for example, Aloui *et al.* (2016) provided a case study from Tunisia; Bongiovanni *et al.* (1991) a case

study from Italy; Khandelwal and Singh (2007) provided a case study from a magnesite mine in India; Kahriman (2002), Ozer (2008) and Ozer *et al.* (2008) examined case studies from Turkey; Milev *et al* (2016) examined cases within South Africa; and Puri and Prakash (1991) examined field blast tests for a proposed limestone quarry. Kumar *et al.* (2016) succinctly summarised the vast number of prediction equations developed since 1959, when they examined methods of creating a model which can address the rock properties of the sites using predictive relations. They cautioned, however, that the equations are site-specific to the study and should not be generalised for other sites. They concluded that PPV is not as sensitive to changes in geological conditions as acceleration and displacement.

The most common approach to take when determining a prediction equation is to plot the variation of PPV with scaled distance (New (1991); Puri and Prakash (1991); Bongiovanni *et al.* (1991); Kahriman (2002); Blair (2004); Khandelwal and Singh (2007); Ozer (2008); Ozer *et al*. (2008)). The variation of PPV is clear, but the relationship of PPV with explosive weight is not as well defined. The relationship of PPV with scaled distance combines distance and explosive weight. Blair (2004) recommends the use of a weighted scaled distance as it is more consistent with the notion of waveform superposition.

Ozer *et al.* (2008), Ozer (2008), Khandelwal and Singh (2007) and Bongiovanni *et al*. (1991) used three PPV-based predictor equations chosen from a number of equations proposed in literature: (a) the United States Bureau of Mines (USBM) equation, (b) the Ambraseys-Hendron equation (Ambraseys and Hendron, 1968) and (c) the Langefors-Kihlstrom equation (Langefors and Kihlstrom, 1963), to establish a relationship between PPV and scaled distance (SD) (Table 1). Khandelwal and Singh (2007) introduced a fourth equation, which is the Indian standard, but it is not commonly utilised elsewhere. The USBM equation uses the square root scaled distance, Ambraseys-Hendron the cube root scaled distance and the Langefors-Kihlstrom uses a different formula for scaled distance. Thus, the three equations represent a good sample of the typical predictive equations available. Aloui *et al.* (2016) stated that even with the large number of prediction equations available within the international literature, the USBM equation is the most widely used one because it provides the better results.

Ozer *et al.* (2008) examined all three equations and compared the results with the ground vibrations recorded during the monitoring of production-related blasting at the Akyol quarry in Turkey. They used the relation with the best results to determine practical blasting charts for the quarry. Bongiovanni *et al.* (1991) observed that the equations used on test blasts monitored during the tunnel construction in Valle d'Áosta, Italy, appear to be a poor fit for the data near the source (<50m). They suggested that a source term accounting for the source geometry should be added because results from a frequency analysis show a large spread in the energy distribution, implying that the physical and geometrical effects tend to be dominant in the propagation of the waves originating from the blastings. They examined the reliability of the Langefors relationship (Table 1) and the constant (K) for the physical effect of soil. However, all their data showed a poor correlation for the Langefors equation and thus they concluded that it was not reliable to predict ground motion produced by blasts for sites with similar soil characteristics to the sites which they examined.

Table 1. PPV predictive equations used in the studies by Ozer (2008), Ozer et al. (2008), Puri and Prakash (1991).

	USBM	**Ambraseys-Hendron**	**Langefors-Kihlstrom**
PPV prediction equation	$PPV\ (mm/s) = K(SD)^{-\beta}$ ($logPPV=-\beta logSD+logK$)	$PPV(mm/s)=K(SD_A)^{-\beta}$ ($logPPV=-\beta logSD_A+logK$)	$PPV(mm/s)=K(SD_L)^{\beta}$ ($logPPV=\beta logSD_L+logK$)
SD equation	$SD = R/(W_d)^{0.5}$	$SD_A = R/(W_d)^{0.3}$	$SD_L=(W_d/(R)^{0.6})^{0.5}$

Where:

PPV = peak particle velocity

SD = scaled distance

K = the ground transmission coefficient

β = the specific geological constant

R = distance from explosion to station (m)

W_d = maximum charge per explosion (kg)

Gupta and Hartenberger (1981) examined seismic waves from surface explosions from two different geological areas in the United States and determined one equation for both sites. They mentioned 12 different ground-motion scaling models which do not consider the upward loss of seismic energy due to explosions on the surface. Many of the studies focus on PPV measurements, but two of the studies considered measuring the ground surface displacement of the seismic waves generated by the explosions. The two exceptions who considered displacement of the seismic waves are (1) Willis and Wilson (1960), who examined data collected from quarries within a few states of the United States and calculated an attenuation relation very similar to the above mentioned equations, and (2) Koper *et al.* (2002) measured the peak displacement of the first ground motion arrival when studying the seismoacoustic data from truck bomb experiments.

New (1991) plotted the variation of PPV against scaled distance and found that the PPV's recorded during the construction of a major road tunnel were generally lower and much more scattered than the pre-construction site investigation trial-blasting. However, the upper-bound equation did provide an excellent prediction of the maximum PPV's actually observed. The variation of PPV with distance, R, and charge weight, W_d, were examined individually and found that whilst the PPV's were very clearly dependent on distance, no such well-defined relationship was apparent for the charge weight. In addition, during a study by Ozer (2008), the various qualities of the geology within the area were examined in order to create predictive equations, based on the USBM equation, specific to those geologies along the Kadikoy-Kartal tunnel in Turkey. However, they explained that the equations are not always reliable and can also produce erratic results due to effects, such as geological variation, on ground motion.

Yan *et al.* (2009) acknowledged the fact that PPV is used to evaluate the risk of blasting-induced seismicity and that there are a number of empirical formulae available that measure the main factors influencing the intensity of the ground vibrations, i.e. quantity of explosive and distance from the blast. However, ground vibrations are far more complex. Yan *et al.* (2009) proposed the use of an artificial neural network to predict the PPV, but their results were once again very site specific and relied on simplified data.

Redmayne and Turbitt (1991), when studying the effects of the Lockerbie plane crash, stated that the seismic signature of the event was very similar to other shallow sourced events (such as quarry and underground-mining related events), having distinct surface waves and lower dominant frequencies than natural earthquakes. For earthquakes it is generally observed that the PPV's of horizontal component are greater than the vertical by a factor of between two and three. Ford *et al.* (2014) utilised measurements of the seismoacoustic wavefield to develop a quantitative understanding of the energy partitioning in order to determine the yield and emplacement of explosions near the surface (both buried below the surface and above the surface of the ground). They were only interested in local distances (<10km) where the collective effects of the radiation pattern (e.g. geometric spreading, scattering and attenuation) are reduced compared to regional or teleseismic distances. In addition, they mentioned that of the three seismic observables (displacement, velocity and acceleration) only displacement legitimately follows cube root scaling.

Kitov *et al.* (1997) described and analysed the recorded seismic and atmospheric acoustic data from bombs dropped by aircraft at a bombing range near Kustanai, Kazakhstan. Some bombs exploded high above (approximately 5 m) the ground, while others only exploded after penetrating 15m underground. They noted that a variety of different types of waves are produced from these blasts both within the ground and the atmosphere. Similar waves are produced by bolides (fireballs) when they explode in the atmosphere (*pers. comm.* Prof R. Gibson, University of Witwatersrand). On the other hand, Koper *et al.* (2002) examined the seismic and atmospheric acoustic data from truck bomb explosion experiments. As with the previous authors, they stated that seismic waveforms are more complex than atmospheric acoustic waveforms due to the geological structure of the ground and will cause the scaling laws to be site specific. Variations in the anelastic structure, which can depend on subtle features such as water table depth, may indirectly degrade the accuracy of seismic scaling laws. Peak displacement of the first seismic arrival, low frequency asymptote of the displacement spectra, corner frequencies and decay rates were analysed for the seismic properties, but only the first two properties performed well during their study.

Bonner *et al.* (2013) monitored calibration explosions on the surface of the ground at a military range in Israel, which they recorded with high pressure sensors, accelerometers on the surface, buried seismometers, acoustic gauges and high speed cameras. As with other authors, they reported that the seismic arrivals were quite complex. The topography of their study area was flat and was unlikely to create near-source topographic scattering. They found that the seismic amplitudes for the above ground shots are very similar to the amplitudes of the shallowest buried shots. As with Koper *et al.* (2002), they utilized the peak displacement of the first seismic arrival.

From the above studies, it is clear that the most commonly used measurement for prediction equations of buried explosions is PPV. However, a few authors preferred peak displacement of the seismic waves and of the first seismic arrival.

2.3 Prediction equations for explosions in the air or on the ground

Williams and Newell (1991) stated that when a high explosive detonates within the atmosphere, an increase in pressure, known as the blast wave is created. The blast wave moves away from the centre of the blast as a spherical wave front, whose peak overpressure is inversely proportional to the cube root of the distance from the blast. Different types of detonations and weather conditions can affect the overpressure, which may cause complaints usually attributed to ground vibration. In addition, it is known that the energy released by a surface explosion may also vary with the soil conditions. Concurrent to the overpressure, a blast wave is set in motion which subjects an additional pressure on any building it confronts. Blast parameters for a surface blast can be obtained by applying an amplification factor of 1.8 to data for an air burst. This factor is derived by assuming that the immediate reflection of the blast wave at the ground surface gives an amplification of 2.0, and that 10% of the explosive energy goes into cratering.

Quest Consultants (1999) examined explosions resulting from the ignition of a cloud of flammable vapor, gas, or mist in which flame speeds accelerate to sufficiently high velocities to produce significant overpressure. However, when comparing these explosions with high explosives occupying small volumes, the cube root scaling law is widely accepted because all high explosives tend to

produce similar blast waves, with the waves appearing to originate at a point within the small volume. Ford *et al.* (2014) examined blast characteristics at local distances and noted that the overpressure mostly behaves as a shock wave obeying hydrodynamic scaling and little atmospheric variability. At longer range, the atmospheric overpressure transitions to infrasound.

Evers *et al.* (2007) utilized the seismograms (Figure 2) from seismic stations to plot the distance vs time of waveforms generated by the explosion of a high pressure gas line in Belgium. They concluded that since the calculated speed was 346m/s, the wave in question was either an acoustic-infrasound or an air-coupled Rayleigh wave. On studying the particle motion of the wave, it was found that the motion was retrograde which is normally produced by an air-coupled Rayleigh wave. Since most of the energy went into the atmosphere as infrasonic energy during the explosion, there was a lack of clear P onsets, however, the first seismic arrival was determined to have travelled at a speed of 5km/s and was thus as a P-wave. The seismic arrival data was then used to accurately determine the time of the explosion.

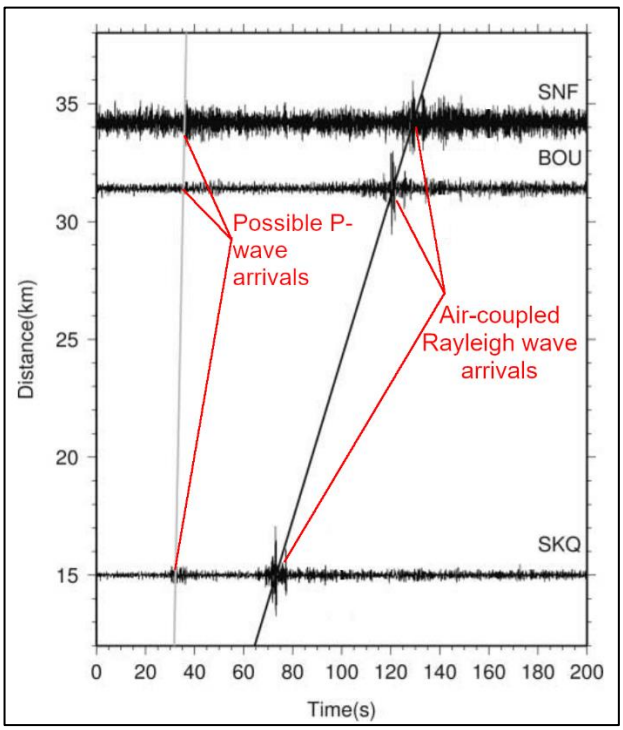


Figure 2. Seismograms modified from Evers et al. (2007) indicating the P-wave arrival and air-coupled Rayleigh waves.

Johnston (1987) examined the seismograms created by a missile silo explosion and noted that large arrivals were recorded over an eleven-minute interval as opposed to a scatter of less than one minute which is expected for P-wave arrivals. The missile silo explosion was 84km west of the station which registered the event four minutes later. There was no trace of P- or S- waves, probably because most of the energy went into the atmosphere, but there were very small signals at the stations on hard rock. The larger amplitude and longer duration signals at the other stations are a mixture of the nearly simultaneous arrivals of the atmospheric acoustic waves and the air-coupled surface waves that were generated by the advancing shock front and propagated to the station with the same velocity. He measured the velocity of the arrivals and calculated a speed of 338m/s, which is within the range of the speed of sound in the air. These arrivals were interpreted as being air-coupled surface waves, but Johnston (1987) could not confirm this interpretation by particle motion analysis because his records were from one-component stations. Johnston (1987) stated that air-ground coupling is significant only when the speed of sound in air is close to the shear wave velocity on the surface crustal layer. This is normal only in the case when unconsolidated material is present at the surface. Seismic instruments sited on soft ground record signals from atmospheric disturbances more clearly than higher gain instruments on hard rock.

Koper *et al.* (2002) examined the seismic and acoustic data from truck bomb explosion experiments. They used pressure gauges, similar to infrasound barometers, to measure the air blast properties in order to determine which property could be reliably used as a yield indicator for uncontrolled explosions of varying size. They analysed peak overpressure, blast wave impulses, pulse duration and air blast travel times and concluded that “velocity at which a shock wave travels is a function of the source magnitude and the elastic structure of the medium through which it propagates”. Thus, there is a change in the speed of the shock wave as it loses energy and decays into an elastic wave. Koper *et al.* (2002) concluded that the most reliable acoustic property is the impulse per unit area delivered by the air blast.

Bonner *et al.* (2013), Gitterman and Hofstetter (2012) and Gitterman (2013) monitored calibration surface explosions at a military range in Israel with high

pressure sensors, accelerometers on the surface, buried seismometers, acoustic gauges and high speed cameras. They examined the secondary shock arrival using seismometers. The data examined were from three large scale (100 tons) surface explosions, one in summer and the other two in winter. They developed a unique empirical scaled relationship for the secondary shock (SS) delay for ANFO (ammonium nitrate/fuel oil which is a widely used bulk industrial explosive) charges and distances. The obtained relationship can be used as a new yield estimator.

The secondary shock (SS) delay phenomenon (Figure 3) occurs when the air blast wave for an explosion source displays a number of recurrent shocks of smaller magnitudes and at different times, caused by successive implosion of rarefaction waves (the region of low relative pressure following a shock wave). Tertiary shocks of this nature have also been observed (Figure 4). Since the overpressure increases with the amount of explosives used and higher pressure shock fronts travel faster, the time delay between the main shock (MS) and the SS phase increases with distance, as well as with the amount of explosive. Thus longer secondary shock delays are observed for longer distances, as well as for larger amounts of explosives. They noted that the ambient temperature and pressure (altitude) would lead to only minor changes in the air blast parameters and thus did not consider them within the distance and SS delay scaling relations. The empirical relationship developed for secondary shock delay (the time between secondary shock and main shock arrivals) is dependent on charge and distance, as are standard air blast parameters, but also on the type of explosive (velocity of detonation).

The secondary shock wave starts close to the charge boundary, but during their experiments the pressure sensors did not register the secondary shock wave closer than 100m to the centre of the blast. The reason for this is probably that at short distances the secondary shock wave arrives during the main shock positive phase because the secondary shock delay is still small. Consequently, superposition of the main and secondary shocks would not result in a clear secondary shock arrival, as in the case of late secondary shock arrivals at larger distances (Figures 5 and 6), where they occur during the main shock negative phase, which is comparable to the secondary shock peak pressure.

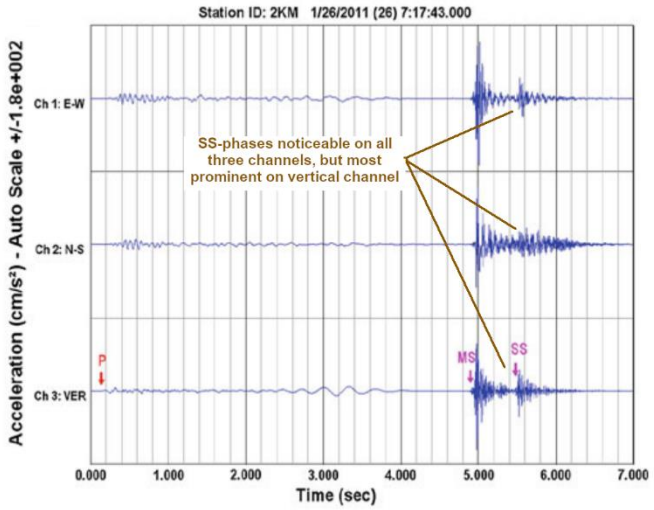


Figure 3. Waveforms recorded by a 3-component accelerometer modified from Gitterman (2013).

P – Primary seismic wave, MS – Main shock and SS – Secondary shock

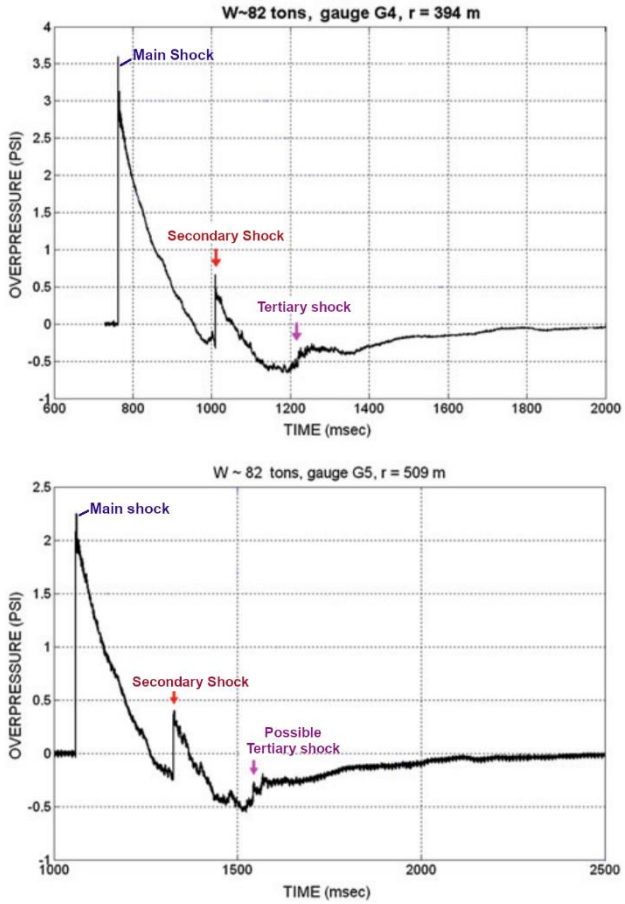


Figure 4. Overpressure records modified from Gitterman (2013).

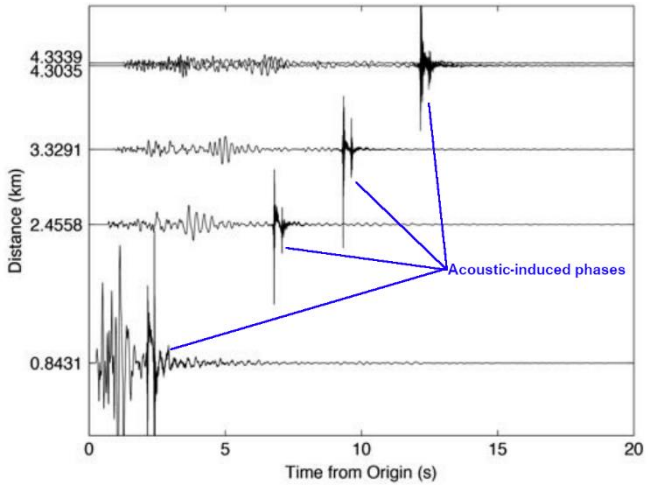


Figure 5. Seismograms of the vertical channel from stations at distances from 0.8 to 4.3 km modified from Bonner et al. (2013).

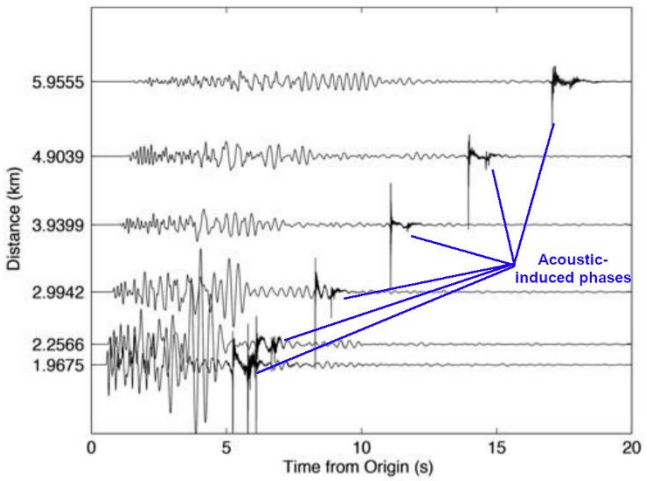


Figure 6. Seismograms of the vertical channel from stations at distances from 2 to 6 km modified from Bonner et al. (2013).

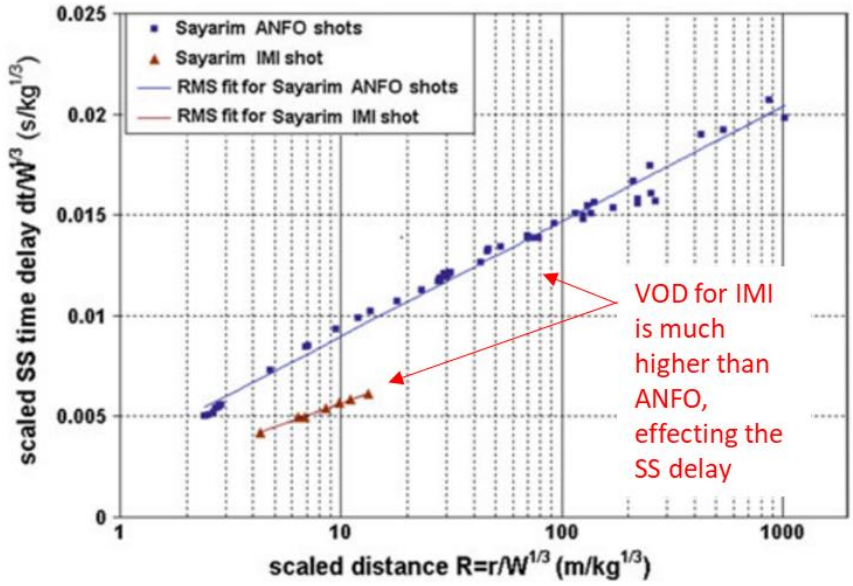


Figure 7. Comparison of ANFO and IMI explosives and the effect on the SS delay, modified from Gitterman (2013).

Gitterman (2013) noted, when examining other detonations, that there was an increase of the secondary shock delay with the amount of explosives used and a decrease of the velocity of detonation (VOD) of the explosives (Figure 7). This was observed due to the time of complete detonation of the finite charge. They noted these differences between the tests and the VOD of the explosives (they compared ANFO with IMI, which is a military explosive), but acknowledged that there may be other explosive parameters that can affect the delay. This new method may be less accurate than that of the traditional procedures, based on high pressure measurements, but it is significantly less expensive, and, in the case of an accidental explosion, may be the only method available. It should work well when determining the relative size of two charges of the same explosive.

There is very little literature available on utilising seismograph systems to determine prediction equations for atmospheric waves created by explosions above or on the surface of the Earth. However, the SS delay is a unique parameter that can be examined by both pressure gauges and seismograph systems and could prove very useful for predicting if records from either of the sensors are not available.

3 Methodology

3.1 Monitoring of seismic signals

This analysis aims to follow methods similar to those undertaken within the case studies described in section 3.3 and performed by Aloui *et al.* (2016), Bongiovanni *et al.* (1991, Khandelwal and Singh (2007), Kahriman (2002), Ozer (2008), Ozer *et al.* (2008) and Puri and Prakash (1991).

Five different military demolition ranges were monitored by a mobile network of seismograph stations in order to develop an empirical relation for the prediction of PPV's from on-surface blasting, which can then be used for other demolition ranges with similar properties. The results of the three different vibration equations, as listed in Table 1, were then compared in order to determine the most favourable vibration prediction equation.

In addition, the data was analysed in order to verify statements by Ford *et al.* (2014), who concluded that only displacement legitimately follows cube root scaling, when one examines displacement, velocity and acceleration.

The monitoring of the blasting was performed using a temporary mobile network of between 5 and 12 seismograph stations consisting of a combination of 4.5 Hz triaxial geophones and 1 Hz triaxial seismometers installed on the surface of the ground (Figure 8) at varying distances from the source. The number of stations used was dependant on the local site conditions and accessibility. The stations were typically located at dwellings or structures encircling the range, similar to the map in Figure 9. Five different military demolition ranges were used during the experiments and the local geology for each range is briefly described in Table 2. Due to the sensitivity of the sites, the precise locations are not provided. For sites 1-4, the distances between the explosions and the sensors varied between 0.1 – 5.5 km; however, at site 5, the sensors were placed at distances of 5.25 – 29 km because of the accessibility of suitable locations.

The manufacturer's calibration values for the instrumentation were verified before

the experiments during a test calibration on the seismometers. The difference between the manufacturer's specifications and the laboratory verification was small enough that the manufacturers' calibration values for the seismographs were used to convert the recorded seismograms to true ground motion



Figure 8. Typical installation of stations within the mobile network.

The use of triaxial sensors were used to measure the ground motion to ensure recording in three mutually perpendicular directions. The goal of the method is to fully records complete vibrations in the earth. These sensors are thus in accordance with the requirements set out in the United States Code of Federal Regulations (30 CFR part 816.67 of 1998) which deals with the control of adverse effects caused by the use of explosives. The SEISAN earthquake analysis software (Havskov and Ottemöller, 2001) was used to determine the peak particle velocities and displacements for each explosion and for each station. Throughout the study, only the vertical component of the sensors was utilised for all the measurements within both the ground monitoring and atmospheric shock wave monitoring analyses. This was to ensure that the same data were utilised during all analyses because the atmospheric shock wave monitoring displayed the strongest and clearest signal on the vertical component of the sensor as experienced by Bonner *et al.* (2013), Gitterman and Hofstetter (2012) and Gitterman (2013). All measurements obtained from the sites may be found in Appendices A to E.

As per the studies performed by Aloui *et al.* (2016), Bongiovanni *et al.* (1991,

Khandelwal and Singh (2007), Kahriman (2002), Ozer (2008), Ozer *et al.* (2008) and Puri and Prakash (1991), the amount of explosive used and the distances between the source and stations were carefully recorded. The explosives used were those scheduled for destruction and they were then heaped on the surface of the ground and detonated. Typically the amount of explosives varied between 5 and 1000kg for most sites, but at site 5 the amount of explosives used reached 25000kg allowing the monitoring of the resulting ground motion at distances up to 29 km. The number of detonations that occurred per day was dependant on the size of the explosives used, thus for the large 25000 kg blast that was detonated at site 5, it was the only detonation for the day because it took a number of hours to setup. Thus, there could be as many as 10 detonations during one day if the amount was small in size.

Three PPV-based predictor equations chosen from a number of equations proposed in literature were utilised: (a) the United States Bureau of Mines (USBM) equation, (b) the Ambraseys-Hendron equation (Ambraseys and Hendron, 1968) and (c) the Langefors-Kihlstrom equation (Langefors and Kihlstrom, 1963), to establish a relationship between PPV and scaled distance (SD) (see Table 1 for the predictive equations).

A linear RMS fit regression curve of the logarithm of PPV against the logarithm of SD was obtained for each of the explosions and each of the stations. In order to find the site constants, the graph between PPV values and SD were plotted for all predictor equations along with the 95% mean prediction interval. The coefficient of determination (R^2) was calculated as it is a quantity which is generally accepted as a basic measure of the quality of the fit. This method was followed for the peak displacement and first arrival displacement measurements as well. All calculations were performed using Matlab software.

As mentioned, the Ambraseys-Hendron equation utilizes the cube root SD, and the USBM equation utilizes the square root SD. The Langefors-Kihlstrom equation is slightly different in that the weight of the explosives is divided by the distance and thus produces a positive slope when plotted, which differs from the negative slopes produced by the other two equations (see Table 1 for the predictive equations).

In Table 1, the constants K and β are site constants that vary between sites and are dependent on the nature of the rock and the type of explosive. K (the ground transmission coefficient) represents the line intercept at SD=1 on the log-log graph and it is the initial energy radiated into the immediate rock and thus is reliant on the features of the medium and the explosive used. β (the specific geological constant) is a slope factor that provides an indication of the attenuation rate of the PPV caused by the geometric spreading and the effect of specific characteristics of the rock (Aloui *et al*. (2016) and Puri and Prakash (1991)).

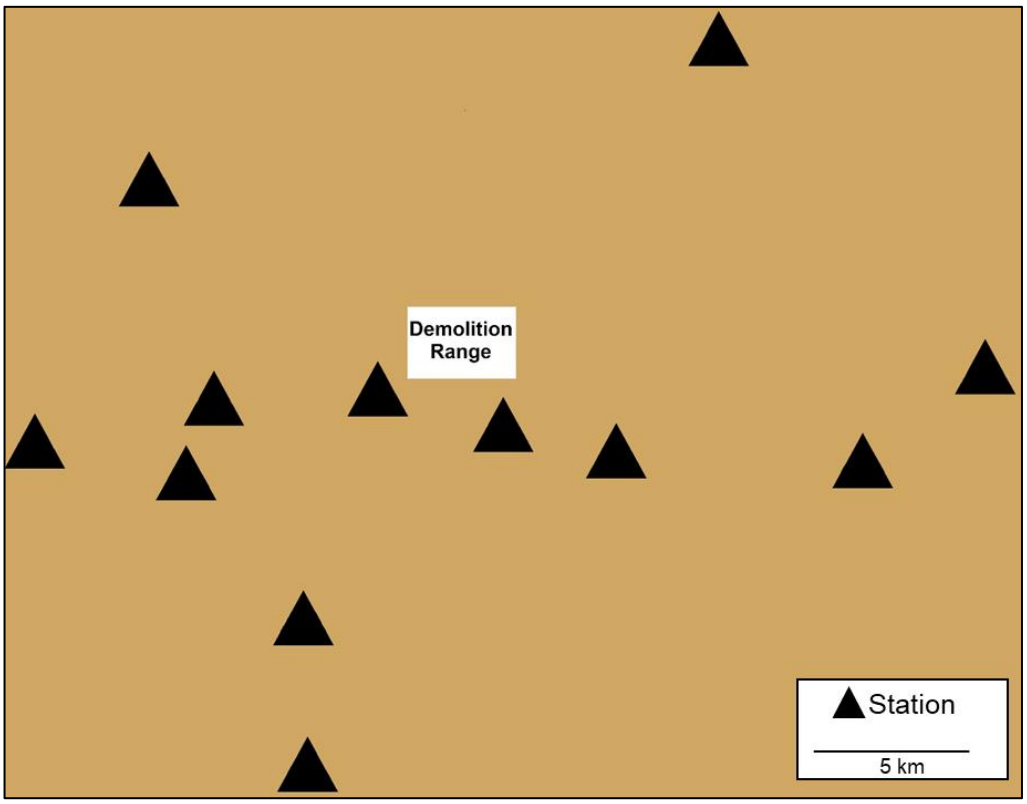


Figure 9. Indication of a typical station distribution in and around the demolition ranges at each site.

Table 2. The geological description at each of the sites

Site	Geology
Site 1	Situated on the Tierberg Formation, Ecca Group. The Tierberg Formation is a blue-grey to black shale with carbonate-rich concretions, subordinate siltstone and sandstone in the upper part. Just south of the site is the contact with the younger Abrahamskraal Formation, Adelaide Subgroup, Beaufort Group. The Abrahamskraal Formation is predominantly a blue-grey silty mudstone, with subordinate brownish-red mudstone and sandstone. Dolerite is abundant and overlaying much of the area. Some Tertiary to Quaternary calcrete was delineated and alluvium covers most of the drainages.
Site 2	The area under investigation is mostly underlain by volcanic and sedimentary rocks of the Ventersdorp Supergroup, shale of the Prince Albert Formation of the Karoo Supergroup and Quaternary sand, calcrete and alluvium. Most of the central, southern and eastern portions are situated on a low plateau underlain by the volcanic rocks. The remaining western portion of the area forms part of the relatively lower lying, eastern side of the Vaalharts valley which is predominantly underlain by sand, calcrete and shale.
Site 3	The area is underlain by Karoo Supergroup rocks developed in the Roedtan sub-basin. The rock units dip shallowly towards the west. The surface rocks are dominantly fine-grained locally amygdaloidal basalts of the Letaba Formation. However, at this southern end of the basin, these volcanic rocks are not thick and this, together with the proximity to faulted basin margins, has resulted in areas of the underlying fine-grained reddish sandstones of the Clarens Formation being exposed. In rare instances even the shales of the Irrigasie Formation below the sandstones crop out, but their extent is very limited. There are localized occurrences of clay (attapulgite) and gypsum associated with weathered basalts.
Site 4	The site lies on Hout River Gneiss, a metamorphosed granitic rock which includes a number of remnants of intruded greenstone belt material. The structural trend of the gneisses and greenstone belt rocks is variable, but on the scale of kilometres they can be regarded as being homogeneous. Diabase dykes are prevalent in the area, and trend in a north-easterly direction. As is typical for the region, the area is essentially sand covered and outcrops of gneissic rock are scarce.
Site 5	The site is underlain by the Proterozoic Groblershoop Formation, the Wilgenhoutsdrif, Koras and Nama Groups; and rocks of the Phanerozoic Karoo Supergroup. Aeolian sand of the Gordonia Formation of the Kalahari Group covers about 90% of the area. Karoo dolerite and kimberlite occur in the area and structural deformation, seen as folding, is restricted to the Proterozoic rocks.

3.2 Monitoring of atmospheric signals

Another major aim of this analysis was to follow similar methods to those performed by Koper *et al.* (2002), Bonner *et al.* (2013), Gitterman and Hofstetter (2012), Gitterman (2013) and Ford *et al.* (2014), but using the data obtained from the

mobile network of temporary seismograph stations described in section 2.1. Although, the above authors utilized high pressure sensors, accelerometers on the surface, buried seismometers, acoustic gauges and high speed cameras, Bonner *et al.* (2013), Gitterman and Hofstetter (2012) and Gitterman (2013) examined the secondary shock delay using seismograph stations similar to the ones installed in this current study. In addition to the secondary shock delay, the displacement recorded by the stations of the atmospheric shock wave was also examined within the current study in order to determine if there was a good correlation with SD.

Bonner *et al*. (2013), Gitterman and Hofstetter (2012) and Gitterman (2013) examined data from three large-scale on-surface explosions, one in summer and the other two in winter. The explosives were packed on dry desert alluvium. They used ANFO and military explosives (IMI) with different velocities of detonation (IMI VOD is 7130 – 7980 m/s and ANFO is 2400 m/s). The VOD for the explosives used in this current study ranged from 3000 m/s to 10 000 m/s, depending on the type of explosive used, and falls within the same range as the military explosives used by Bonner *et al.* (2013), Gitterman and Hofstetter (2012) and Gitterman (2013).

The SEISAN earthquake analysis software (Havskov and Ottemöller, 2001) was used to calculate the delay in seconds between the visually determined onset of the main atmospheric shock wave (MS) and the SS wave (Figures 10, 11 and 12). In figures 10 – 12, the horizontal line at the start of the plot is the DC level. The small number above each trace to the right is the maximum absolute count with the DC-level subtracted and the small number to the left above the trace is the DC level.

The following formula was used to plot the measured scaled SS time delay (Dt) against the scaled distance:

$$Dt=\Delta t/W_d^{0.33}$$

Where:

Dt is the scaled SS time delay

Δt is the measured delay in seconds

W_d is the amount of explosive in kg

$$SD=R/W_d^{0.33}$$

Where:

SD is the scaled distance

R is the distance in metres from the explosion to the station

W_d is the amount of explosive in kg

A linear RMS fit regression curve of the scaled SS time delay against the scaled distance was then obtained for the explosions. The R^2 was calculated as it is a quantity which is generally accepted as a basic measure of the quality of the fit. All calculations were performed using Matlab software.

As mentioned in Bonner *et al.* (2013), Gitterman and Hofstetter (2012) and Gitterman (2013), small differences in the air temperature and altitude for different explosions were considered to cause negligible variances in air blast parameters, comparable with measurement errors of distance and wave parameters.

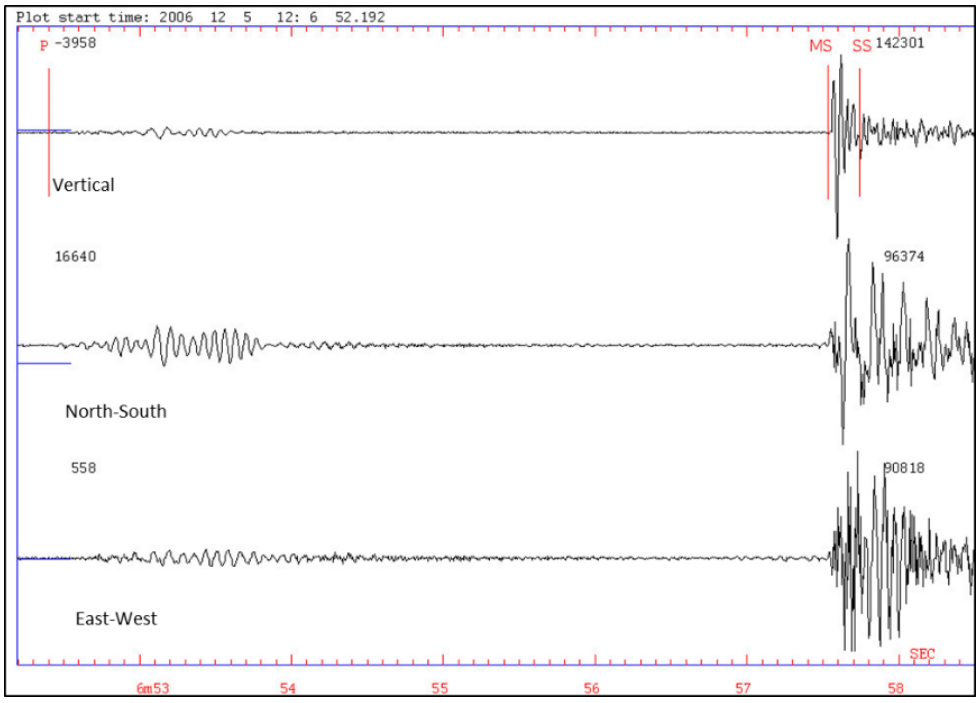


Figure 10. Example of the signal registered on all three components of a station 2.14km from the demolition range.

"P" indicates the P-wave arrival, "MS" the main shock and "SS" the secondary shock.

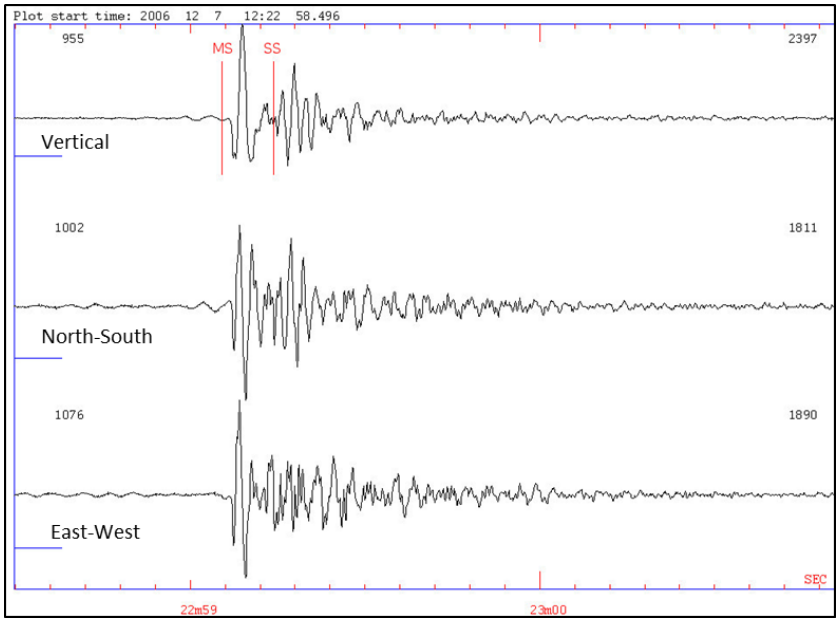


Figure 11. An example of the signal registered on all three components at a station 4.89km from the demolition range

The P-wave arrival was not recorded but the main shock ("MS") and secondary shock ("SS") were recorded.

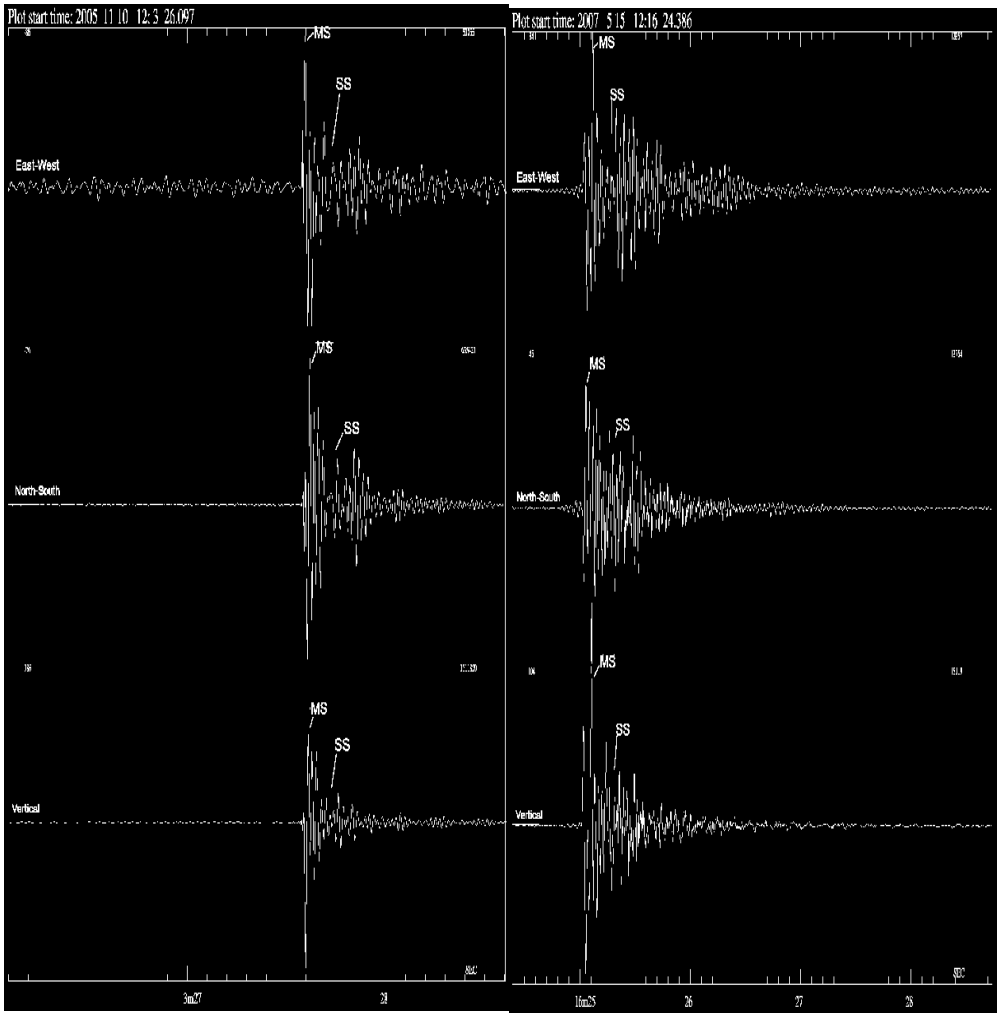


Figure 12. Example of the signal registered on all three components of stations 12.37km (left) and 3.6km (right) from the demolition range

"MS" indicates the main shock and "SS" the secondary shock.

4 Results

4.1 Ground monitoring

4.1.1 PPV predictive equations

All of the graphs of log PPV versus log SD for each of the sites are shown in Figures 13 – 17, displaying the 95% mean prediction interval. The largest PPV recorded was 0.485mm/s recorded for a 250kg explosion at a distance of 10m. However, this was only 2.5% of the 19mm/s limit set out in the United States Code of Federal Regulations (30 CFR part 816.67 of 1998), which deals with the control of adverse effects caused by the use of explosives (Figure 1). As was expected, since the readings were so low, no damage to the infrastructure in and around the station was observed. Figures 18-20 display the results from each of the sites on one graph per prediction equation. Table 3 summarises the results of the regression analyses and coefficient of determination (R^2) value for each of the sites and equations.

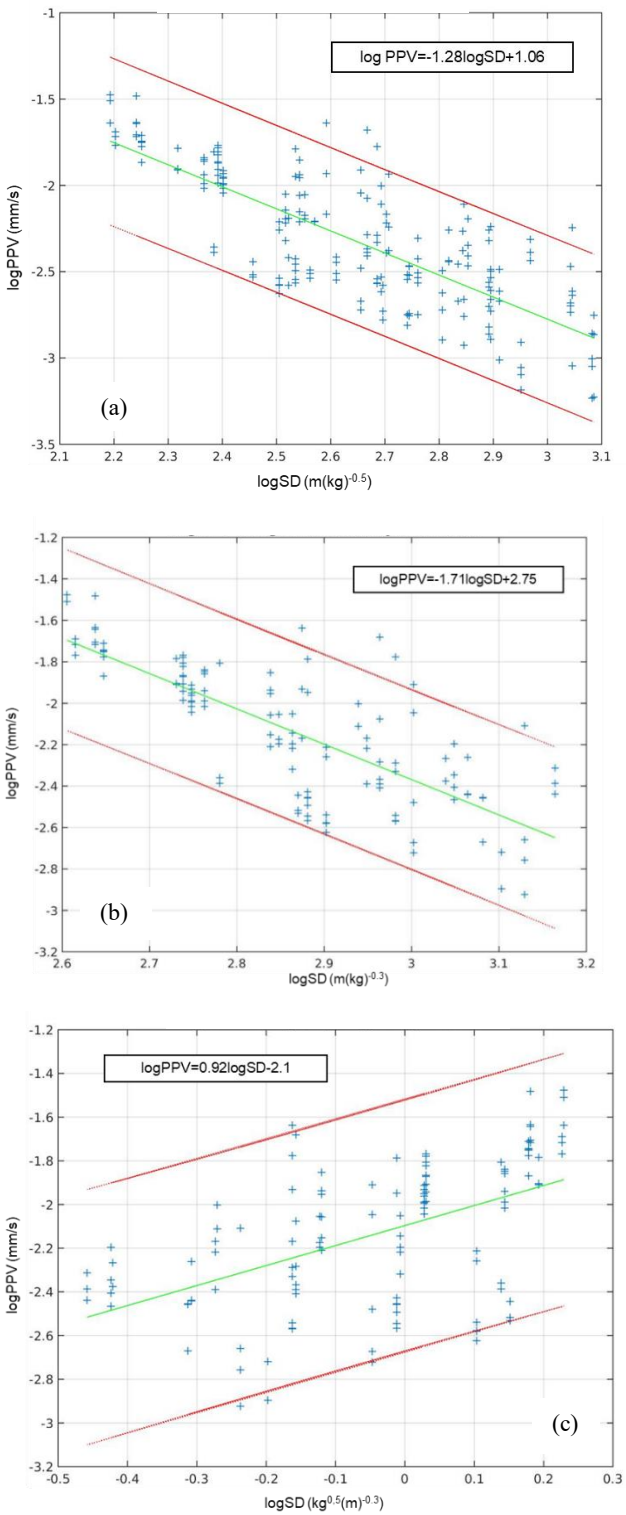


Figure 13. The relation between PPV and SD for site 1.

The green lines represent the best fit using the least squared method, and the red lines represent the 95% confidence range. The "+"symbol represents the recorded PPV. (a) = USBM, (b) = Ambraseys, (c) = Langefors.

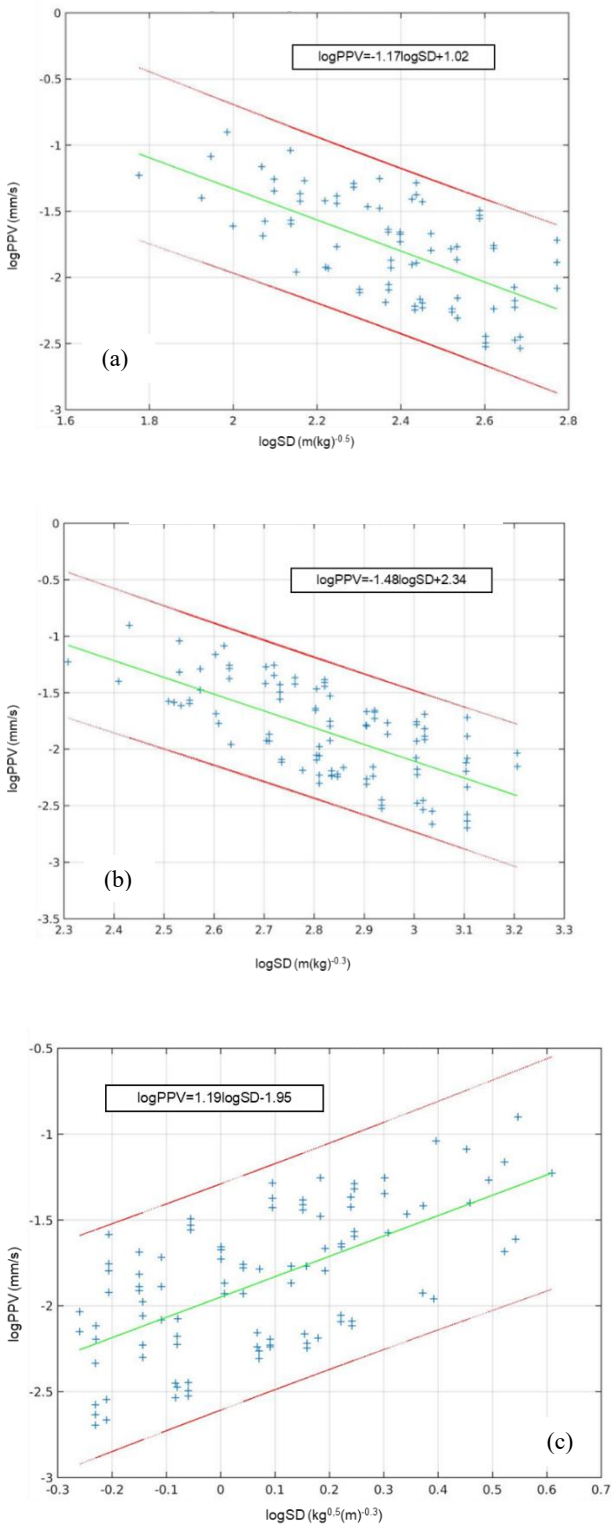


Figure 14.The relation between PPV and SD for site 2.

The green lines represent the best fit using the least squared method, and the red lines represent the 95% confidence range. The "+"symbol represents the recorded PPV. (a) = USBM, (b) = Ambraseys, (c) = Langefors.

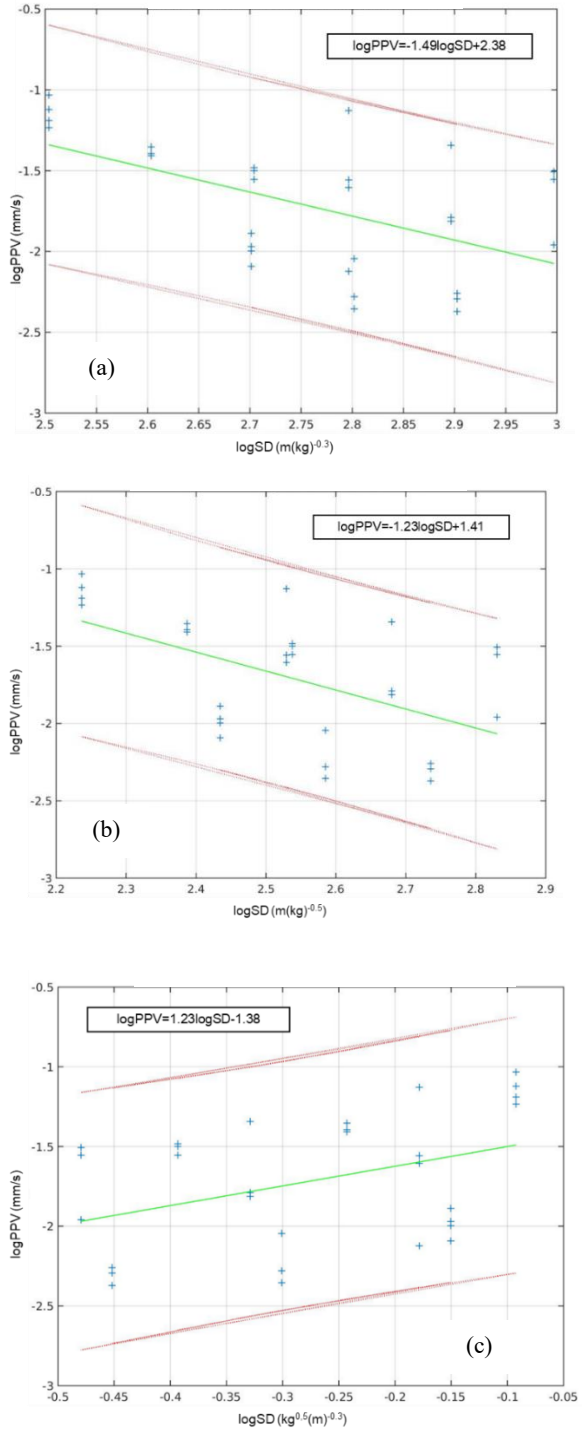


Figure 15. The relation between PPV and SD for site 3.

The green lines represent the best fit using the least squared method, and the red lines represent the 95% confidence range. The "+"symbol represents the recorded PPV. (a) = USBM, (b) = Ambraseys, (c) = Langefors.

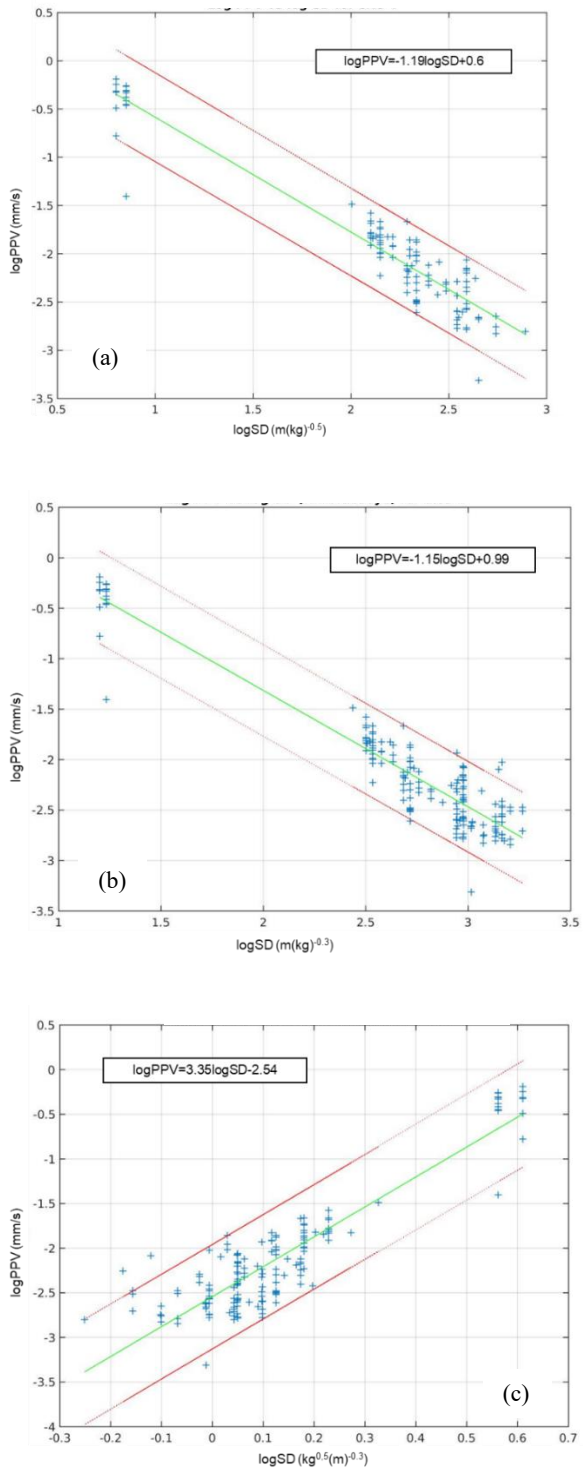


Figure 16. The relation between PPV and SD for site 4.

The green lines represent the best fit using the least squared method, and the red lines represent the 95% confidence range. The "+"symbol represents the recorded PPV. (a) = USBM, (b) = Ambraseys, (c) = Langefors. The gap in the data is due to the lack of stations within that range from the explosion.

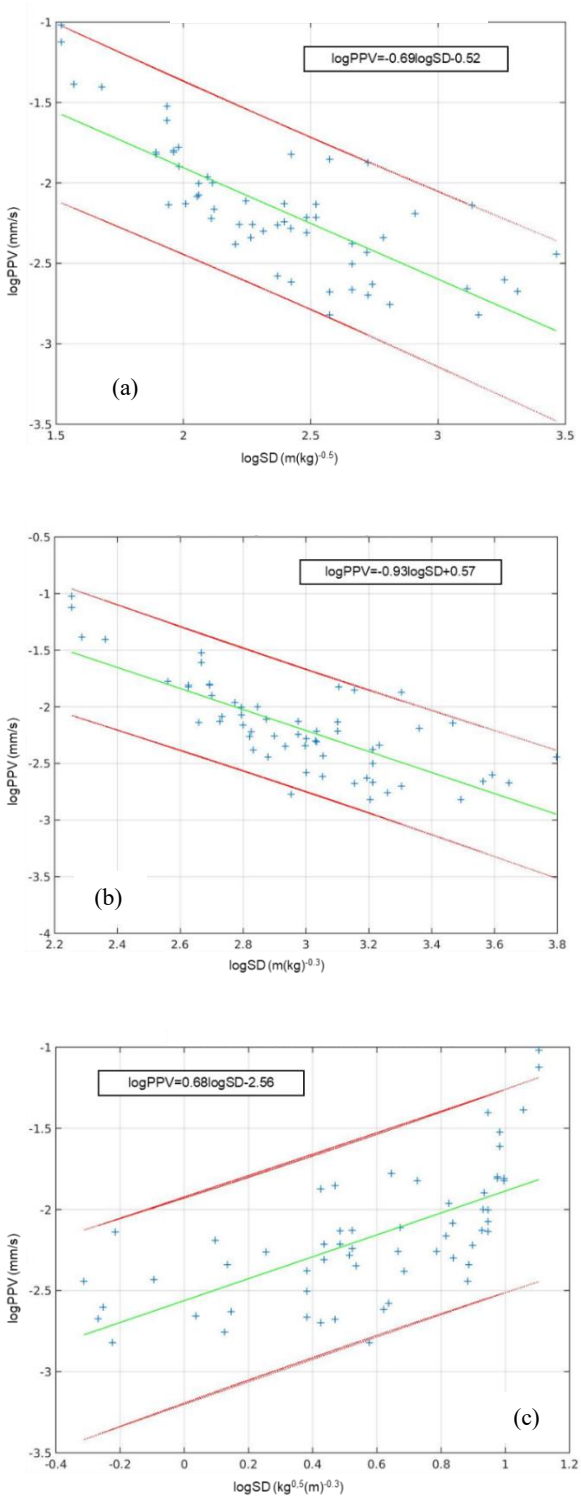


Figure 17. The relation between PPV and SD for site 5.

The green lines represent the best fit using the least squared method, and the red lines represent the 95% confidence range. The "+"symbol represents the recorded PPV. (a) = USBM, (b) = Ambraseys, (c) = Langefors.

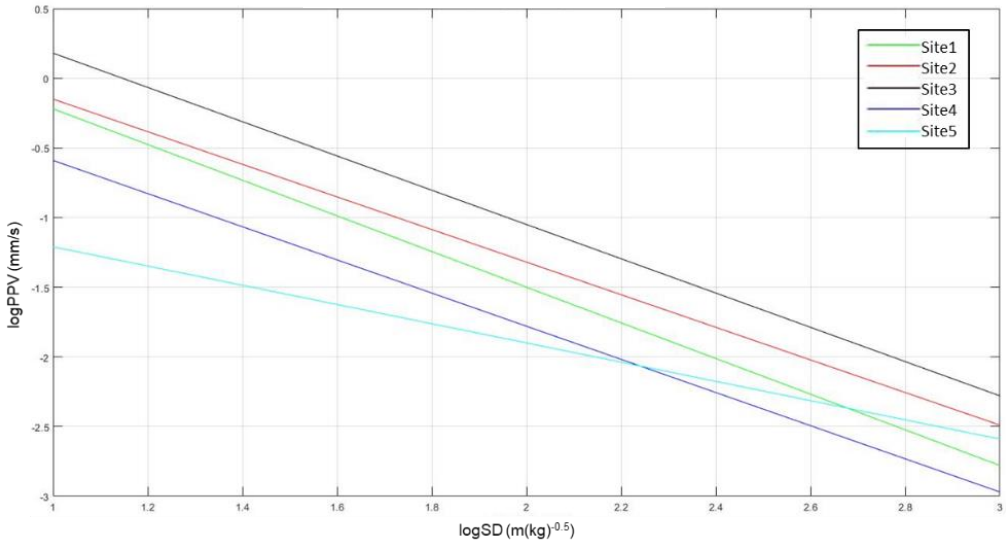


Figure 18. The results of the USBM equation for all five sites. The coefficients calculated for each site are listed in Table 3.

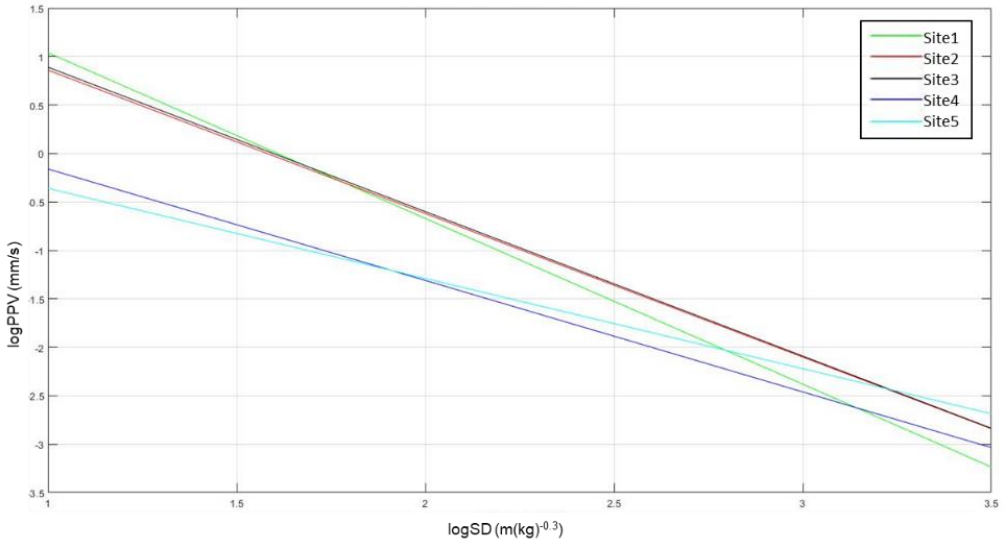


Figure 19. The results of the Ambraseys equation for all five sites. The coefficients calculated for each site are listed in Table 3.

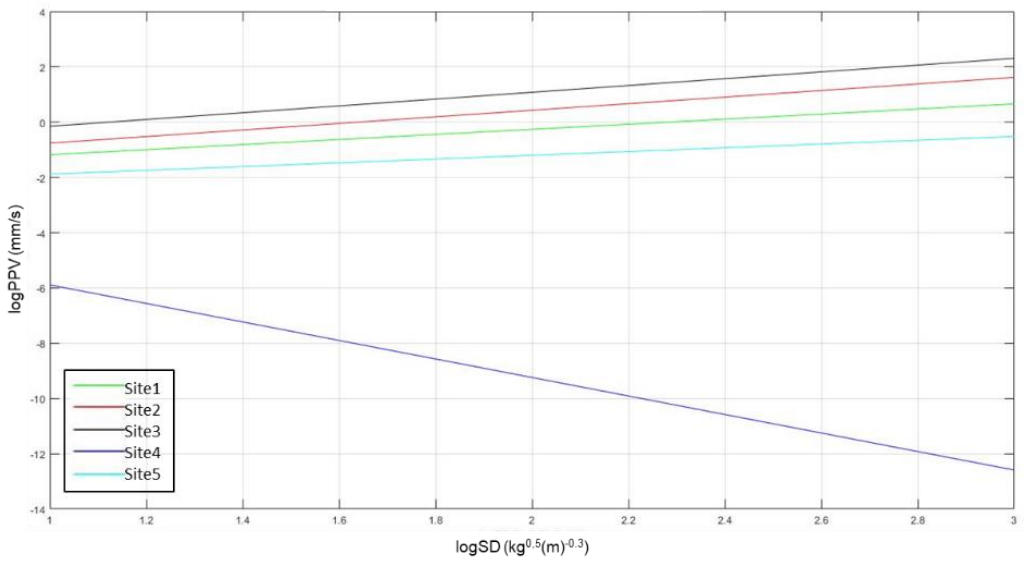


Figure 20. The results of the Langefors equation for all five sites. The coefficients calculated for each site are listed in Table 3.

Generally, from Table 3 one can notice that the Langefors-Kihlstrom equation for each of the sites exhibits the lowest value for the coefficient of determination (R^2) compared to the values obtained from the USBM and Ambraseys-Hendron equations. This result agrees with the findings of Bongiovanni *et al*. (1991), who concluded that since the data shows a poor correlation for Langefors-Kihlstrom, the equation is not reliable to predict motion produced by blasts at their site.

It is interesting to note that the highest R^2 values (greater than the generally accepted value of 0.7 (Kahriman, 2002)) for all three equations was for site 4, which is located on metamorphosed granitic rock. The other R^2 values were far lower.

Figures 18 - 20 provide a quick comparison of the results of each of the sites for each of the predictive equations and show that the sites correspond surprisingly well with each other, except site 5 for the USBM equations and site 4 for the Langefors equation. Interestingly, these two sites exhibit similar gradients for the Ambraseys equation and are different to the other three sites.

The results obtained from the USBM equation for site 1 in Table 3 are similar to Gupta and Hartenberger (1981), and the geology is similar to one of the sites which they studied.

Table 3. Empirical formulae for PPV, the Peak Displacement (Pk) and displacement of the first arrival (Fst) obtained from the five different sites. Table 1 displays the PPV equations and corresponding coefficients utilised.

	Site 1		***Site 2***	***Site 3***	***Site 4***	***Site 5***
Geology (see Table 2 for details)	Tierberg Formation of the Ecca Group.		Ventersdorp Supergroup; Prince Albert Formation of the Karoo Supergroup; Quaternary sand	Letaba and Clarens formations of the Karoo Supergroup	Hout River Gneiss. Letaba and Clarens formations of the Karoo Supergroup	Karoo Supergroup; Aeolian sand of the Gordonia Formation of the Kalahari Group
USBM	K	11.4	10.4	25.5	4.02	0.3
$PPV = K(SD)^{-\beta}$	β	1.3	1.2	1.2	1.2	0.7
R^2	0. 61		0.41	0.28	0.90	0.58
Ambraseys	K	562.3	220.3	240.2	9.79	3.75
$PPV=K(SD_A)^{-\beta}$	β	1.7	1.5	1.5	1.2	0.9
R^2	0.58		0.45	0.29	0.89	0.57
Langefors	K	0.01	0.01	0.04	0.003	0.003
$PPV=K(SD_L)^{\beta}$	β	0.9	1.2	1.2	3.4	0.7
R^2	0.27		0.39	0.15	0.81	0.43
USBM	K	$1.47e^{-04}$	0.01	0.001	$5.33e^{-05}$	0.082
$Pk = K(SD)^{-\beta}$	β	0.04	0.74	-0.06	0.10	0.84
R^2	-0.40		-0.83	0.83	-7.56	0.15
Ambraseys	K	$7.75e^{-06}$	0.01	0.001	$3.98e^{-05}$	0.769
$Pk=K(SD_A)^{-\beta}$	β	-0.50	0.56	-0.07	0.04	0.99
R^2	-2.90		-1.97	0.83	-8.22	0.00
Langefors	K	$2.22e^{-04}$	$2.64e^{-04}$	0.002	$2.57e^{-05}$	2.8e-04
$Pk=K(SD_L)^{\beta}$	β	-0.45	0.60	-0.09	0.70	0.88
R^2	-4.83		-1.55	-0.12	-36.55	-0.33
USBM	K	0.02	0.04	$3.60e^{-04}$	$7.44e^{-06}$	0.01
$Fst = K(SD)^{-\beta}$	β	1.22	1.15	0.32	0.04	0.89
R^2	-0.49		-0.82	0.76	-3.71	-0.18
Ambraseys	K	0.61	0.74	$4.06e^{-04}$	$1.10e^{-05}$	0.12
$Fst=K(SD_A)^{-\beta}$	β	0.69	1.47	0.32	0.02	1.14
R^2	0.65		-1.94	0.75	-4.34	-0.16
Langefors	K	$1.24e^{-05}$	$4.59e^{-05}$	$1.17e^{-04}$	$1.02e^{-05}$	$6.72e^{-05}$
$Fst=K(SD_L)^{\beta}$	β	-0.83	1.48	0.96	-0.54	0.82
R^2	-3.00		-1.72	-0.86	-16.87	-1.2

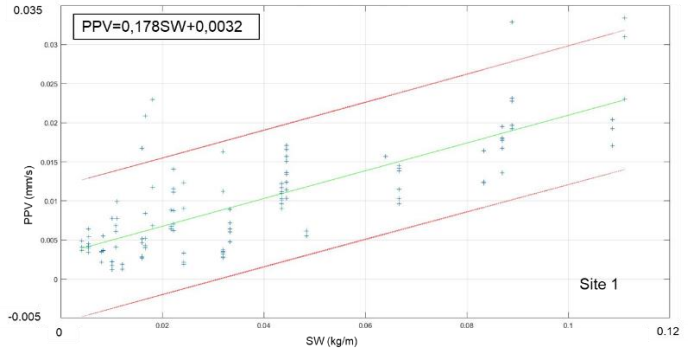
.

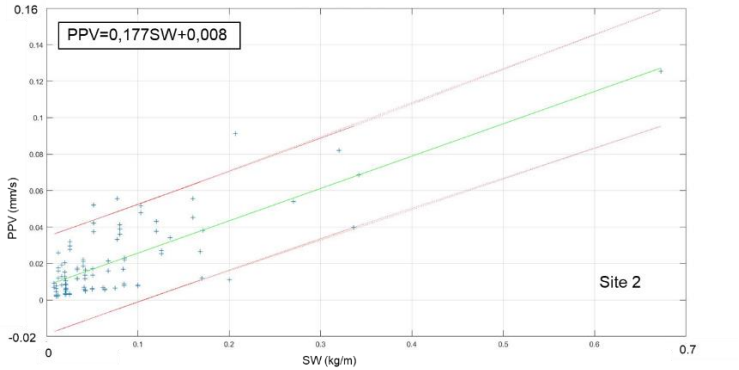
When surveying the results obtained in Figure 13-17, one can observe that there is a fair amount of scattering, which is similar to Kumar *et al.'s* (2016) observations, but they mentioned that the equations still provide a fair prediction of PPV.

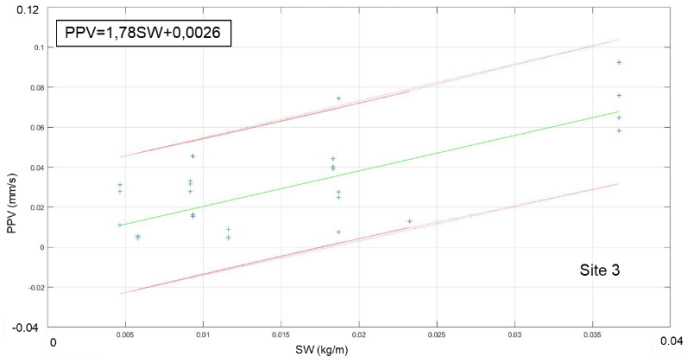
From Table 3 and Figures 18-20, it is clear that the geological constants (β) for sites 1, 2, 3 and 4 are similar for the USBM equation and sites 2 and 3 for the Ambraseys and Langefors equations. The ground transmission coefficient (K) for each relation for site 5, compared to the other sites, is expected to be low due to the sandy conditions of the region.

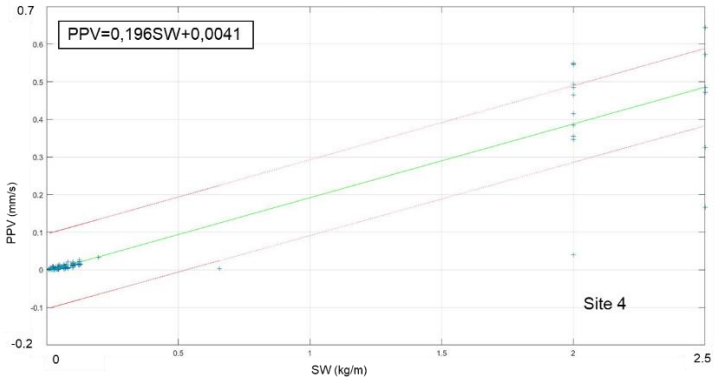
In an effort to find equations which produced higher coefficients of determination (R^2), the equations were then modified slightly by removing the logarithms and exponents and only utilising the observed values obtained from the measurements. Figure 21 displays the graphs of PPV versus the scaled weight (SW) for all five sites separately and Figure 22 displays the combined results for all five sites. Table 4 displays the resultant formulae and R^2 for all the five sites.

However, when comparing Tables 3 and 4, one notices that there was a decrease in R^2 for all the sites except site 5. Site 4 displays the highest R^2 values while site 3 displays the lowest R^2 values. Site 3 has the steepest gradient as seen in Figure 22(a). Figure 22(a) displays the results along the SW range between 0 and 0.04 kg/m. as was recorded for site 3 in Figure 21. Figure 22(b) displays the same results as Figure 22(a) but without site 3 because it deviates significantly from the other sites. In addition Figure 22(b) covers a SW range of 0 to 5 kg/m (which was the highest result obtained in Figure 21 for site 5). From Figure 22(b) it is noticeable that for sites 1, 2 and 4, the gradients are very similar. Site 5 displays a gentler gradient.









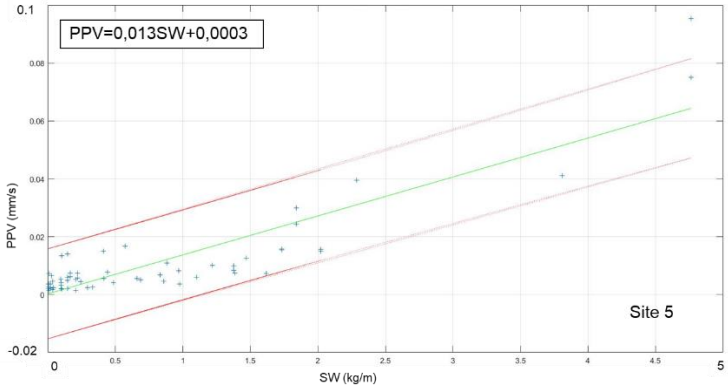


Figure 21. The relation between PPV and SW for all 5 sites. The green lines represent the best fit using the least squares method, and the red lines represent the 95% confidence range. The "+"symbol represents the recorded PPV.

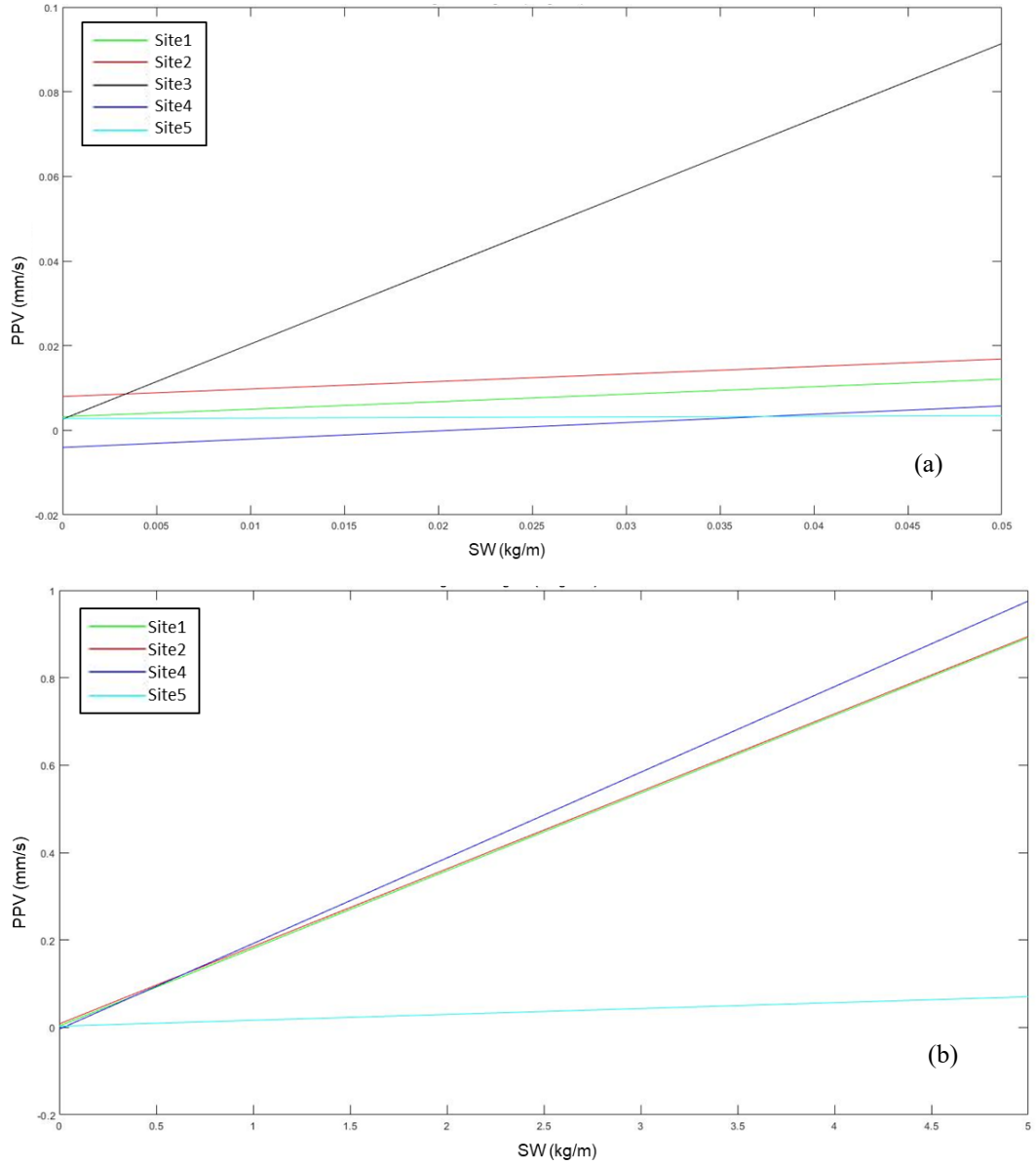


Figure 22. The results of the PPV vs SW equation for (a) all five sites and (b) only sites 1, 2, 4 and 5, excluding site 3 because it deviates significantly from the other sites.

Table 4. The resultant formulae obtained from the PPV vs SW calculations all five sites.

Site	**Equation**	**R^2**
1	PPV=0.1776SW+0.0032	0.36
2	PPV=0.1773SW+0.0080	0.36
3	PPV=1.775SW+0.0026	0.16
4	PPV=0.196SW-0.0041	0.85
5	PPV=0.013SW+0.0003	0.72

4.1.2 Peak displacement measurements

The graphs of log peak displacement versus log SD for each of the prediction equations at each of the sites are found in Figures 23 – 27 with the 95% mean prediction interval. The peak displacement was not always easy to determine, due to the weak ground motion signals recorded for the explosions. The analysis of peak displacement aims to test the conclusion of Ford *et al*. (2014) that the displacement measurements are more reliable than the velocity measurements. Figures 28-30 display the results from each of the sites on one graph per prediction equation. Table 3 summarises the results of the regression analyses, and coefficient of determination (R^2) value for each of the sites and equations.

It is quite evident from the Table 3 and Figures 23-27 that there is a large scatter of peak displacement measurements when plotted with the scaled distances of the prediction equations. All sites have very low (even negative) R^2 values except sites 3 and 5 for the USBM and Ambraseys-Hendon equations, and the Langefors equation for site 5. In Figures 28-30, all the sites seem to show different results and no similarities, except perhaps sites 1 and 3 for the USBM equation; sites 3 and 4 for the Ambraseys equation; and sites 2 and 4 for the Langefors equation. Interestingly, the geology of site 5 is similar to the geology reported by Ford *et al.* (2014) during their experiment.

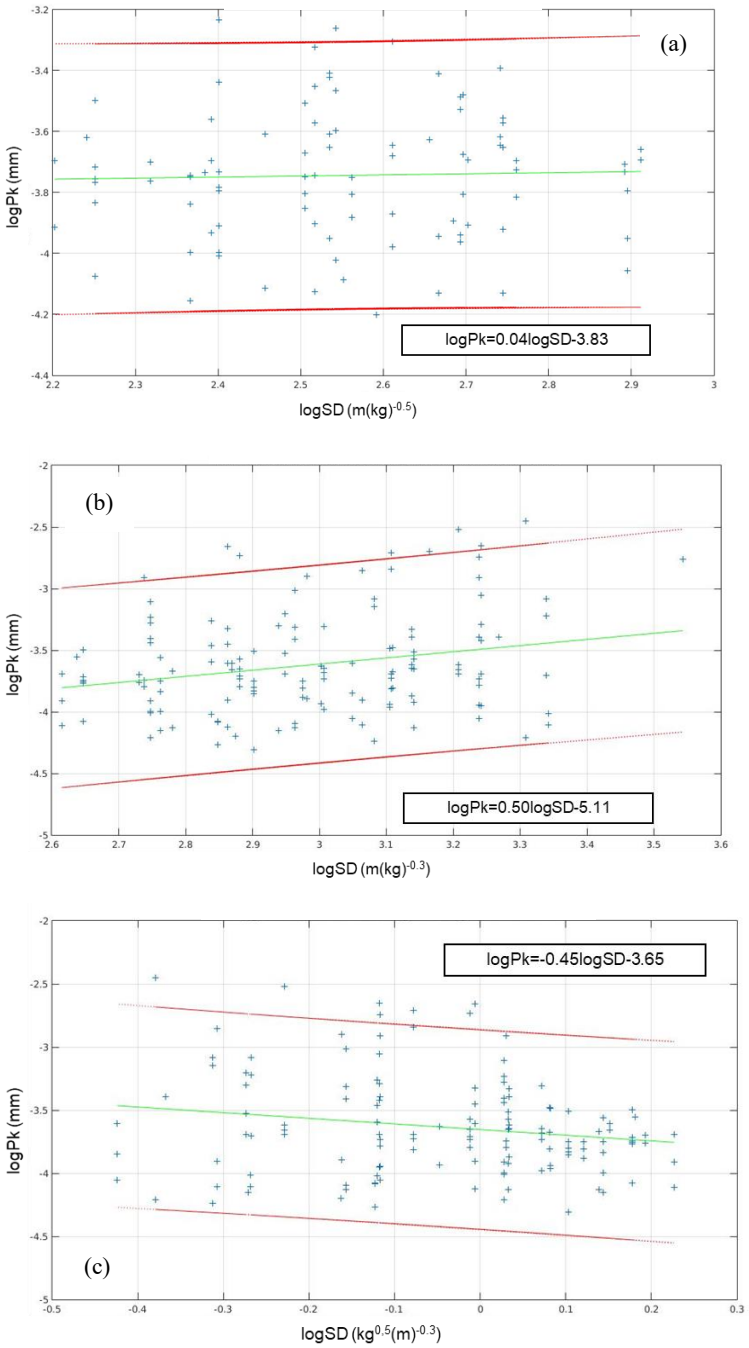


Figure 23. The relation between Peak displacement and SD for site 1.

(a) = USBM, (b) = Ambraseys, (c) = Langefors. The green lines represent the best fit using the least squared method and the red lines represent the 95% confidence range. The "+" symbol represents the recorded Peak displacement.

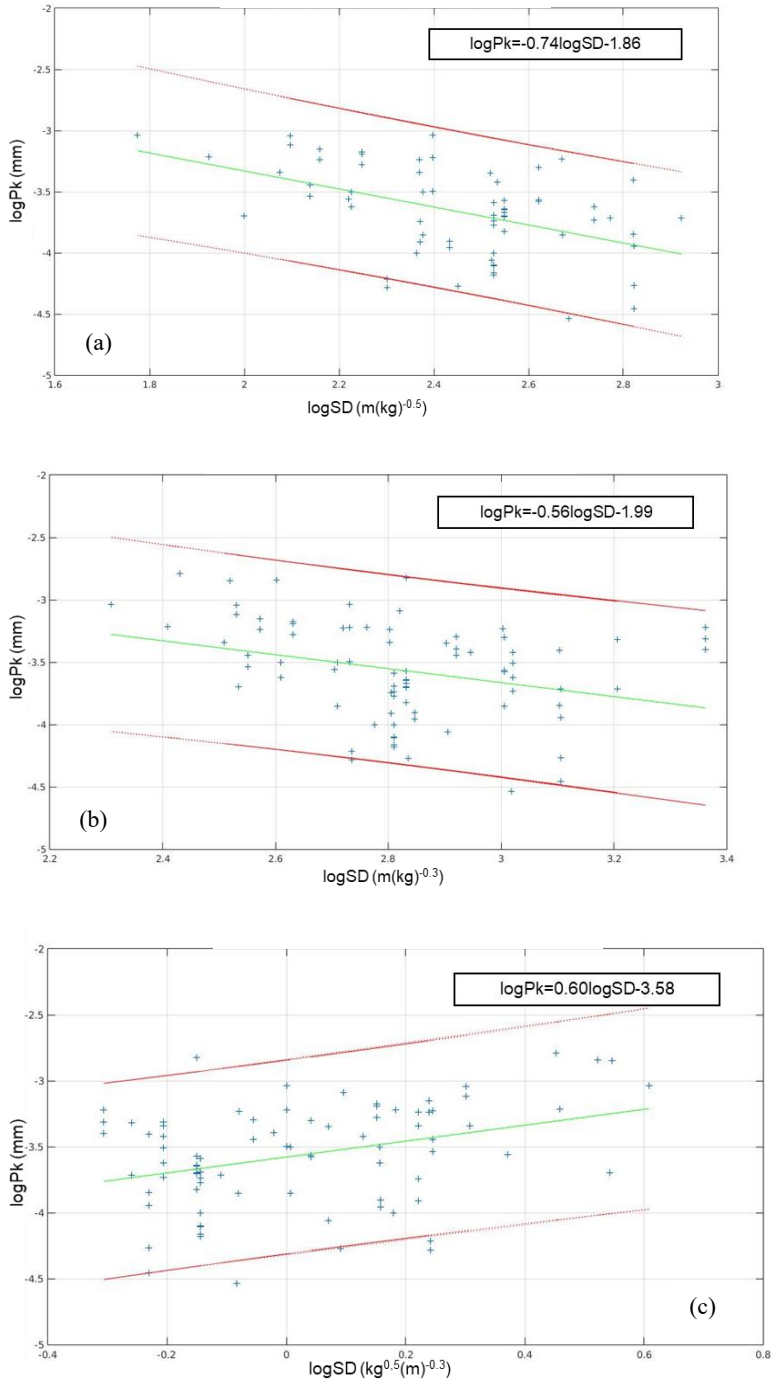


Figure 24. The relation between Peak displacement and SD for site 2.

(a) = USBM, (b) = Ambraseys, (c) = Langefors. The green lines represent the best fit using the least squared method and the red lines represent the 95% confidence range. The "+" symbol represents the recorded Peak displacement.

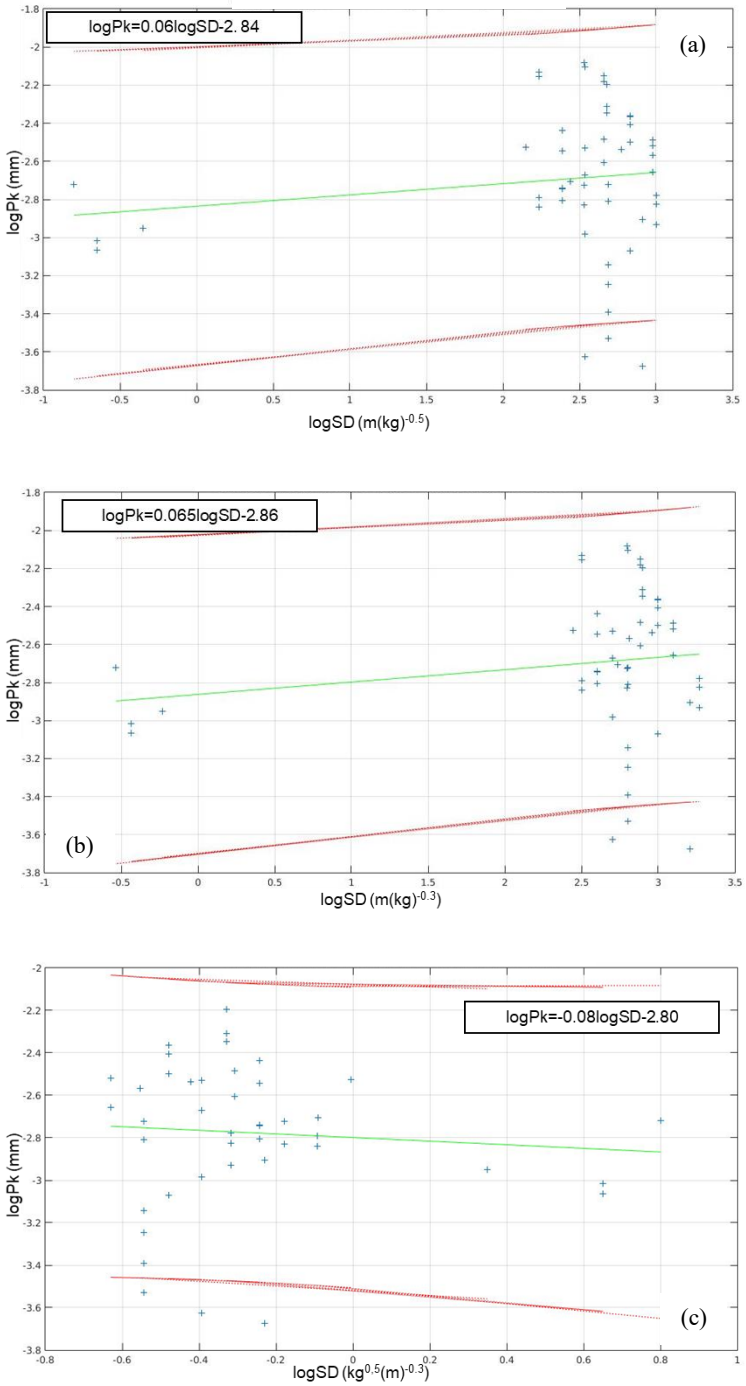


Figure 25. The relation between Peak displacement and SD for site 3.

(a) = USBM, (b) = Ambraseys, (c) = Langefors. The green lines represent the best fit using the least squared method and the red lines represent the 95% confidence range. The "+" symbol represents the recorded Peak displacement.

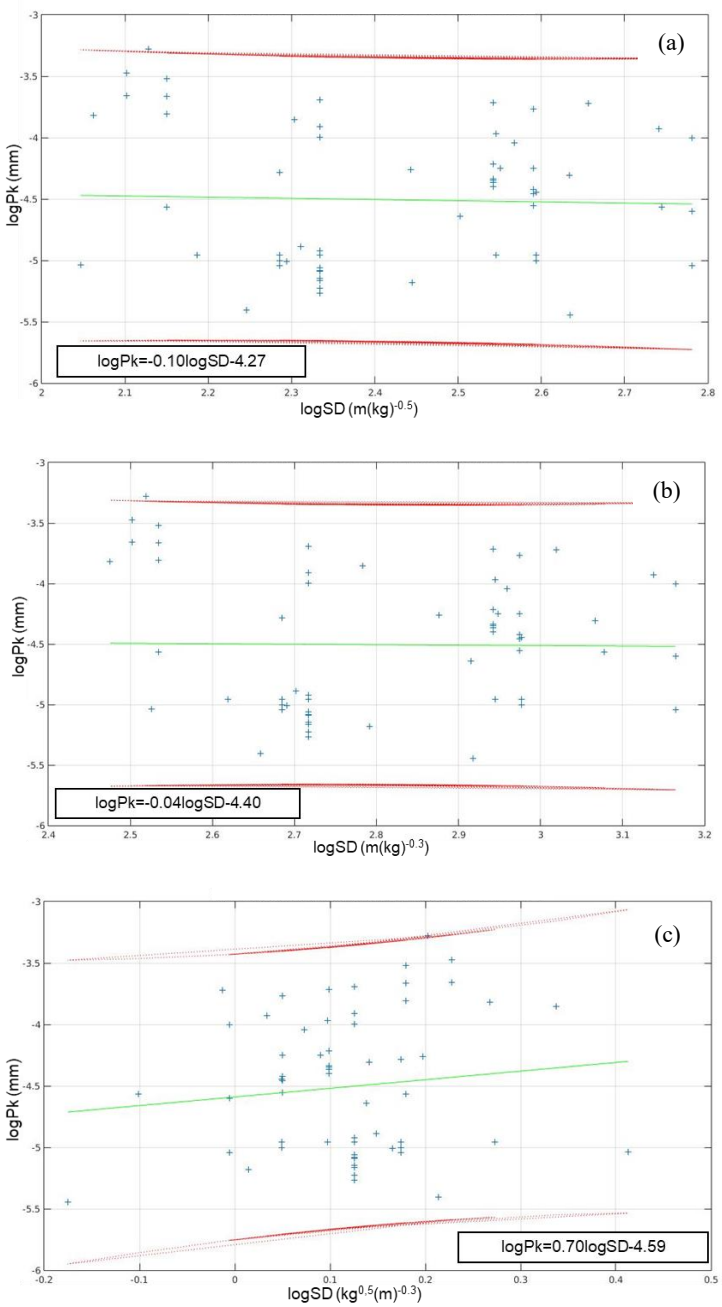


Figure 26. The relation between Peak displacement and SD for site 4.

(a) = USBM, (b) = Ambraseys, (c) = Langefors. The green lines represent the best fit using the least squared method and the red lines represent the 95% confidence range. The "+" symbol represents the recorded Peak displacement.

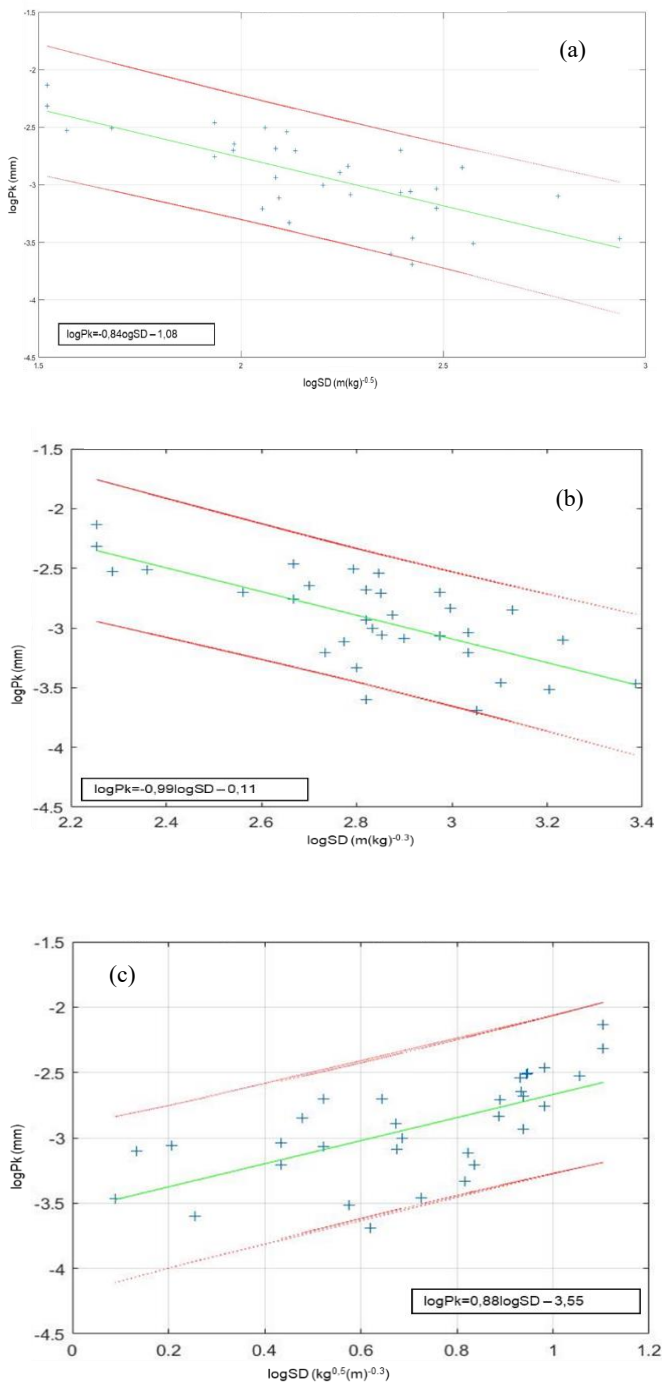


Figure 27. The relation between Peak displacement and SD for site 5.

(a) = USBM, (b) = Ambraseys, (c) = Langefors. The green lines represent the best fit using the least squared method and the red lines represent the 95% confidence range. The "+" symbol represents the recorded Peak displacement.

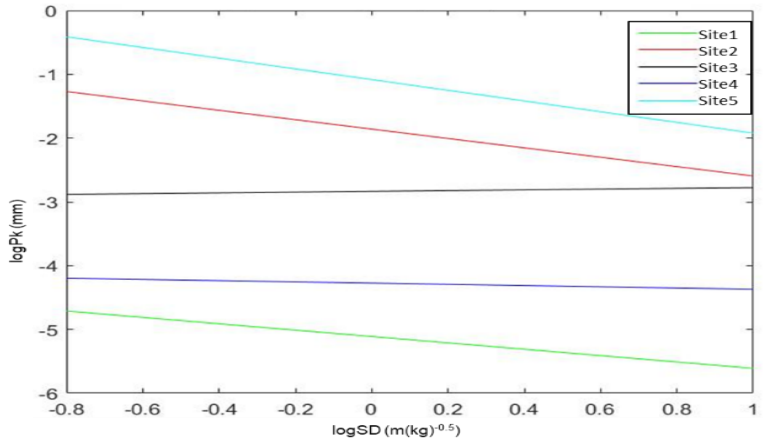


Figure 28. The results for the USBM (peak displacement) equation for all five sites. The coefficients calculated for each site are listed in Table 3

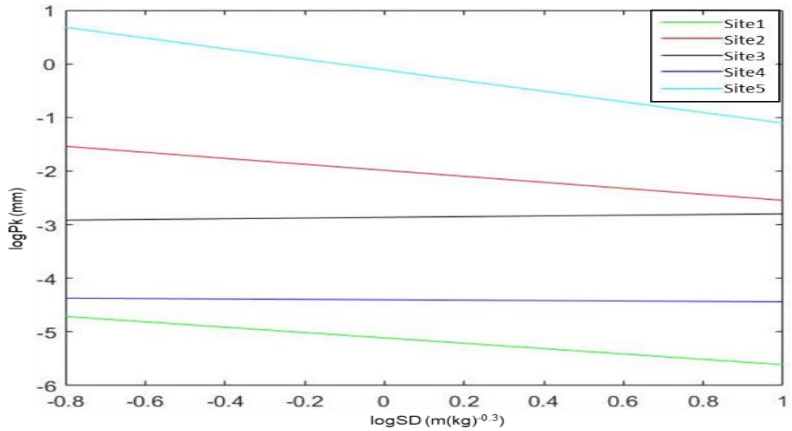


Figure 29. The results for the Ambraseys (peak displacement) equation for all five sites. The coefficients calculated for each site are listed in Table 3

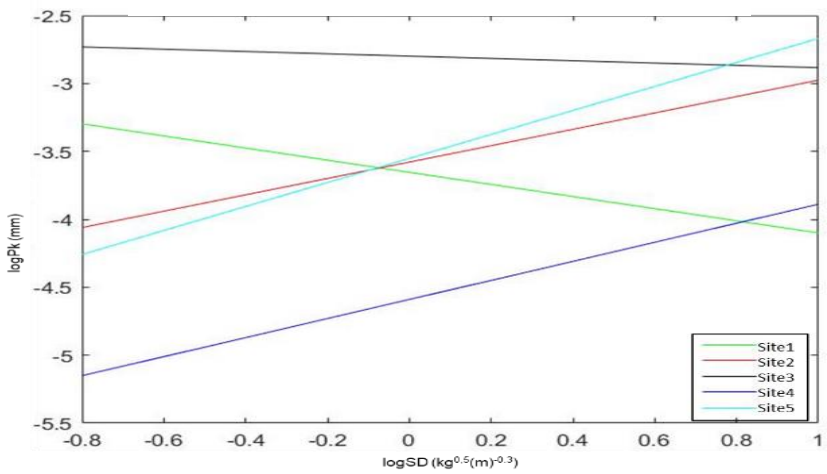


Figure 30. The results for the Langefors (peak displacement) equation for all five sites. The coefficients calculated for each site are listed in Table 3

4.1.3 First arrival displacement

All of the graphs of log first arrival displacement (Fst) versus log SD for each of the prediction equations at each of the sites are found in Figures 31 – 35 and they also display the 95% mean prediction interval. The first arrival displacement was not always easy to determine, due to the weak ground motion signals recorded for the explosions and thus some of the data used in other analyses (such as peak displacement) could not be utilised for this analysis. The analysis of first arrival displacement follows the method of Bonner *et al.* (2013) and Koper *et al.* (2002) where they utilized the peak displacement of the P-wave arrival for prediction equations. Figures 36-38 display the results from each of the sites on one graph per prediction equation. Table 3 summarises the results of the regression analyses, and coefficient of determination (R^2) value for each of the sites and equations.

These results are similar to the ones obtained for the peak displacement with site 3 and site 5 having the highest R^2 values while the other sites have very low (even negative) R^2 values. From Figures 36 and 37, sites 3 and 5 exhibit a similar gradient for the USBM and Ambraseys equations. In addition, site 5 is situated on geology similar to that at the sites reported within Bonner *et al.* (2013) and Koper *et al.* (2002).

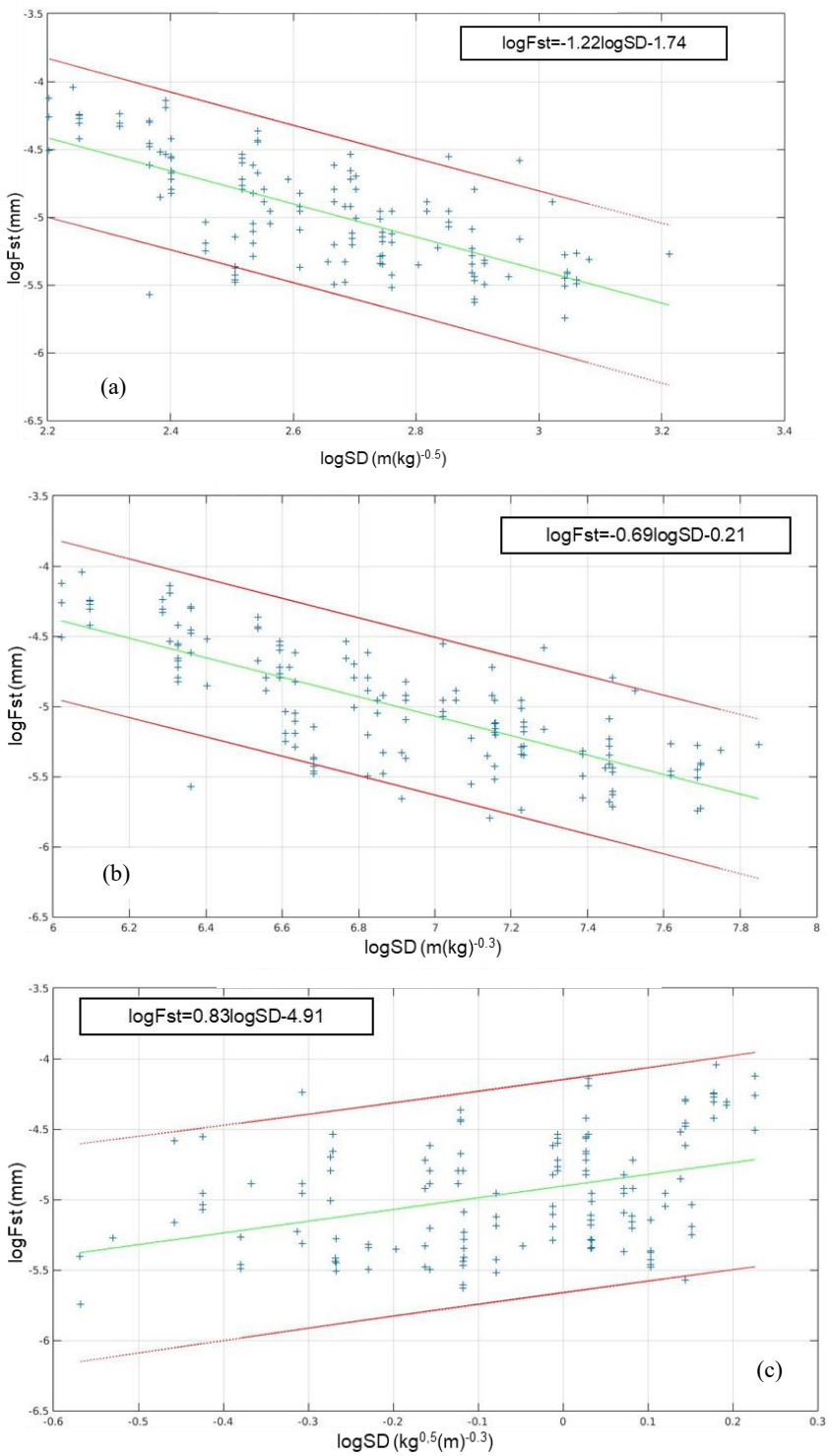


Figure 31. The relation between the first arrival displacement and SD for site 1.

The green lines represent the best fit using the least squared method and the red lines represent the 95% confidence range. The "+" symbol represents the recorded first arrival displacement. (a) = USBM, (b) = Ambraseys, (c) = Langefors.

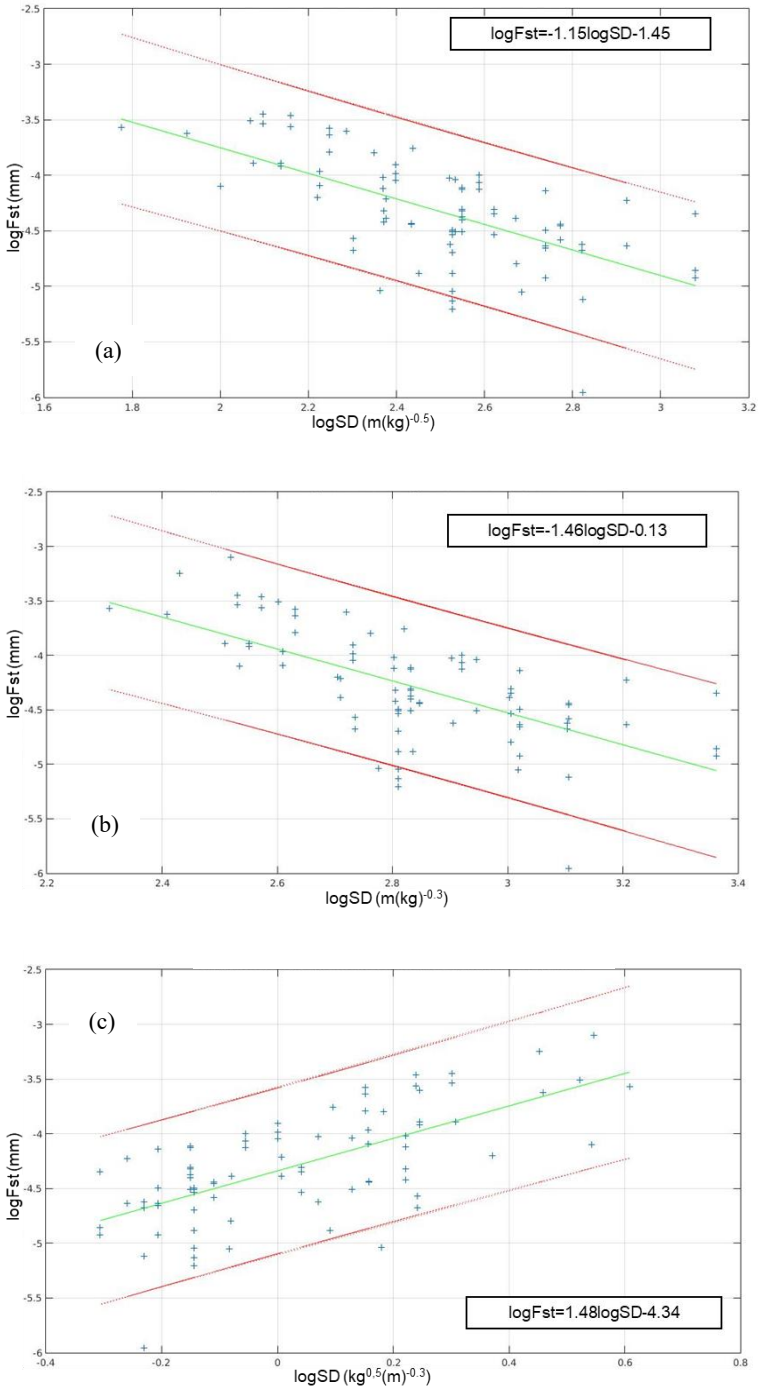


Figure 32. The relation between the first arrival displacement and SD for site 2.

The green lines represent the best fit using the least squared method and the red lines represent the 95% confidence range. The "+" symbol represents the recorded first arrival displacement. (a) = USBM, (b) = Ambraseys, (c) = Langefors.

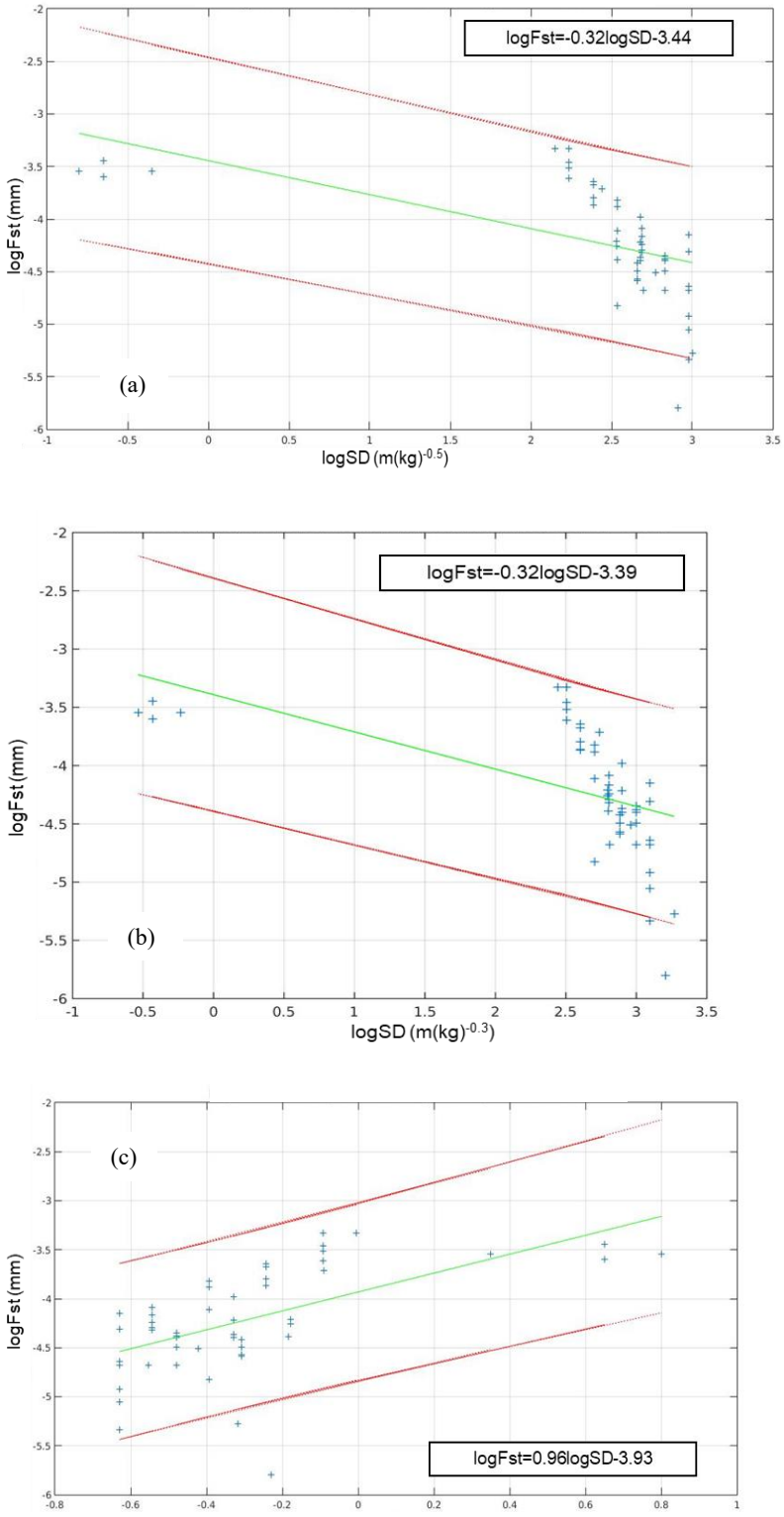


Figure 33. The relation between the first arrival displacement and SD for site 3.

The green lines represent the best fit using the least squared method and the red lines represent the 95% confidence range. The "+" symbol represents the recorded first arrival displacement. (a) = USBM, (b) = Ambraseys, (c) = Langefors.

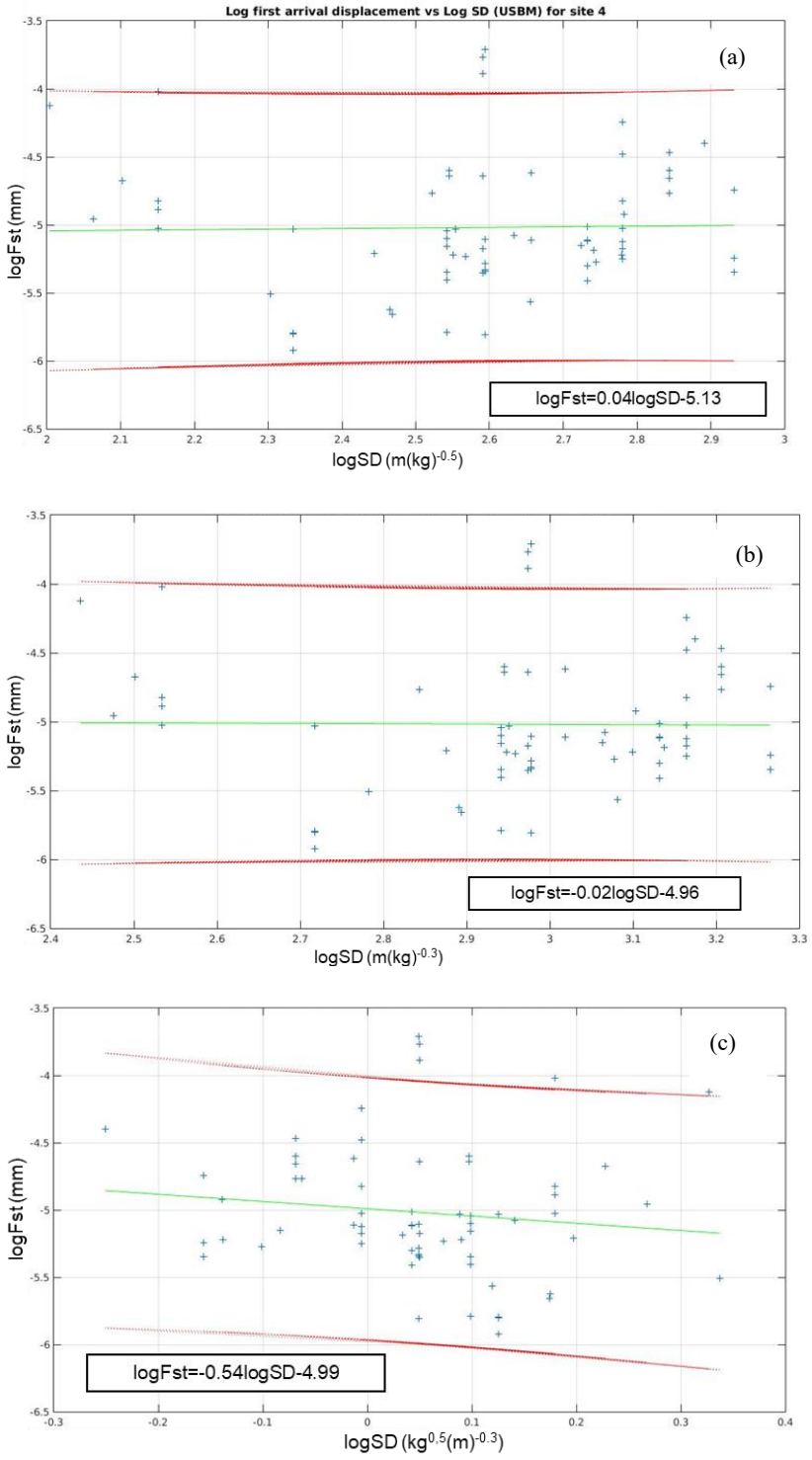


Figure 34. The relation between the first arrival displacement and SD for site 4.

The green lines represent the best fit using the least squared method and the red lines represent the 95% confidence range. The "+" symbol represents the recorded first arrival displacement. (a) = USBM, (b) = Ambraseys, (c) = Langefors.

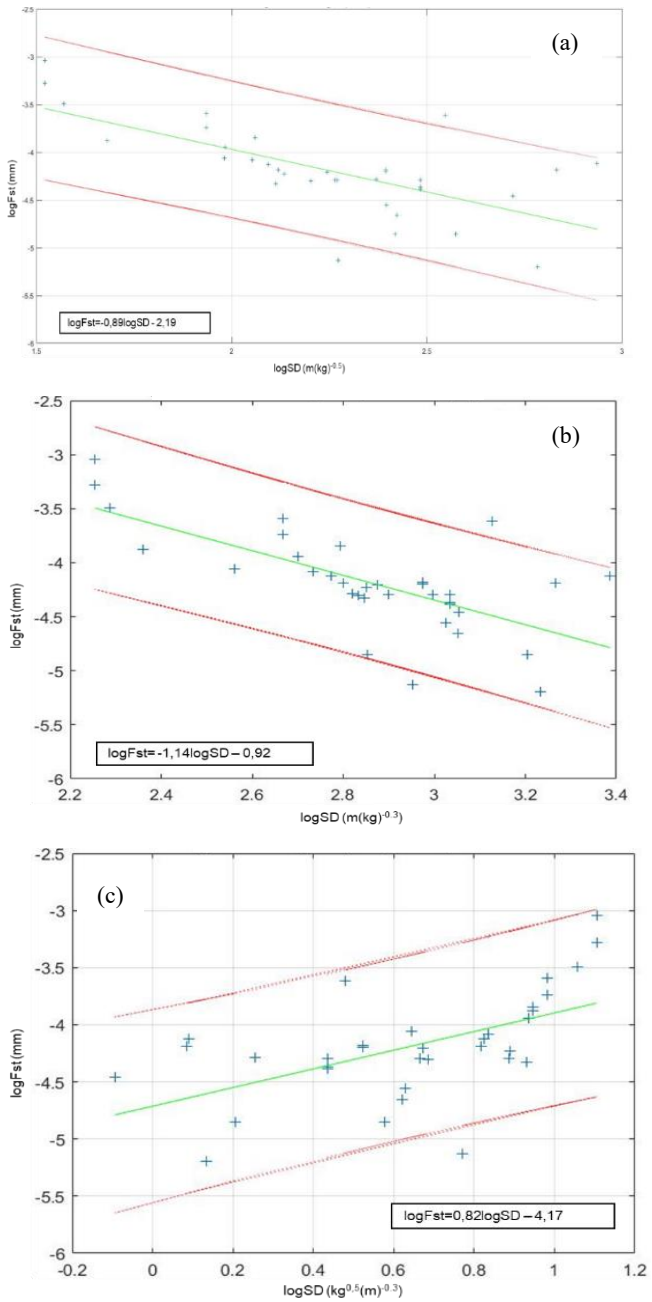


Figure 35. The relation between the first arrival displacement and SD for site 5.

The green lines represent the best fit using the least squared method and the red lines represent the 95% confidence range. The "+" symbol represents the recorded first arrival displacement. (a) = USBM, (b) = Ambraseys, (c) = Langefors.

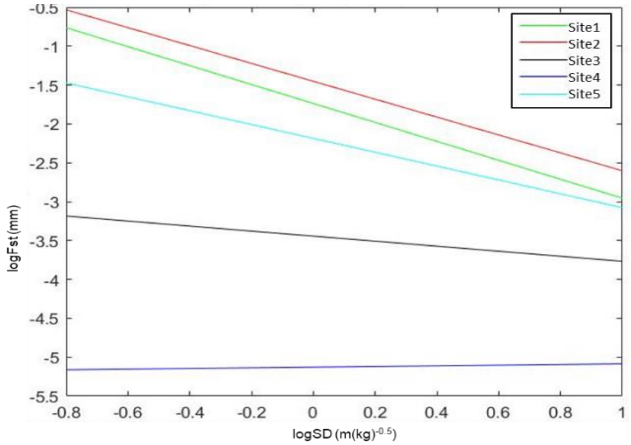


Figure 36. The results from the USBM (first arrival displacement) for all five sites. . The coefficients calculated for each site are listed in Table 3

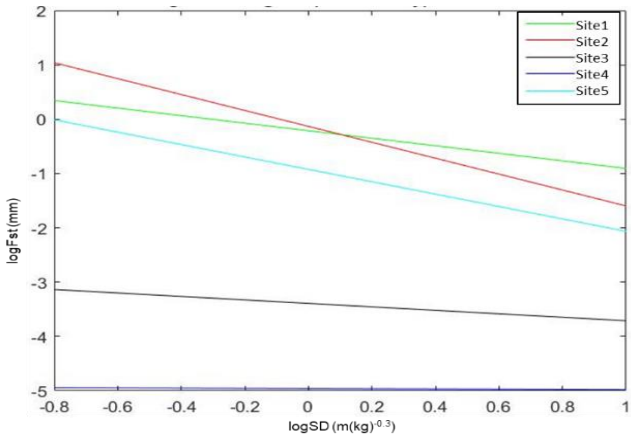


Figure 37. The results from the Ambraseys (first arrival displacement) for all five sites. The coefficients calculated for each site are listed in Table 3

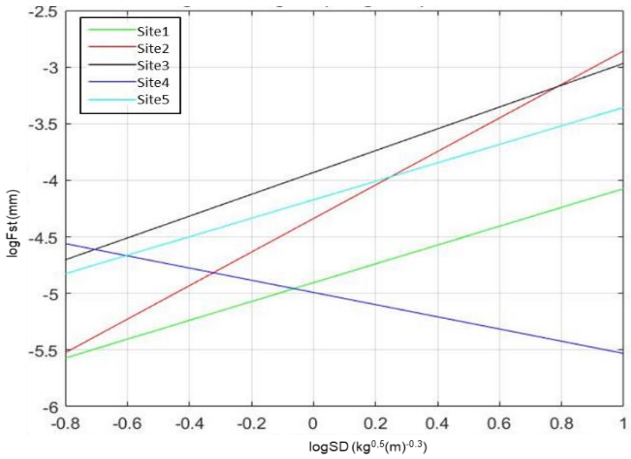


Figure 38. The results from the Langefors (first arrival displacement) for all five sites. The coefficients calculated for each site are listed in Table 3

4.2 Atmospheric shock wave monitoring

4.2.1 Displacement of atmospheric shock wave

The values for the atmospheric shock waves were easier to measure than those of the ground motion because the atmospheric shock waves are more prominent on the seismograms than those of the ground motion, as is evident in Figure 10. Johnston (1987) encountered a similar situation and noted that analysing the atmospheric shock waves was useful when the P and S waves are not clearly recorded.

All of the graphs of the log displacement of the atmospheric shock wave versus log SD for each of the prediction equations at each of the sites are shown in figures 39 – 43 and they also display the 95% mean prediction interval. Figures 44-46 display the results from each of the sites on one graph per prediction equation. Table 5 summarises the results of the regression analyses, and coefficient of determination (R^2) value for each of the sites and equations.

There are distinct differences in the R^2 values between the various equations and sites, with the highest R^2 values for sites 3, 4 and 5 (greater than the generally accepted value of 0.7 (Kahriman, 2002)), especially for the USBM equation which displays the best R^2 values for all the sites. This is most surprising because what was generally reported in literature (e.g. Williams and Newell (1991); Joint Committee on Administrative Rules (1998); Quest Consultants (1999)) is that atmospheric shock waves/overpressure is inversely proportional to the cube root of the distance from the blast, which is equivalent to the Ambraseys-Hendron equation. The results for site 2 in Figures 44 and 45 are distinctly different to those of the other sites, and sites 1, 3 and 5 are similar for the USBM equation.

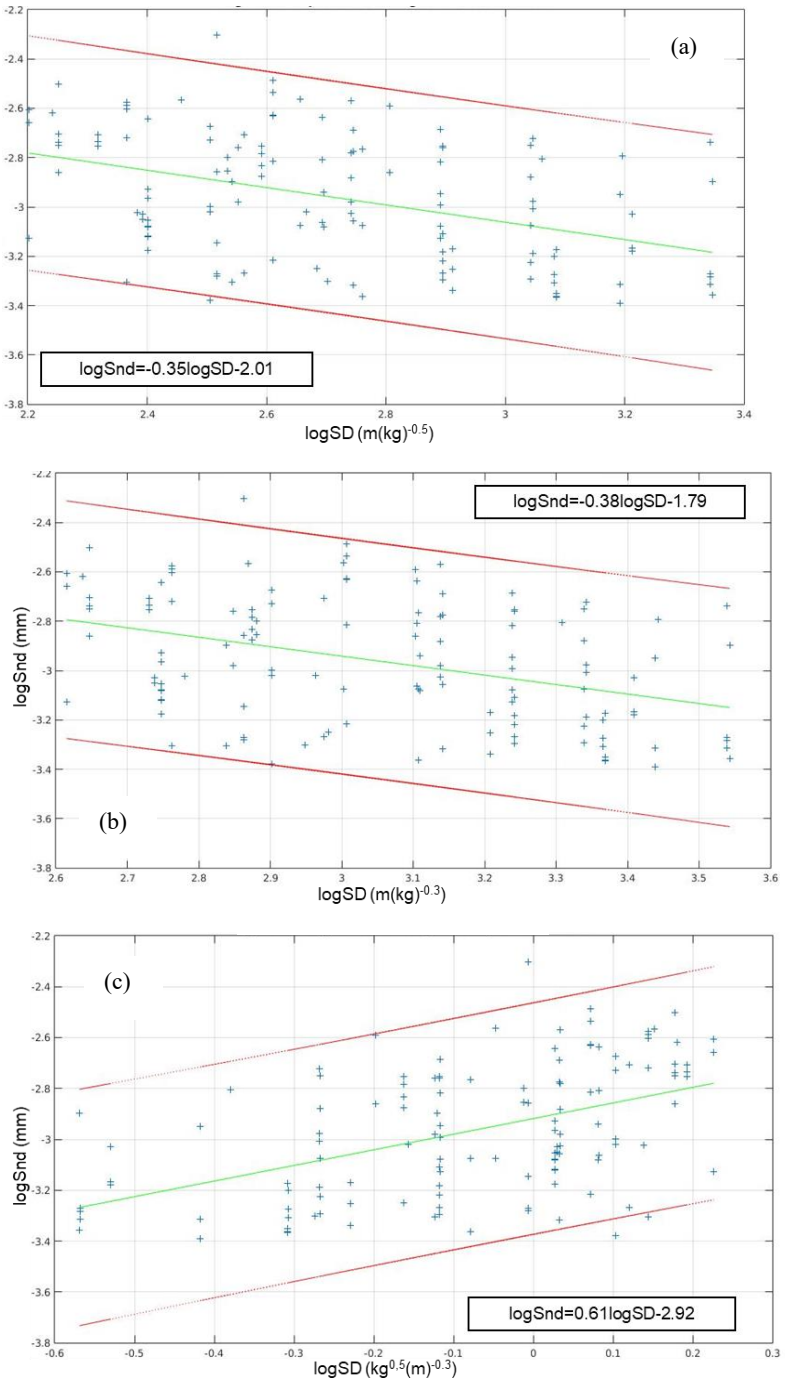


Figure 39. The relation between the displacement caused by the atmospheric shock wave and SD for site 1.

The green lines represent the best fit using the least squared method and the red lines represent the 95% confidence range. The "+" symbol represents the recorded atmospheric shock displacement. (a) = USBM, (b) = Ambraseys, (c) = Langefors.

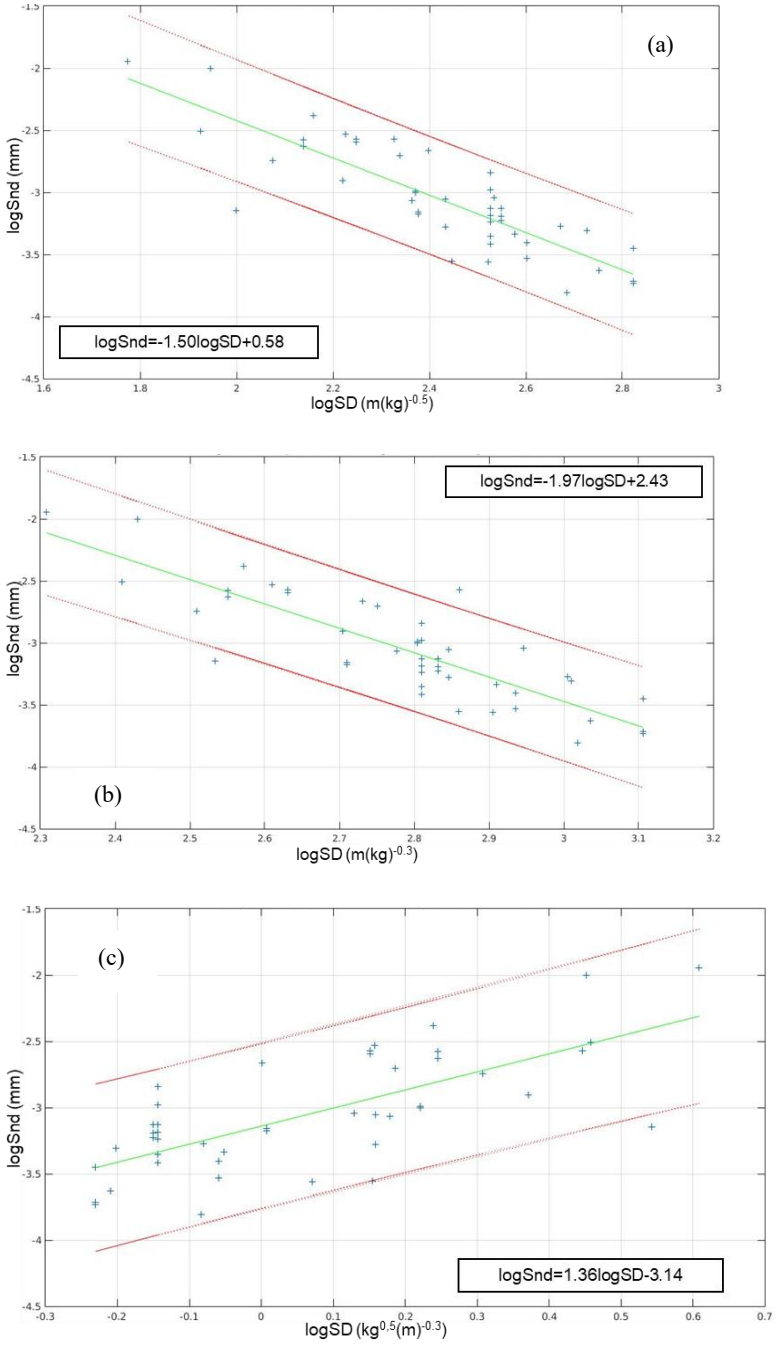


Figure 40. The relation between the displacement caused by the atmospheric shock wave and SD for site 2.

The green lines represent the best fit using the least squared method and the red lines represent the 95% confidence range. The "+" symbol represents the recorded atmospheric shock displacement. (a) = USBM, (b) = Ambraseys, (c) = Langefors.

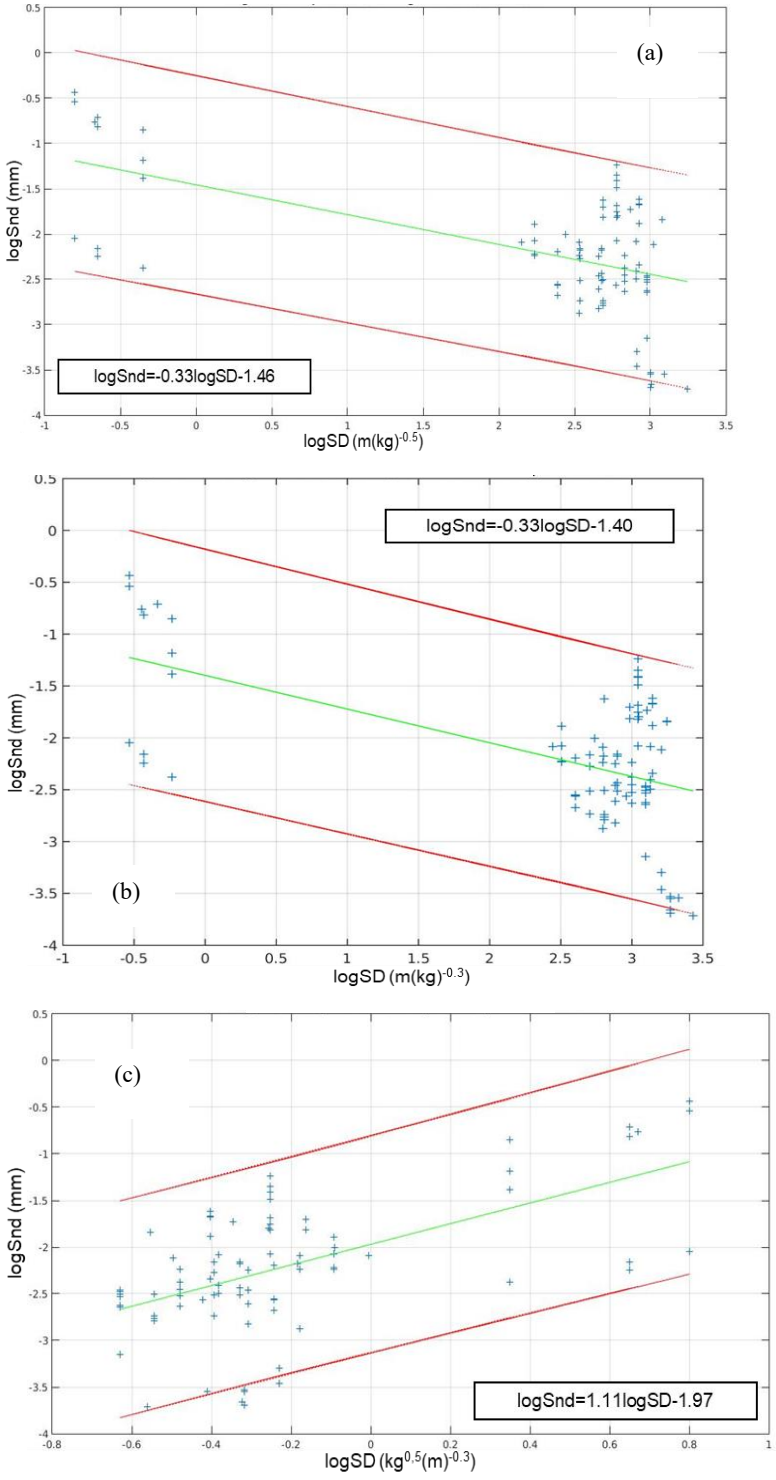


Figure 41. The relation between the displacement caused by the atmospheric shock wave and SD for site 3.

The green lines represent the best fit using the least squared method and the red lines represent the 95% confidence range. The "+" symbol represents the recorded atmospheric shock displacement. (a) = USBM, (b) = Ambraseys, (c) = Langefors.The gap in the data is due to the lack of stations within that range from the explosion.

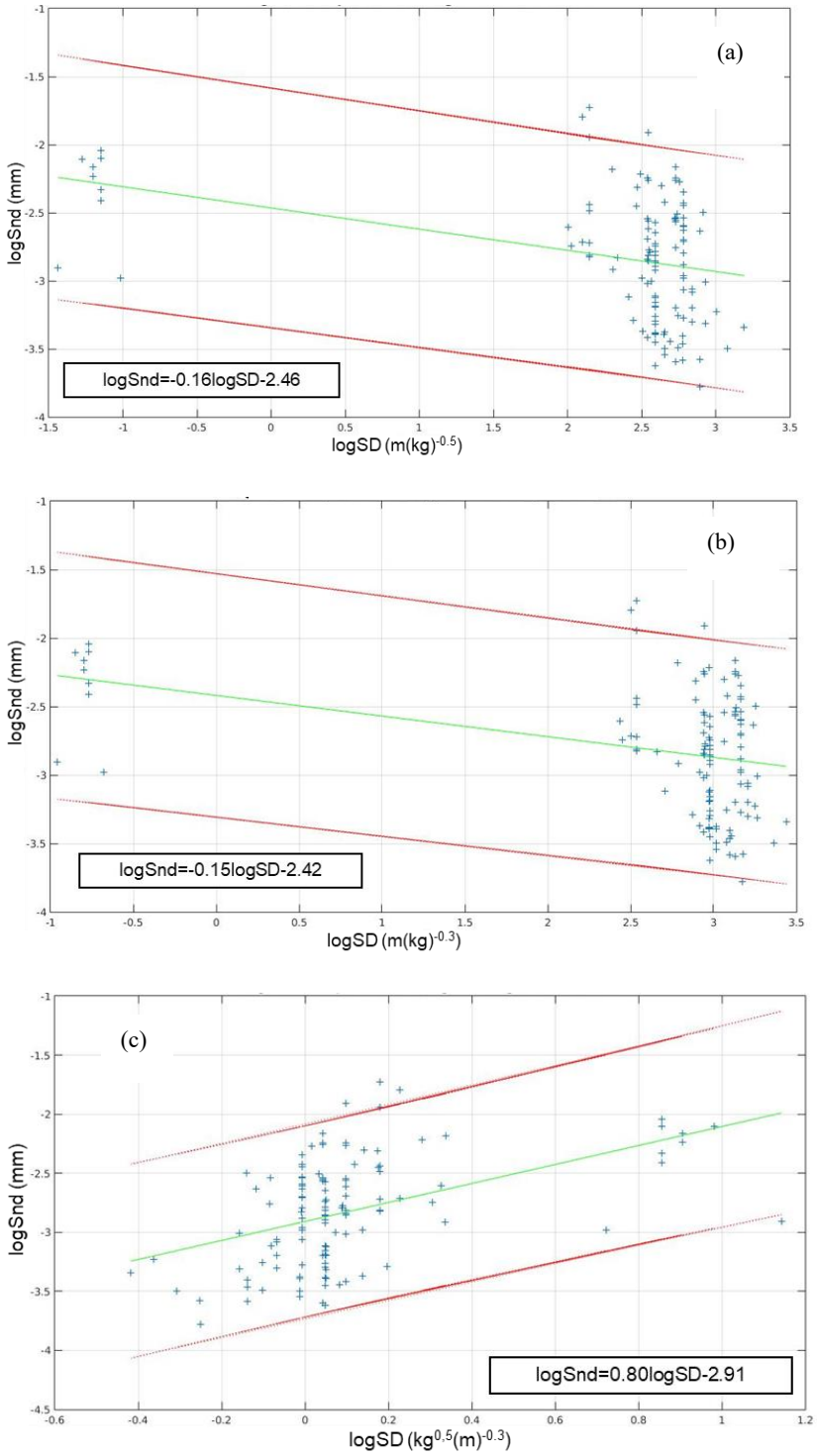


Figure 42. The relation between the displacement caused by the atmospheric shock wave and SD for site 4.

The green lines represent the best fit using the least squared method and the red lines represent the 95% confidence range. The "+" symbol represents the recorded atmospheric shock displacement. (a) = USBM, (b) = Ambraseys, (c) = Langefors. The gap in the data is due to the lack of stations within that range from the explosion.

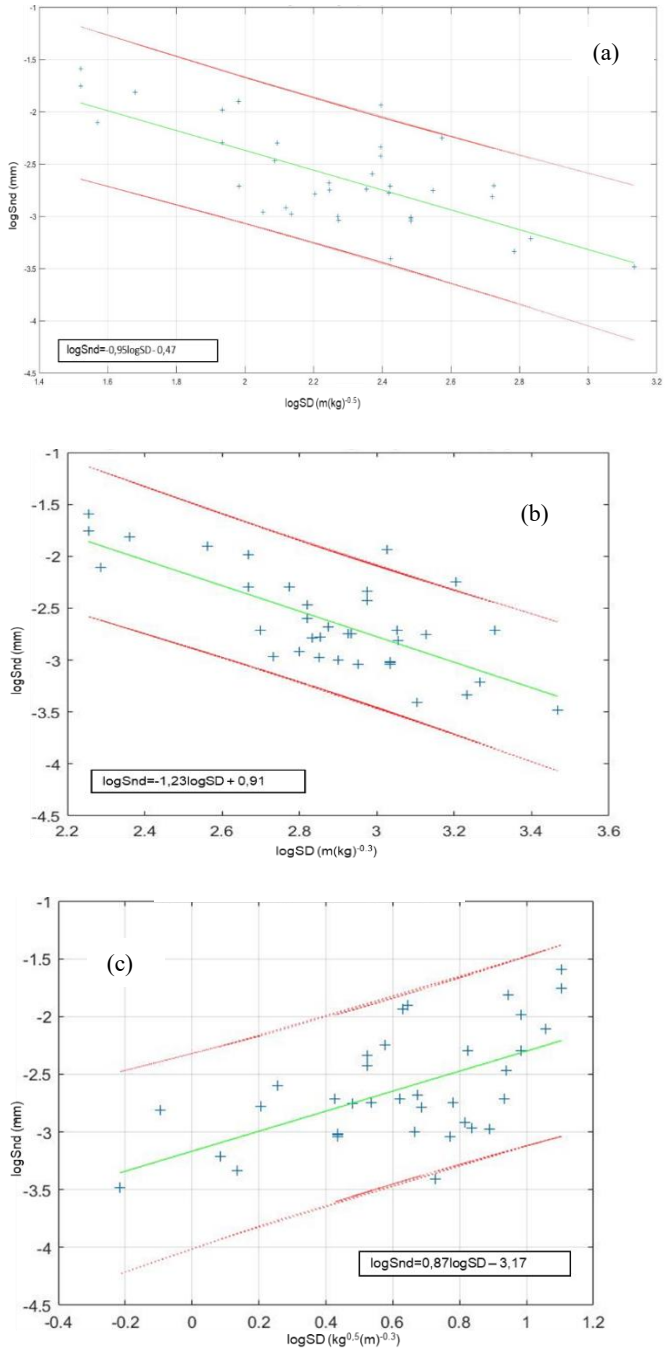


Figure 43. The relation between the displacement caused by the atmospheric shock wave and SD for site 5.

The green lines represent the best fit using the least squared method and the red lines represent the 95% confidence range. The "+" symbol represents the recorded atmospheric shock displacement. (a) = USBM, (b) = Ambraseys, (c) = Langefors.

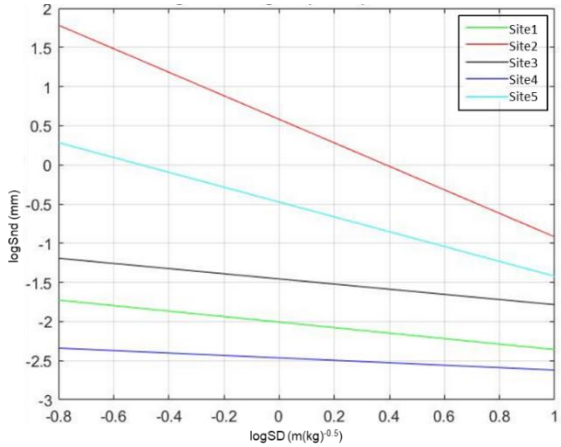


Figure 44. The results for the USBM (atmospheric shock displacement) relation for all five sites. The coefficients calculated for each site are listed in Table 5

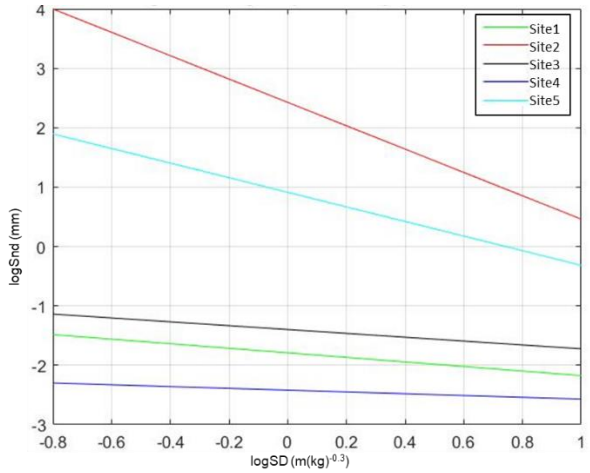


Figure 45. The results for the Ambraseys (atmospheric shock displacement) relation for all five sites. The coefficients calculated for each site are listed in Table 5

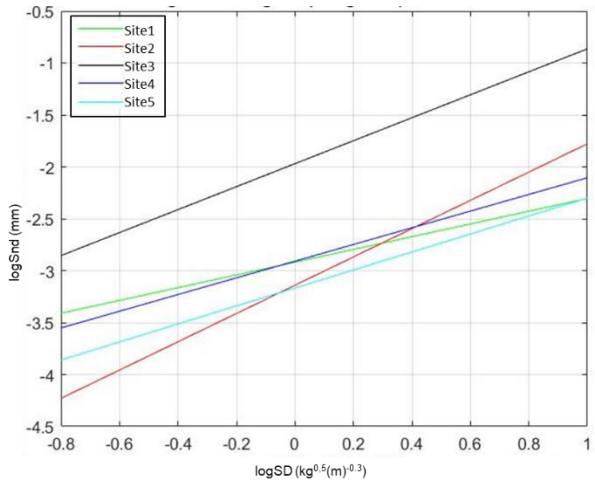


Figure 46. The Langefors (atmospheric shock displacement) relation for all five sites. The coefficients calculated for each site are listed in Table 5

Table 5. Empirical formulae for the ground displacement caused by the atmospheric shock wave (Snd) obtained from the five different sites.

	Site 1		***Site 2***	***Site 3***	***Site 4***	***Site 5***
Geology (see Table 2 for details)	Tierberg Formation of the Ecca Group.		Ventersdorp Supergroup; Prince Albert Formation of the Karoo Supergroup; Quaternary sand	Letaba and Clarens formations of the Karoo Supergroup	Hout River Gneiss. Letaba and Clarens formations of the Karoo Supergroup	Karoo Supergroup; Aeolian sand of the Gordonia Formation of the Kalahari Group
USBM $Snd = K(SD)^{-\beta}$	K	0.01	3.83	0.04	0.003	0.34
	β	0.35	1.50	0.33	0.16	0.95
R^2	0.42		0.11	0.75	0.83	0.06
Ambraseys-Hendron $Snd=K(SD_A)^{-\beta}$	K	0.02	266.99	0.04	0.004	8.18
	β	0.38	1.97	0.33	0.15	1.23
R^2	0.18		-0.51	0.75	0.82	0.12
Langefors-Kihlstrom $Snd=K(SD_L)^{\beta}$	K	0.001	$7.24e^{-04}$	0.01	0.001	$6.81e^{-0.4}$
	β	0.61	1.36	1.11	0.80	0.87
R^2	-0.23		-0.75	-1.51	-1.42	-0.91

4.2.2 Secondary shock delay

All of the graphs of the log displacement of the scaled secondary shock delay (Dt) versus the natural log SD (as described in Bonner *et al.,* 2013; Gitterman and Hofstetter, 2012 and Gitterman, 2013) for each of the sites are found in Figure 47 and they also display the 95% mean prediction interval. Figure 48 displays the results for all of the sites in one graph. Table 6 summarises the results of the regression analyses, and coefficient of determination (R^2) value for each of the sites.

From Table 6, it is interesting to note that the R^2 values are equal to one, especially since there is such a wide scatter of the values. However, Gitterman (2013) also reported similar values of R^2 and a gradient which falls between those of site 1 and site 5 in the above equations. This is reassuring, since site 5 is also a semi-desert environment comparable to the site described in Bonner *et al*. (2013), Gitterman and Hofstetter (2012) and Gitterman (2013) as “the subsurface layer of 0.5 – 1.0

m consists of soft and loose sediments, with consolidated sediments below. The subsurface media is made up of Quaternary alluvial conglomerates, underlain by consolidated limestone, chalk and chert rocks."

In Figure 48, it is clear that sites 2, 3 and 4 display similar gradients which may be indicative of a different VOD within the assortment of explosives used compared to sites 1 and 5. This is similar to the results obtained by Gitterman (2013) as displayed in Figure 7. Alternatively, it could be related to the differing topographies of the sites.

Table 6. Empirical formulae for the scaled SS wave delay (Dt) obtained from the five different sites.

Site	**Equation**	**R^2**	**Season**
1	Dt=0.0081928lnSD-0.032479	1.00	Autumn
2	Dt=0.0204lnSD-0.096245	0.9996	Spring
3	Dt=0.024688lnSD-0.11758	0.9998	Summer
4	Dt=0.024572lnSD-0.13233	0.9997	Spring
5	Dt=0.0020355lnSD-0.0027627	1.00	Summer

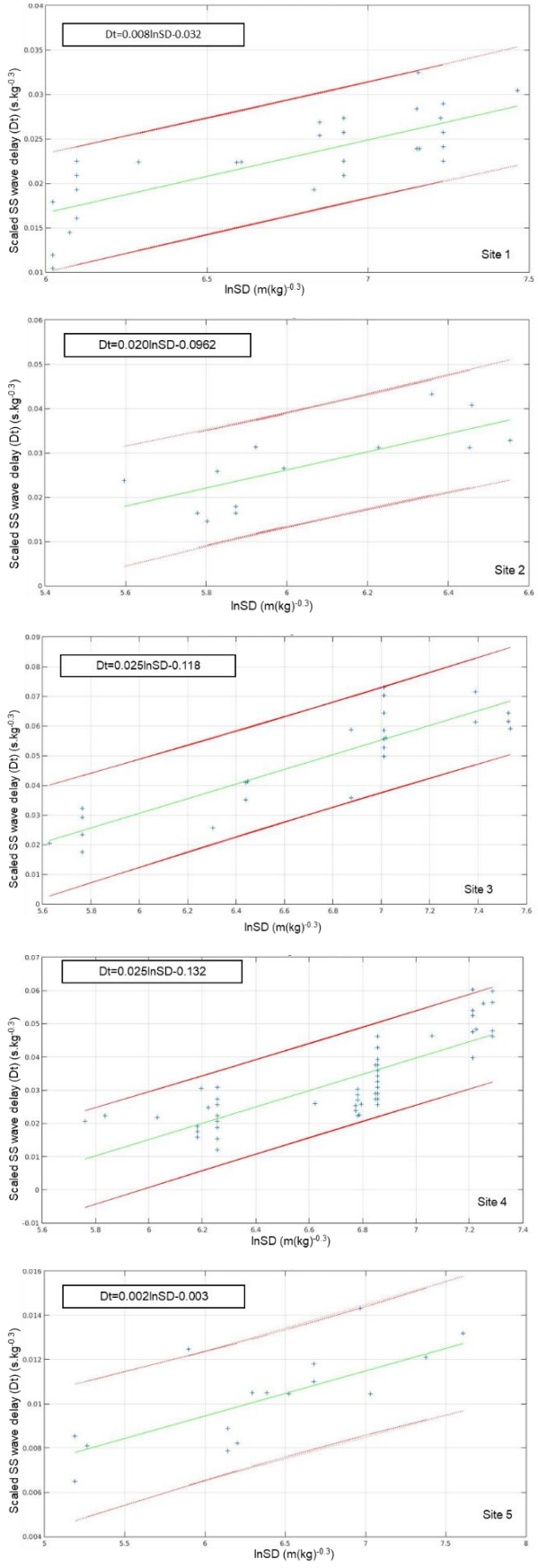


Figure 47. The relation between the scaled SS wave delay (Dt) and ln SD for all the sites.

The green lines represent the best fit using the least squares method and the red lines represent the 95% confidence range. The "+" symbol represents the recorded secondary shock wave delay.

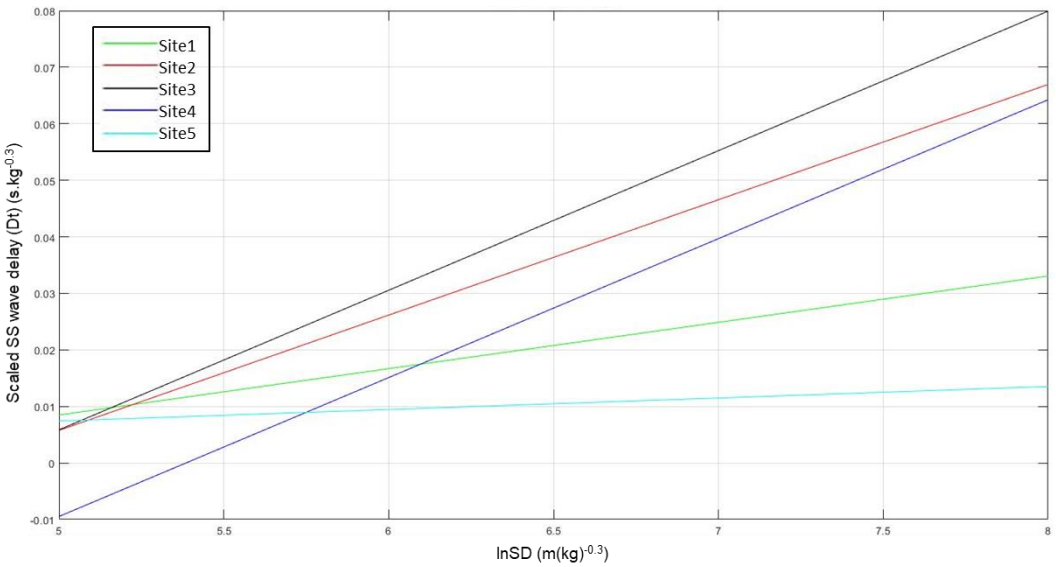


Figure 48. The relation between scaled SS wave delay (Dt) and ln SD for all five sites. The coefficients calculated for each site are listed in Table 6

All of the graphs of the log scaled SS delay (Dt) versus the log SD for each of the sites are shown in Figure 49 and they also display the 95% mean prediction interval. Figure 50 displays the results of all the sites on one graph. Table 7 summarises the results of the regression analyses, and coefficient of determination (R^2) value for each of the sites.

Table 7. Empirical formulae for the relationship between the scaled secondary shock (SS) wave delay (Dt) and scaled distance obtained from the five sites.

Site	**Equation**	**R^2**	**Season**
1	$Dt=0.0015SD^{0.401}$	0.8892	Autumn
2	$Dt=2.4424e^{-04}SD^{0.772}$	0.4213	Spring
3	$Dt=7.4456e^{-04}SD^{0.609}$	0.9026	Summer
4	$Dt=1.7993e^{-04}SD^{0.764}$	0.7256	Spring
5	$Dt=0.0026SD^{0.209}$	0.9675	Summer

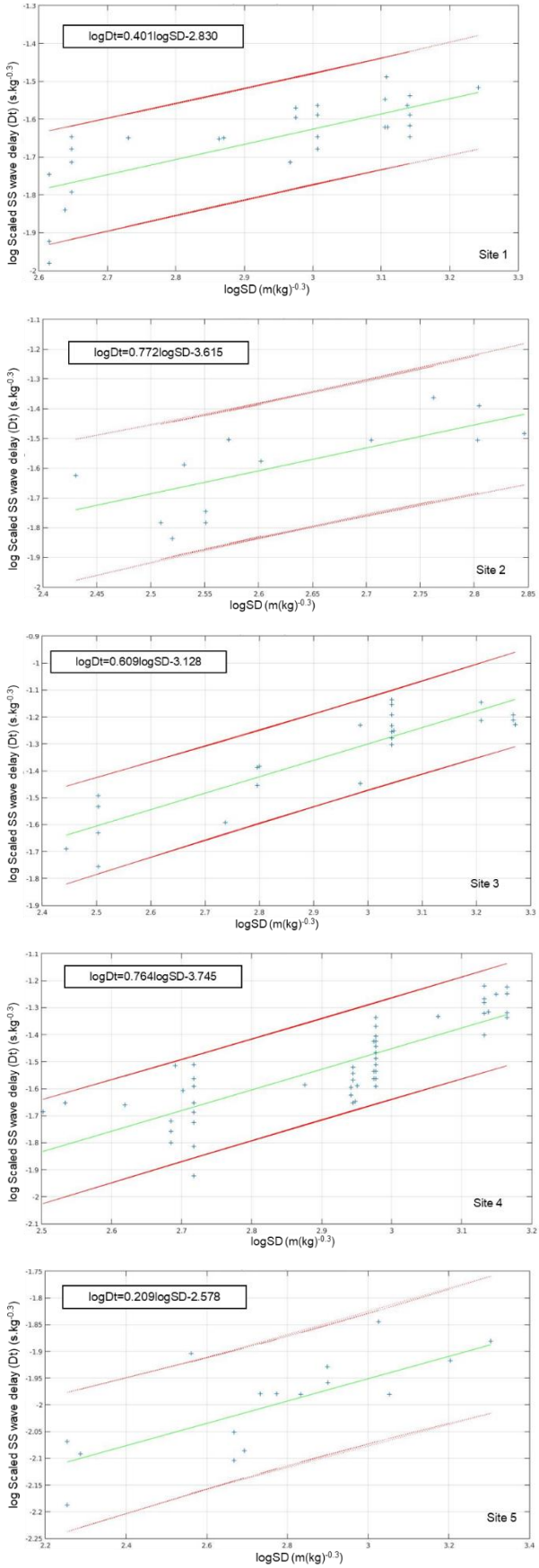


Figure 49. The relation between the log scaled SS wave delay (Dt) and log SD for all the sites

The green lines represent the best fit using the least squares method and the red lines represent the 95% confidence range. The "+" symbol represents the recorded log secondary shock wave delay

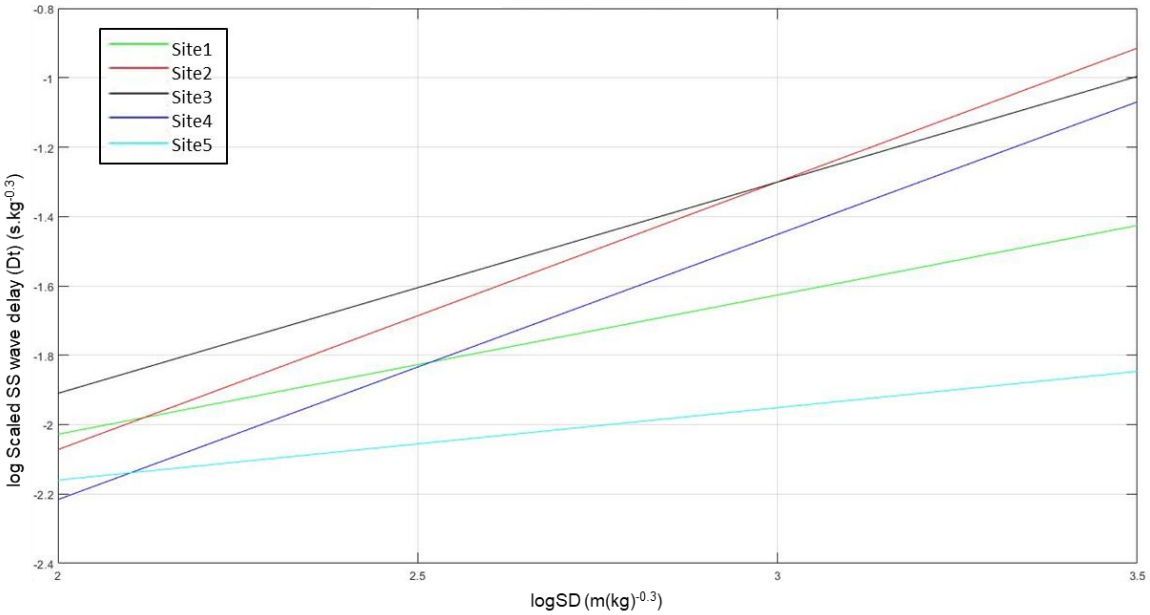


Figure 50. The relation between log scaled SS (Dt) and log SD for all five sites. The coefficients calculated for each site are listed in Table 7.

These results also display high R^2 values (greater than the generally accepted value of 0.7 (Kahriman, 2002)) except for site 2. Although there is still a scatter among the data, there are distinct groupings, which are obvious within the figures, providing more confidence within the results. As with Figure 48, in Figure 50 it is clear that sites 2 to 4 display similar gradients. However, unlike in Figure 48, sites 1 and 5 seem to differ in that respect.

5 Discussion

5.1 Ground monitoring

Although there is extensive literature describing prediction equations for the vibrations induced by blasting in open pit mines and tunneling (e.g. Aloui *et al. (*2016); Bongiovanni *et al.* (1991); Khandelwal and Singh (2007); Kahriman (2002); Ozer (2008); Ozer *et al. (*2008); Puri and Prakash (1991) and Kumar *et al*. (2016)) many authors conclude that a reliable general approach or formula has not been established yet due to the complexity of issues relating to blasting.

In fact, the low R^2 values obtained for the PPV predictive equations (Table 3) are comparable with Khandelwal and Singh (2007), who used the same three equations and obtained an R^2=0.2276 for the USBM equation, R^2=0.1836 for the Ambraseys-Hendron equation, and R^2=0.2218 for the Langefors-Kihlstrom equation. Thus, these low R^2 are not unique to this experiment. But unlike Khandelwal and Singh (2007), the explosions within this experiment were on the surface, and, as Evers *et al.* (2007) and Williams and Newell (1991) stated, very little of the energy goes into the ground.

The data within Figures 13 to 17 is very scattered, but the higher coefficients of determination (R^2) indicate that the formulae obtained using the USBM equation show better fit than for the other relations, and a good fit for site 4. This is contrary to Ozer *et al.* (2008) and Kahriman (2002), who obtained the highest R^2 value for the Ambraseys-Hendron equation, and thus recommended the use of that equation.

However, it must be kept in mind that although the R^2 values for the Ambraseys-Hendron and Langefors equations are not as high as for the USBM sites, it is not necessarily true that there is something wrong with the fit. R^2 measures how useful the independent variable is in predicting values of the dependent variable, not how appropriate the polynomial model is for the data. When analysing inherently unpredictable data, a small value of R^2 indicates that the independent variable does not predict the dependent variable precisely.

This is particularly true for measurements of explosions on the surface of the ground, as opposed to excavation/mining explosions, which are placed within the bedrock. Thus, a

lot of the energy from the explosions is lost to the atmosphere and therefore an increase in distance from the explosions results in smaller P and S waves than calculated by the predictor equations, such as site 5 where the sensors were placed at greater distances than the sensors at the other sites. Ichinose *et al.* (1998), Johnston (1987) and Evers *et al.* (2007) noted similar findings. In addition, site 4 is a good example of an area where the geology plays an important role, as noted by Johnston (1987) and Koper *et al.* (2002), who stated that even minimal changes in the anelastic structure can affect the predictor equations and Redmayne and Turbitt (1991) who noted that different soils can magnify or diminish values by a factor of 4.

Since the geological constants for regions 1, 2, 3 and 4 are similar for the USBM equation, it would seem that the USBM is the more reliable PPV predictive equation to use for each of these sites, especially because values of 1.2 are considered satisfactory (Atkinson (2004); Atkinson and Mereu (1992); Ford *et al.* (2014)). Redmayne and Turbitt (1991), using a simple attenuation relation, obtained a value of 2.18 which differs from the results obtained during this study. However, one must caution against using the predictive equations designed for mining and excavation, because during blasting on the surface most of the energy escapes into the atmosphere. Thus, other methods should be sought to enhance these predictive equations in order to predict the ground vibrations caused by blasting on the surface. This is confirmed with the results obtained from examining the peak and first arrival displacements as suggested by Ford *et al.* (2014), Bonner *et al.* (2013) and Koper *et al.* (2002).

Table 4 displays the results obtained when the equations were simplified and PPV was plotted against scaled weight (SW). Although not all the results were greatly improved compared to those obtained from the USBM, Ambraseys and Langefors equations, it is a far simpler method to predict PPV in a particular area. The fact that the results for sites 1, 2 and 4 were very similar would suggest that this method could be more widely used.

Table 3, which displays the results from the peak displacement and the first arrival displacement, show negative R^2 values. Since R^2 is the proportion of variance explained by the fit, this basically means that the fit is actually worse than just fitting a horizontal line (such as some of the data displayed in Figures 23-35). Thus, unlike Ford *et al.* (2014), Bonner *et al*. (2013) and Koper *et al.* (2002), these measurements do not produce good results, except for those sites with similar geology, i.e. sites 3 and 5 and

mainly for the USBM equations. These results support Kumar *et al.* (2016), who stated that PPV is not as sensitive to changes in geological conditions as acceleration and displacement.

Although the sites differ between the ground motion measured (PPV or displacement), the equation which seems to produce the best fit is the USBM equation, which is in agreement with Aloui *et al.* (2016).

5.2 Surface/air monitoring

This study only used seismographs installed on the surface and did not utilize the sensors mentioned within the studies performed by Koper *et al.* (2002), Bonner *et al.* (2013), Gitterman and Hofstetter (2012), Gitterman (2013) and Ford *et al.* (2014), i.e. high pressure sensors, accelerometers on the surface, buried seismometers, acoustic gauges and high speed cameras. Nevertheless, it provided an opportunity to replicate their studies.

The shape of the overpressure pulse recorded by the geophones is consistent with the results obtained by Edwards *et al.* (2007), who concluded that the dispersed wave train of smaller amplitude that follows the initial overpressure pulse is an air-coupled Raleigh wave. This is very clear in Figure 11 on the vertical component and it is this initial overpressure pulse that was used for the surface/air monitoring studies.

As Gitterman (2013) noted, the predictive equation using secondary shock wave delay may be less accurate than traditional procedures and equations based on high pressure measurements, but it is significantly less expensive and in the case of an accidental explosion, may be the only method available.

In addition, this study agreed with Gitterman (2013), Johnston (1987) and Evers *et al*. (2007) who stated that the atmospheric shock waves were clearly observed at all sites, especially when compared to the ground motion measurements. The seismograms showed clear and strong main shock peaks and smaller amplitude secondary peaks, with easily measured arrival times.

Tables 5 to 7, which cover the results from the displacement caused by the atmospheric

shock wave, scaled secondary shock wave delay and the log of the scaled secondary shock wave delay respectively, display more promising results than those in Tables 3 and 4 which cover the results from the PPV, peak displacement and first arrival displacement measured at the sites. The R^2 values in Tables 5 to 7 are greater than the generally accepted value of 0.7 (Kahriman, 2002)).

Once again, the highest R^2 values in Table 5, which show the results of the displacement caused by the atmospheric shock wave, are for the USBM predictive equation, although this time the measurement is for the atmospheric shock wave displacement. Thus, it would seem the most reliable predictive equation to use.

However, the results do improve dramatically when examining the secondary shock wave delay phenomenon as described by Gitterman and Hofstetter (2012) and Gitterman (2013). This unique phenomenon seems to provide a better solution than the USBM, Ambraseys-Hendron and Langefors equations for predictive equations of surface explosions. Although the R^2 values reported in Table 6, which covers the scaled secondary shock wave delay, equate to one, indicating that the model explains all the variability of the response data around its mean, they are similar to the Gitterman and Hofstetter (2012) and Gitterman (2013) studies and the gradients within the equations for sites 1 and 5 are also similar.

Sites 2 to 4 display similar gradients, which would seem to indicate a different assortment of explosives used with a different VOD to those used at sites 1 and 5. When examining the layout of the different sites, it is obvious the sites are all located on fairly flat terrains and thus the topographies at the sites are unlikely to play a role. In addition, Gitterman and Hofstetter (2012) and Gitterman (2013) noted similar differences when using different explosives with varying VOD's.

Table 7, which covers the log of the secondary shock wave delay, merely reflects same data as in Table 6, but where the logarithm of both the secondary shock wave and the scaled distance have been evaluated. Once again the R^2 values are acceptable, except for site 2, and thus it is a good solution for predicting equations.

6 Conclusions

At the start of the study, the one objective was to determine whether or not one could utilise equations developed for predicting the ground motion produced by buried explosions to predict the effects of explosions on the Earth's surface using data obtained from a small network of surface-installed seismograph stations. The aim of the equations would be to prevent harm to people and damage to infrastructure.

Many of the predictive equations within literature are focused on explosions within the ground such as mining blasts and tunnelling. Other equations do examine surface explosions, but use more specialised equipment.

This study has identified a number of predictive equations that have produced acceptable results when examining data obtained from military ordnance demolitions on the surface. Therefore, the first objective of the study has been achieved.

When examining the second objective of the study, which was to determine whether or not there are other equations available that are perhaps more suitable for surface explosions, it was found that the measurements recorded during the shaking of the geophones and seismometers by the atmospheric shock wave, may be more useful than ground motion measurements. This is because the ground motion is not always clearly recorded, as demonstrated within the study. In general, the values for the atmospheric shock waves were easier to determine than those of the ground motion because the atmospheric shock waves are more prominent on the seismograms than those of the ground motion, due to the fact that very little of the energy is transmitted into the ground. The variations in the pressure from atmospheric shock waves cause the seismographs to shake, especially since the equipment was installed on the surface.

The suitability of the equations in achieving the objectives of this study is summarised in Table 8. Table 8 clearly shows that the USBM prediction equation using PPV measurements, and originally developed for underground explosions, was the most suitable in achieving the first objective of the study. Table 8, also shows that the relations between PPV and SW, Dt and ln SD, and log Dt and log SD are the newer suitable equations which address the second objective of the study.

Table 8. Summary of the suitability of each of the equations examined in achieving the objectives of the study.

	Objective 1	***Objective 2***
USBM: $PPV = K(SD)^{-\beta}$	Suitable	
Ambraseys: $PPV=K(SD_A)^{-\beta}$	Not Suitable	
Langefors: $PPV=K(SD_L)^{\beta}$	Not Suitable	
USBM: $Pk = K(SD)^{-\beta}$	Not Suitable	
Ambraseys: $Pk=K(SD_A)^{-\beta}$	Not Suitable	
Langefors: $Pk=K(SD_L)^{\beta}$	Not Suitable	
USBM: $Fst = K(SD)^{-\beta}$	Not Suitable	
Ambraseys: $Fst=K(SD_A)^{-\beta}$	Not Suitable	
Langefors: $Fst=K(SD_L)^{\beta}$	Not Suitable	
PPV vs SW		Suitable
USBM: $Snd = K(SD)^{-\beta}$		Not Suitable
Ambraseys: $Snd=K(SD_A)^{-\beta}$		Not Suitable
Langefors: $Snd=K(SD_L)^{\beta}$		Not Suitable
Dt vs ln SD		Suitable
Log Dt vs log SD		Suitable

Although, the USBM PPV predictive equation was identified as the most reliable equation out of the three equations examined, the predictive equation using the secondary shock wave phenomenon produced better results. However, the study also showed that a new method using the relations between PPV and scaled weight (SW) was as reliable as the predictive equations found in literature, but far less cumbersome.

The usefulness of the suggested prediction equations would depend on what requires predicting. Thus, for determining the limits of a military demolition range, one would require PPV prediction and thus the USBM equation or the PPV vs SW equation would be the better solutions. On the other hand, for assisting in forensic seismology to determine the details of an unexpected explosion (such as gas pipelines, silo explosions and vehicle bombs), the secondary shock wave and atmospheric shock wave displacement could be utilised, especially if the ground motion waves are not obvious within the seismograms.

7 References

Aloui, M., Bleuzen, Y., Essefi, E. and Abbes, C. (2016). Ground vibrations and air blast effects induced by blasting in open pit mines: Case of Metlaoui mining basin, Southwestern Tunisia, *J. Geol. Geophys*, 5:3. DOI: 10.4172/2381-8719.1000247

Ambraseys, N.R. and Hendron, A.J. (1968). Dynamic behavior of rock masses. Rock mechanics in engineering practice. London: Wiley.

Atkinson, G.M. (2004). Empirical attenuation of ground-motion spectral amplitudes in southeastern Canada and northeastern United States. *Bull. Seism. Soc. Am.*, 94, pp 1079-1095.

Atkinson, G.M. and Mereu, R.F. (1992). The shape of ground motion attenuation curves in southeastern Canada. *Bull. Seism. Soc. Am.*, 82, pp 2014-2031.

Blair, D.P. (2004). Charge weight scaling laws and the superposition of blast vibration waves. *Fragblast,* 8, pp 221-239.

Bongiovanmi, G., Gonelli, V., Rienzo, G. and Rinaldis, D. (1991). Experimental Studies of Vibrations caused by blasting of Tunnel excavation. *Earthquake, Blast and Impact: Measurement and Effects of Vibration,* Elsevier Applied Science, London, pp 201-210.

Bonner, J., Waxler, R., Gitterman, Y. and Hofstetter, R. (2013). Seismo-acoustic energy partitioning at near-source and local distances from the 2011 Sayarim explosions in the Negev desert, Israel. *Bull. Seism. Soc. Am.*, 103, No. 2A, pp 741-758.

Edwards, W.N., Eaton, D.W., McCausland, P.J., ReVelle, D.O. and Brown, P.G. (2007). Calibrating infrasonic to seismic coupling using the Stardust sample return capsule shockwave: Implications for seismic observations of meteors. *J. Geophy. Res., 112, B10306, doi:10.1029/2006JB004621.*

Evers, L.G., Ceranna, L., Haak, H.W., Le Pichon, A. and Whitaker, R.W. (2007). A Seismoacoustic analysis of the gas-pipeline explosion near Ghislenghein in

Belgium. *Bull. Seism. Soc. Am.*, 97, pp 417-425.

Ford, S.R., Rodgers, A.J., Xu, H., Templeton, P.H., Foxall, W. and Reinke, R.E. (2014). Partitioning of seismoacoustic energy and estimation of yield and height-of-burst/depth-of-burial for near surface explosions. *Bull. Seism. Soc. Am.*, 104, pp 608-623.

Gitterman, Y. (2013). Secondary shock features for large surface explosions: results from the Sayarim Military Range, Israel and other experiments. *Shock Waves*, DOI 10.1007/s00193-013-0487-y.

Gitterman, Y. and Hofstetter, R. (2012). GT0 explosion sources for IMS infrasound calibration: Charge design and yield estimation from near-source observations. *Pure Appl. Geophys.*, DOI 10.1007/s00024-012-0575-4.

Gupta, I.N. and Hartenberger, R.A. (1981). Seismic phases and scaling associated with small high-explosive surface shots. *Bull. Seism. Soc. Am.*, 71, pp 1731-1741.

Havskov, J., Ottemöller, L. (2001): The SEISAN earthquake analysis software for Windows, Solaris and Linux, manual. University of Bergen, Norway.

Ichinose, G.A., Smith, K.D. and Anderson, J.G. (1999). Seismic analysis of the 7 January 1998 chemical plant explosion at Kean Canyon, Nevada. *Bull. Seism. Soc. Am.*, 89, pp 938-945.

Johnston, A.C. (1987). Air blast recognition and location using regional seismographic networks. *Bull. Seism. Soc. Am.*, 77, pp 1446-1456.

Joint Committee on Administrative Rules (1998). Administrative Code, *Title 62: Mining,* Chapter 1, Part 1817, Section 1817.67.

Kahriman, A. (2002). Predictability of the ground vibration parameters induced by blasting during the tunneling. *Min. Resourc. Engin.* 11(3), pp 279-291.

Khandelwal, M. and Singh, T.N. (2007). Evaluation of blast-induced ground vibration

predictors. *Soil Dynam. and Earthq. Engin.*, 27, pp 116-125.

Kitov, I.O., Murphy, J.R., Kusnetsov, O.P., Barker, B.W. and Nedoshivin, N.I. (1997). An analysis of seismic and acoustic signals measured from a series of atmospheric and near-surface explosions. *Bull. Seism. Soc. Am.*, 87, pp 1553-1562.

Koper, K.D., Wallace, T.C., Reinke, R.E. and Leverette, J.A. (2002). Empirical scaling laws for truck bomb explosions based on seismic ad acoustic data. *Bull. Seism. Soc. Am.*, 92, pp 527-542.

Kumar, R., Choudhury, D. and Bhargava, K. (2016). Determination of blast-induced ground vibration equations for rocks using mechanical and geological properties. *J. of Rock Mech. and Geotech. Engin.*, 8, pp 341-349.

Langefors, U., Kihlstrom, B., Westerberg, H. (1958). Ground vibrations in blasting. Water Power.

Milev, A., Durrheim, R., Brovko, F., Kgarume, T., Singh, N., Lumbwe, T., Wekesa, B., Pandelany, T. and Mwila, M. (2016). Development of a South African minimum standard on ground vibration, noise, air-blast and flyrock near surface structures to be protected. SIM 14-09-01, Mine Health and Safety Council.

New, B.M. (1991). The effect of detonator variability on explosively induced ground vibration. *Earthquake, Blast and Impact: Measurement and Effects of Vibration,* Elsevier Applied Science, London, pp 163-175.

Ozer, U. (2008). Environmental impacts of ground vibration induced by blasting at different rock units on the Kadikoy-Kartal metro tunnel. *Engin. Geol.*, 100, pp 82-90.

Ozer, U., Kahriman, A. and Aksoy, M. (2008). The analysis of ground vibrations induced by bench blasting at Akyol quarry and practical blasting charts. *Environ. Geol.*, 54, pp 737-743.

Puri, V.K. and Prakash, S. (1991). Estimation of design forces on structures near quarries

from field blast tests. *Earthquake, Blast and Impact: Measurement and Effects of Vibration,* Elsevier Applied Science, London, pp 201-210.

Quest Consultants (1991). Comparison of vapour cloud explosion models – Part II, *The Quest Quarterly,* 4, issue 2.

Redmayne, D.W. and Turbitt, T. (1991). Ground velocity attenuation associated with the Lockerbie air crash impact. *Earthquake, Blast and Impact: Measurement and Effects of Vibration,* Elsevier Applied Science, London, pp 352-362.

Williams, M.S. and Newell, J.P. (1991). Methods for the assessment of the blast response of engineering structures. *Earthquake, Blast and Impact: Measurement and Effects of Vibration,* Elsevier Applied Science, London, pp 176-185.

Willis, D.E. and Wilson, J.T. (1960). Maximum vertical ground displacement of seismic waves generated by explosive blasts. *Bull. Seism. Soc. Am.*, 50, pp 455-459.

Yan, Z., Jiang, P. and Duan, J. (2009). Study on the methods of predicting blasting-induced ground vibration intensity. RaSiM: Controlling Seismic Hazard and Sustainable Development of Deep Mines (Tang, C.A. editor), Rinton Press.

APPENDIX A

Table 9. Measurements from site 1. A comma separates each measurement listed.

Ordnance (kg)	Distance (m)	Snd (nm)	Fst (nm)	Pk (nm)	PPV (nm/s)	SS (sec)
15						
	2700				4197, 9922	
	2760		11, 28, 8,42, 9,22	142, 88, 248	5419, 3431, 6389, 4504	
	3600		6,89, 26		4095, 4869, 3655	
	3750					
	5760					
	6320	680, 662, 932	5,3			
	8540	484, 537, 521	4,53			
	8610	1264, 438	1,8			
30						
	2700		22, 29	70	7760	
	2760	499	9,79, 20, 16	203, 627, 296, 500	4076, 6800	
	3600		11, 13, 13, 58	1405, 78, 124	3919, 3655, 5493, 3616	
	3750		5,9	717, 58, 824	3505, 3487, 5139	
	5760		13	404		
	6320	1570	5,37, 3,46, 3,23	3554, 62		
	8540	486, 1121, 408				
	8610					
50						
	2700					
	2760	530, 630, 491, 671	3,62	598	6075, 6797, 11730	
	3600					

	3750					
	4960				1744, 1190, 1272, 1905	
	5760					
	6320		5,24			
	8540	433, 447, 430	6,26			
	8610	1472, 1765, 1646, 2571				
60						
	2700	1083	36, 3,92, 16	343, 549, 123	11554, 11117, 14063, 6177, 7028, 10316	
	2760	572, 1131, 1745	17, 15	475, 198, 114	8753, 22990, 8803, 6703	
	3600	1184	16, 24, 37, 4,77, 16	970, 484, 389, 203, 196	4283, 5198, 20869, 4085, 8417, 3913	
	3750	509	12, 13, 4,46, 3,18	1267, 128	2704, 16740, 4687, 2721, 11239, 3492	
	4960	1325, 1052	27		9005, 3321	
	5760					
	6320	841, 1270, 2056	4,55, 3,33, 4,66, 21	3019, 236, 95, 80		
	8540	596, 495, 650, 4974, 840	3,56, 3,08, 16, 19	824, 84, 75		
	8610	1890, 560, 838, 526, 952	3,85	78, 97		
120						
	2700	889, 932	3,64, 72, 64, 53	202, 1233, 180	16587, 15657, 15052, 11449, 17077,	

					13643, 13441, 12399	
	2760	1397, 537, 665, 828, 884, 3150, 659, 1528	43, 5,21, 16, 19, 21, 22, 35, 3,9, 33	253, 165, 185, 364, 585, 62, 101, 184, 466	6377, 11695, 10956, 12200, 10281, 11174, 10119, 9048, 9632	
	3600	1521, 717, 2699, 1019, 2582	28, 24, 29, 3,72, 3,01, 6,61	786, 268, 180, 202, 153, 209	1521, 8909, 6382, 7174, 6047, 4788	0,11
	3750	747, 1591	27, 38, 8,93, 5,15, 6,38, 4,25	354, 391, 246, 223, 161, 101	3510, 3209, 3742, 16296, 2719, 2847, 15660, 4380	
	4960	2269, 843	5,86	117, 202	12341, 2131, 1900, 2373, 2889	
	5760					
	6320	432, 495	16, 4,52, 7,54, 7,15, 29	379, 1802, 1225, 188, 49, 512		0,16
	8540	755, 1716, 837, 3265, 1381, 1392	6,47, 25, 4,47, 8,10, 15, 24	1438, 2203, 2235, 88, 98, 161, 112		
	8610	541, 507, 1759, 778, 602, 1873, 941	7,79, 11, 3,38, 2,35, 3,63, 2,47	1852, 1950, 523, 882, 112, 275, 125		0,15
240						
	2700	1048	13	54	32886, 23126, 19690,	

					22736, 19252, 13565	
	2760	760, 2341, 2350, 1775, 1044	38, 56, 49, 3,12, 14	84, 318, 176, 220, 214	19491, 17907, 17745, 18018, 16753	
	3600	2488, 417, 1979, 606, 946	51, 50, 50, 2,67, 11, 3,71, 30	70, 179, 179, 227, 147, 171, 74	14461, 9655, 14179, 10259, 13824, 11512	0,12
	3750		9,71	135	4095, 7772, 2189	0,12, 0,13, 0,17, 0,12, 0,14
	4960	957, 1824, 2663, 1676	3,33, 3,43, 4,32, 11, 7,99	176, 311, 141, 406, 184	2633, 5497, 6152, 2654, 2937, 3600	
	5760					
	6320	2903, 2126, 481, 678, 2400, 1783	15, 8,01, 12, 3,18, 7,12, 57	495, 105, 82, 307, 120		
	8540	1654, 2050, 1838, 1383, 985, 875	4,58, 5,13, 38, 91	242, 226, 192, 278, 145		0,12
	8610	1902, 1316, 458, 1002	4,47, 7,68, 5,19, 4,68, 4,21	268, 74, 223, 240, 157		0,14, 0,13, 0,13, 0,09, 0,16
300						0,1, 0,17
	2700				33412, 30997, 23010	0,18, 0,15, 0,14, 0,15, 0,16

	2760	1555, 2316, 863	31, 11, 8,88	122, 77, 178	19247, 20406, 17027	
	3600	2475, 2710, 2200	75, 12	173, 199	16395, 12286, 12429	
	3750					
	4960	746	9,23, 19, 55	220, 326	3039	0,08, 0,12, 0,07, 0,15
	5760					0,16
	6320	1147, 1334	49, 5,64, 19	131, 156, 63		
	8540	829, 541, 1965	7,66, 6,98, 6,26	109, 115, 332		0,15
	8610	1769, 1961	6,43, 47, 4,83	156, 212, 74		
						0,17, 0,19
						0,18, 0,19
						0,16

APPENDIX B

Table 10. Measurements from site 2. A comma separates each measurement listed

Ordnance (kg)	Distance (m)	Snd (nm)	Fst (nm)	Pk (nm)	PPV (nm/s)	SS (sec)
50						
	2380	578, 744, 651, 1434, 1049, 382, 442	31, 29, 20, 6,21, 7,36, 8,99, 13, 32	182, 203, 79, 69, 78, 100, 168, 257		
	2500	590, 642, 746	77, 42, 49, 48, 31, 40, 124, 75	226, 200, 215, 150, 198,267		
	3770	491				
	3870		73, 73, 23, 22, 32, 22, 12	186, 237		
	4000	235				
	4680		21, 24	391, 142		
	4700	192, 186, 352	7,63, 1,11	35, 54, 113		
	4840					
	5920		23, 59	193		
	8490		14, 12, 45, 12			
100						
	2380	697, 664	61, 41	313, 141	13550, 11773	
	2500	2165	124, 104, 90	916, 320, 598	18643, 21282, 22066	
	3770	463				
	3870		75, 86, 100		29592, 32054, 27750	
	4000	295, 396			2968, 3202, 3576	
	4680		41	583	8405	
	4700	533	16	141	5972, 3349, 6646	
	4840	155	8,95	29	2916,	

					3539	
	5920		35, 26, 36	193	19163, 12988	
	8490					
200						
	2380	2932	81, 109	313, 238	11768	
	2500	2552, 2665	163, 230, 264	667, 640, 528	17014, 41183, 36091	
	3770				38956, 12560	
	3870		174		12857, 42231, 52064	
	4000		13	53	37356, 5912, 6407	
	4680		95	448	16383	
	4700	274	24	87	5769, 5459	
	4840				4918, 6966	
	5920		29, 49, 45	498, 271, 263	5789, 16591, 17433	
	8490					
300						
	2380	2339, 2655	120, 128	357, 291	25338, 27040	0,11, 0,12
	2500	4161	272, 343	581, 701	43053, 37750	0,21, 0,21
	3770	1978				
	3870		159		55622, 33278	
	4000	854	9,17	100	6496	
	4680					0,23
	4700	526, 879	36, 37	111, 124	5682, 6062	0,22, 0,23
	4840	279			6865, 6849	
	5920	906	92, 31	378	17046, 13612	
	8490					
400						
	2380	1801	129	455	55571	
	2500		289, 355	900, 764	45127	0,19

	3770					
	3870		249		51544, 47916	
	4000		21, 27	61, 52	7639, 8123	
	4680		76, 96	577, 455	22111, 22992	0,23
	4700	993, 1017	38, 48	180, 123	8061, 8846	0,3
	4840					
	5920				21497, 16050	
	8490					
800						
	2380	3105	238	610	39844	
	2500	9962			82004	0,22
	3770					
	3870				91268	
	4000				10988	
	4680				38112	
	4700	1245	63	277	11893	
	4840					
	5920				34156	
	8490					
1600						
	2380	11318	269	915	59316	
	2500					
	3770					
	3870				125463	0,17
	4000	717	80	201	24358	
	4680		309		68698	0,31
	4700				20674	
	4840					
	5920				53880	
	8490	2697				

APPENDIX C

Table 11. Measurements from site 3. A comma separates each measurement listed

Ordnance (kg)	Distance (m)	Snd (nm)	Fst (nm)	Pk (nm)	PPV (nm/s)	SS (sec)
4,8						
	1					
	1090		21			
	2140					
	3790					
	6340					
5						
	1	4179, 65521, 41224, 141542	284	1118		
	1090	1635, 1717, 23663, 3109, 1634, 1827	48, 82, 57, 68, 68,51	296, 1893, 406, 1556, 722, 566		
	2140	713, 2378, 3325, 3124, 2288, 3436, 2928	71, 4,63, 8,86, 12, 21, 49, 23	3261, 2209, 2702, 3023		
	3790					
	6340					
10						
	1				21595460, 82487, 105626	
	1090	5323, 3051, 1847, 6891	7, 151, 131, 15	2959, 1040, 2131, 236	31582, 33015, 27826	
	1720				4265, 5099, 5519	
	2140	2331, 3532, 5809, 4194, 2996	42, 21, 45, 40, 32	3928, 4319, 3178, 4340, 848	11000, 27858, 31167	

	3790	14380, 14472				
	6340					
13						
	1					
	1090					
	2140	2730	31	2905		
	3790	7672				
	6340	194				
20						
	1	195818, 153308, 6928, 5733	357	962, 862	33114728, 29340880, 153645, 124631, 53913904	
	1090	2774, 2799, 2122, 2748, 6356	160, 136, 210, 228, 137	1817, 1563, 3656, 2853, 1803	39258, 40290, 40290, 44235	
	1720				5233, 4437, 4437, 9039	
	2140	3049, 6925, 3706, 6677	104, 61	4898, 4489, 6371	15390, 16242, 16242, 45554	
	3790	13182, 21208, 21505, 24055, 4561				
	6340					
22						
	1	173027				
	1090					
	2140	1508, 2453, 3473, 5665	26, 27, 32, 38	7081, 2484, 6587, 3285		
	3790	3206, 3928, 8296				
	6340					

26						
	1					
	1090					
	2140					
	3790	18505				
	6340	285				
39						
	1					
	1090					
	2140	6623	41	7875		0,14
	3790	15976				0,19
	6340	219				0,2
40						
	1	366501, 288725, 8941	286	1904	54016796, 161070, 160043	
	1090	12905, 5996, 5847	349, 245, 472, 304	1444, 7019, 7399, 1616	75758, 58315, 92521, 64753	0,06, 0,08, 0,1, 0,11
	1720				10050, 8054, 10694, 12984	
	2140	5787, 8105, 1325	55, 62	1487, 1890, 8257	27651, 24815, 7563, 74383	0,12, 0,14
	3790	38973, 38613, 15220, 57814, 20618, 32438, 17548, 8413				0,24, 0,25, 0,25, 0,25, 0,22, 0,2, 0,17, 0,19, 0,17, 0,18
	6340	295, 281, 204	5,34	1174, 1663, 1497	549, 355, 681	0,22, 0,21, 0,22
60						
	1					
	1090	8198	471	2968		0,08
	2140	9965	194	1964		0,1
	3790	15365, 19723				0,14, 0,23

	6340	344, 506	1,59	1246, 211		0,28, 0,24

APPENDIX D

Table 12. Measurements from site 4. A comma separates each measurement listed

Ordnance (kg)	Distance (m)	Snd (nm)	Fst (nm)	Pk (nm)	PPV (nm/s)	SS (sec)
30						
	1					
	2000					
	5510					
	5550	590				
	8540	453				
50						
	1					
	2000				5216	
	3050			3,57	5530	
	5510	166	40		1572	
	5550	265				
	8540	319				
60						
	1					
	2000	761				
	5510					
	5550					
	8540					
84						
	1					
	2000	1478				
	3050		17			
	5510	261, 392, 343	5,97			
	5550		12			
	8540					
100						
	1					
	2000				9581, 11024, 13819	
	3050				4833, 4119, 5118	
	5510				2240,	

					1753, 1489	
	5550	321, 557	5,34	27		
	8540	489, 984	4,5, 5,67, 18			
108						
	1	1047				
	2000					
	5510	2881	7,05			
	5550	1749				
	8540	3181				
120						
	1					
	2000					
	3050			6,57		
	5510					
	5550					
	8540	2312				
150						
	1					
	2000				11981, 14967, 12156, 9151	
	3050				4745, 7603, 5993, 5253	
	5510	405			2183, 488, 2184, 2097, 488, 2184, 2097	
	5550	287, 317, 421	7,74, 24	190		
	8540	636, 865, 497, 830	34, 22, 17, 25			
200						
	1	7917, 9004, 3857, 4660			346231, 39554, 493135, 384264,	

					464746, 354664, 484941, 544431, 414759, 549668, 547204	
	2000	3254, 11354, 18864, 1506, 1893, 1531, 3632	15, 13, 9,39	27, 155, 217, 300	21689, 18161, 18680, 5888, 10277, 13105, 12480, 14879, 11410, 9977, 13728, 10082, 9198	0,13
	3050		1,59, 1,19, 1,57, 9,28	100, 122, 11, 12, 8,73, 11, 204, 5,44, 7,09, 6,86, 11, 5,94, 8,26, 8,15	3239, 5056, 13234, 9639, 13957, 9537, 4147, 5762, 8455, 3331, 10369, 2450, 3122, 3043, 3195	0,18, 0,07, 0,15, 0,11, 0,15, 0,09, 0,11, 0,12, 0,09, 0,11, 0,13, 0,15, 0,15, 0,16, 0,11, 0,12, 0,16
	5510	1887, 406, 638, 409, 479, 754	130, 4,46, 172, 23, 6,65	172, 35, 56, 38	4089, 3043, 2658, 4477, 7039, 8670, 5170, 1701, 1647, 6750, 6995, 2737, 6317, 5155, 5155	0,16, 0,22, 0,17

	5550	650, 770, 413, 1401, 694, 239, 353, 550, 508, 2669, 1813, 1279, 1370, 1530, 1639, 2245, 1191	4,58, 194, 1,55, 5,16, 4,68, 7,81	36, 10, 11		0,2, 0,21, 0,2, 0,23, 0,18, 0,23, 0,25, 0,18, 0,19, 0,27, 0,27, 0,22, 0,16, 0,15, 0,17, 0,19, 0,18
	8540	1051, 863, 1307, 1952, 1994, 1087, 1598, 532, 2493, 3740, 2903, 2345, 4492, 2556, 2915, 3567	7,49, 9,4, 57, 33, 15, 6,65, 6,67	25, 9,04, 99		0,28, 0,3, 0,35, 0,33, 0,27, 0,27
222						
	1					
	2000			529	15128	
	3050			13	7533	0,15
	5510	994	5,86	90		
	5550					
	8540	5348				0,34
240						
	1					
	2000				14368	
	3050			9,78	6524	0,19
	5510	1695	6,02	56	2204	0,14
	5550	1619	9,31			0,16

	8540	3114	6,5	118		0,3
250						
	1	6865, 5824			166118, 571429, 643709, 471920, 484888, 324944	
	2000	16059, 1938	21	221, 337	16626, 26461, 16070, 12228, 21759, 14659, 15369, 20824	0,13
	3050			9,94, 52, 10, 11, 9,01, 9,08	21638, 7533, 6980, 6934, 6711, 3952, 4964, 5698	0,1, 0,11, 0,12
	5510	961, 1436, 5702, 2864, 2038, 383	7,94, 3,94, 6,96, 4,48, 1,62, 9,05	45, 46, 61, 40, 43, 192	3688, 2513, 2056, 1682, 2554, 2059, 1834, 5141	0,15, 0,16, 0,16
	5550	12314, 1403, 5462, 1405, 1528, 2749, 2422, 1405	23, 25	11, 108		0,17, 0,19, 0,14, 0,18, 0,14, 0,18, 0,17
	8540	634, 254, 2902, 2793, 5510, 6856, 5731, 2704	9,72, 5, 7,6, 3,88, 7,77			0,34, 0,34, 0,25, 0,33, 0,38

300						
	1					
	2000		11	151		
	3050			3,93		
	5510	1043		23		
	5550	427				
	8540	358				
356						
	1	7838				
	2000	1791				
	5510	3524	2,37			
	5550	4877	2,2			
	8540	3759	2,72			
394						
	1					
	2000	2461	6,17		32443	
	3050			11	15007	0,16
	5510	514		55	3782	0,19
	5550					
	8540	4986	8,34	49		0,34
750						
	1	1243				
	2000					
	3050			9,12		
	5510	6599	3,1	141		
	5550	1216				
	8540	6051				

APPENDIX E

Table 13. Measurements from site 5. A comma separates each measurement listed

Ordnance (kg)	Distance (m)	Snd (nm)	Fst (nm)	Pk (nm)	PPV (nm/s)	SS (sec)
100						
	5250	1538	35		3685,6	
	12370					
	13600	327			7238,8	
	14430				1507	
	18170				2505,4	
	19300					
	20520				2125,9	
	29070				3611,2	
400						
	5250	609	14	875		
	12370					
	13600		65			
	14430					
	18170					
	19300					
	20520					
	29070					
500						
	5250	2541	52	250	5472,4	
	12370				2337	
	13600	459	6,33	794	4576,3	
	14430				1751,6	
	18170				6428,8	
	19300		76	340		
	20520					
	29070				2211,2	
2000						
	5250					
	12370					
	13600	947, 908, 970	43, 51, 41,	624, 922, 918	4891,3, 6087	
	14430					
	18170					
	19300					
	20520				4186, 3145,9, 2162,5	

	29070					
3000						
	5250	12530	87	1996	16693,9	0,18
	12370	1812				
	13600	4587, 3747	63, 66	857, 1983	7443,1, 5746,3	
	14430				5235,9	
	18170				7369,3, 6121,8	
	19300	1768	244	1413		
	20520				2103,1, 14064,9	
	29070	1948			13396,8, 1997,6	0,19
6000						
	5250					
	12370	1632	50	993	4169,3	0,19
	13600	2085	62	1279	7749,7	
	14430	996	51	817	5510,8	0,2
	18170				2631,6	
	19300	11543	28			0,26
	20520	1927	22	203	2429,3	0,19, 0,19
	29070	5641	14	307	1506,3	0,22, 0,22
12000						
	5250	15370	132	3088	39552,6	
	12370	1089	83	620	8216,4	0,24
	13600	5026	75	768	10891,7	0,24
	14430	1204	65	467	6883,6	
	18170				5519,5	0,27
	19300	1779				
	20520	916	7,4			
	29070	394		345	14997,8	
20000						
	5250	7845	322	2970	41174,9	0,22
	12370				7291,1	
	13600	1925	113	2268	12621,8	
	14430				7421,1	
	18170				6020,6	
	19300	1050	59	1964		
	20520					
	29070				5013,6	

25000						
	5250	17590, 25686	526, 911	4836, 7332	75134,3, 95432,7	0,19, 0,25
	12370				15559,5, 15049	
	13600	5067, 10408	181, 254	1754, 3459	24488,9, 29922,8	0,23, 0,26
	14430				15512,4, 15851,4	0,24
	18170		143	3127	9915,7, 8451,1	
	19300	3391		1159, 2072		
	20520		47	2876	10045,6	
	29070		51	1454	4563,8	